Electrostatic Vibration-to-Electric Energy Conversion

by

José Oscar Mur Miranda

Bachelor of Science in Electrical Engineering
Massachusetts Institute of Technology, 1995
Master of Engineering in Electrical Engineering and Computer Science
Massachusetts Institute of Technology, 1998

Submitted to the Department of Electrical Engineering and Computer Science
in partial fulfillment of the requirements for the degree of

Doctor of Philosophy in Electrical Engineering and Computer Science

at the

Massachusetts Institute of Technology

February 2004

Author .....
Department of Electrical Engineering and Computer Science
November 5, 2003

Certified by .....
Jeffrey H. Lang
Professor of Electrical Engineering and Computer Science
Thesis Supervisor

Read by .....
Anantha P. Chandrakasan
Professor of Electrical Engineering and Computer Science
Thesis Reader

Read by .....
Martin A. Schmidt
Professor of Electrical Engineering and Computer Science
Thesis Reader

Read by .....
Alexander H. Slocum
Professor of Mechanical Engineering, MacVicar Faculty Fellow
Thesis Reader

Accepted by .....
Arthur C. Smith
Chairman, Department Committee on Graduate Students

Electrostatic Vibration-to-Electric Energy Conversion

by

José Oscar Mur Miranda

Submitted to the Department of Electrical Engineering and Computer Science
on November 5, 2003, in partial fulfillment of the
requirements for the degree of
Doctor of Philosophy in Electrical Engineering and Computer Science

Abstract

Ultra-Low-Power electronics can perform useful functions with power levels as low as 170 nW. This makes them amenable to powering from ambient sources such as vibration. In this case, they can become autonomous. Motivated by this application, this thesis provides the necessary tools to analyze, design and fabricate MEMS devices capable of electrostatic vibration-to-electric energy conversion at the microwatt level. The fundamental means of energy conversion is a variable capacitor that is excited through a generating energy conversion cycle with every vibration cycle of the converter.

This thesis presents a road map on how to design MEMS electrostatic vibration-to-electric energy converters. A proposed converter is designed to illustrate the design process, and is based on vibration levels typical of rotating machinery, which are around 2% of the acceleration of gravity from 1-5 kHz. The converter consists of a square centimeter with a 195 mg proof mass which travels ± 200 μm. This mass and travel can couple to a sinusoidal acceleration source of $0.02g$ at 2.5 kHz, typical of rotating machinery, so as to capture 24 nJ per cycle. This moving proof mass is designed to provide a variable capacitor ranging from 1 pF to 80 pF. Adding a capacitor of 88 pF in parallel with this device will result in a capacitance change from 168 pF to 89 pF that is required to extract 24 nJ using a charge-constrained cycle. This device can be attached to power electronics that implement a charge-constrained cycle and deliver 0.5 nJ back to the reservoir for a total power output of 1.3 μW at 2.5 kHz. The efficiency of the electrical conversion is 2%. Including packaging, the power per volume would be 0.87 μW/cm^3 and the power per mass would be 1.3 μW/g.

System improvements are also identified such as those that address the principal sources of loss. For example, decreasing the output capacitance of the MOSFET switches from 10 pF to 1 pF, while keeping the energy conversion cycle the same, results in an energy output of 13 nJ out of 24 nJ, for an efficiency of 54% and a power output of 33 μW. This argues strongly for the use of integrated circuits in which the output capacitance of the MOSFET switches can be reduced for this application.

Thesis Supervisor: Jeffrey H. Lang
Title: Professor of Electrical Engineering and Computer Science

Acknowledgments

This thesis was prepared through collaborative participation in the Advanced Sensors Consortium sponsored by the U.S. Army Research Laboratory under Cooperative Agreement DAAL01-96-2-001, by the Charles Stark Draper Lab Internal Research and Development Program Contract #DL-H-513128, and by ABB. My first three years of graduate study at MIT were funded by a National Science Foundation Fellowship. Special thanks go to Peggy Carney, who provided an EECS Fellowship, and Dean Isaac Colbert, who gave me a Graduate School Fellowship so that I could fully devote myself to this thesis and be able to graduate.

I also want to thank Kurt Broderick, who built the first prototypes using Mask 3, and was a source of constant help in the fabrication lab. Vicky Diadiuk gave me all the support I needed to work in the fab and a wonderful smile. Paul Tierney took care of all the implants on my wafers. The members of the microengine group always gave me advice, materials, and access to the machines. I have to make special mention of Dennis Ward, who gave me a lot of time in the STS, Lin Vu, who spent countless hours with me in the lab, and Arturo Ayón, who answered all my questions regarding the STS.

Wayne Ryan helped me build the test macro capacitor and was always a pleasure to work with. Antimony L. Gerhardt, of the Schmidt Group Laboratory, graciously helped me borrow the shaker table. Prof. Dave Perreault and Joshua Phinney always answered my questions with outstanding knowledge of electronics, and helped me find whatever chips and any other materials I needed. Timothy Neugebauer gave me the transformer used in the circuit. Steve Umans gave me the MOSFETs used in the circuit.

Rajeevah Amirtharajah and Scott Meninger did the work upon which this thesis grew. I hope they enjoy the work I have done with their help.

All the readers of my thesis, Prof. Marty Schmidt, Prof. Alex Slocum and Prof. Anantha Chandrakasan, have given me all the time and effort I needed, and have truly enriched my work. I am honored to have you all as my thesis committee.

Jeffrey H. Lang deserves more thanks than I can possibly give. This thesis belongs as much to him as to me. His dedication to me and my work goes far beyond what is expected.

I am truly his student, and I can only hope that I have, and will continue to, make him proud. He is the best part of my experience at MIT. Since I don't have enough words to say what his impact in my life has been, I can only hope he understands this thank you.

Lodewyk Stein is an amazing tinkerer and problem solver. He has helped me in many ways, and always doing far more than I expected. Jian Li took me to use the waterjet and taught me to make transparency masks. I must also thank Jin Qiu and Steve Nagle for their help whenever I needed it.

Nothing would ever get done without Kiyomi Boyd, Karin Janson-Strasswimmer and Vivian Mizuno. Their professionalism and willingness to help deserve more credit than I can give them.

Pedro Zayas, Juan Carlos Pérez-Bofill and Carlos Hidrovo have been very good friends at MIT, and I have enjoyed their company always. Thanks for your part in making my life more fun and interesting.

I wish to especially thank Virginia Estrada Perales, Rita Padilla and Michelle Corona. The time you were in Boston made my life much brighter. I am confident they know how much they mean to me.

The moments of fun with Scott Poulin, Inés Beatriz "Txiki" Rodríguez de Prado, Juan Antonio "Juantxo" Pérez García, Edmundo "Mundo" Agüero, Claudio Traccana, Tellie and María will always be with me. They are the best group of friends I could ever hope to have. I will miss you until the day I die.

My parents, Maria Teresa Miranda and Rogelio Mur have been a constant source of support. I especially have to thank my mother for feeding me so many times, and my father for always being my father. I hope you enjoy my achievements as much as you deserve it.

Thanks to Marta Iraizoz Irurita, for unmentionable support.

This thesis is dedicated to my professors Jeff Lang, Al Drake, and George Verghese for believing in me, and to Linda Cunningham for a job well-done. You have been true angels in my life, and I can only share what I am with you in the hope of making you proud.

Contents

List of Figures

List of Tables

Chapter 1

Introduction

Energy harvesting is the use of energy present in the environment to perform useful functions. These functions might include sensing, monitoring, communication, computation, actuation and control. Sources of energy are necessary in order to perform these functions. Typical choices are the use of chemical batteries or the wiring of cables from a power source. In these scenarios, the energy is either stored internally or sent from a distance. The advantage of using the energy present in the immediate environment is to minimize or eliminate the need for internal sources of energy or the need to transport this energy from another location.

This thesis provides the necessary tools to analyze, design and fabricate devices capable of electrostatic vibration-to-electric energy conversion. The intention is to harvest ambient vibration energy and transform it into electric energy to power different tasks.

Energy harvesting is commonplace today. For example, light panels convert enough energy to power calculators. Solar panels are also used in remote roads to power emergency cellular telephones, eliminating the need to wire them externally. Other examples of energy harvesting include dams, although the commonplace usage of harvesting implies the capture of energy for immediate, local use. Nevertheless, dams do capture energy from the environment to perform useful functions, although they use the power grid to distribute this energy.

Modern large-scale machines are often monitored and controlled in remote places. A typical manufacturing plant will have control rooms away from the manufacturing floor. The manufacturing floor might have chemicals dangerous to humans, or human presence

might contaminate the site. This usually requires running power and communication wires to remote locations. Furthermore, in some applications running electrical wires to a remote location might be undesirable since they may cause an explosion, generate noise or interfere with other electronics. Also, small wires are easily broken when handling a large machine. Even the presence of the chemicals contained inside a battery may be an unacceptable risk in some applications.

Typical rotating machines, such as generators, motors and combustion engines, have efficiencies ranging from 20%-99% [11, 17], where efficiency is the ratio of power output to power input. For example, a *SuperGenerator* described by Kalsi exhibit an overall efficiency of 98.6% [17]. In everyday experience, they waste considerable energy in the form of heat, sound and vibration. Often, the wasted energy is large enough to power modern low-power digital processors [10]. Thus, harvesting the waste energy could provide enough power to perform useful low-energy functions. Furthermore, the complete system can be implemented as an autonomous function and buried inside a machine.

A self-powered sensor with wireless communication would greatly minimize the complexity and cost of monitoring and control, while enhancing reliability and flexibility. The lifetime of the sensor or controller becomes as long as the life of the vibration-producing machine itself. Furthermore, after the end of the life of the device, there is no worry about hazardous chemicals from batteries, retrieving valuable resources or draining energy from fuel cells, capacitors, flywheels or any other energy storage device.

Even if a sensor uses a battery, harvesting energy can decrease the energy demand on the battery and prolong its life. The energy, if present in excess at a particular moment, can even be used to recharge the battery. There are harsh environments in which a normal battery, solar cells or a combustion engine may not work appropriately: high temperature, darkness, vacuum, and/or low temperature, for example, in outer space.

Vibrations disturbing an electromagnetic field through structural displacement introduce energy into that field. Recuperation of this energy using macro-scale harvesters is often lossy and inadequate [3]. Micro-scale devices offer low resistances and small fringing effects which improve the efficiency of the harvesting and conditioning of the energy. Furthermore, at some dimension, electric fields carry higher energy densities than magnetic fields [8]. Plus, it

is easy to build electrostatic devices using current VLSI and fabrication expertise, but hard to include magnetic materials. Therefore, micro-scale devices based on electrostatic fields appear to be an attractive solution to convert mechanical vibration energy into electrical energy.

The development of an electrostatic harvester of electric energy from ambient vibrations is a novel combination that presents several challenges. In the process of creating such a device, several of its elements must be pushed to their achievable limits and novel configurations must be found. For example, a comb drive is a transducer capable of turning mechanical into electrical energy and vice versa. While many comb drives have been reported in the literature, their typical capacitance is small since the power needed to overcome losses (e.g. internal friction and air resistance) in a small MEMS device is minimal. The objective in this thesis is to convert as much mechanical energy as possible into electrical energy, so that the transfer of energy must be maximized. This transfer of energy from mechanical to electrical is directly proportional to the available change in capacitance. However, in order to increase the change in capacitance, a comb-drive must have high-aspect-ratio comb fingers and large comb travel. Such a comb drive has not yet been reported in the literature.

The power and control electronics must also be designed so as to consume minimum power since this power is a tax on the energy converter. The general principles of power and very-low-power electronics design will be invoked in the process; similar principles would guide the design of the load electronics [4, 26, 10, 9].

Previous work in this field goes back to Williams and Yates [39] who provide the theoretical framework for energy conversion using a nonlinear model similar to the model presented in Chapter 4. Shearwood and Yates [32] provide an early experimental device capable of producing 0.3 μW from ambient vibrations using magnetic transduction. Amirtharajah and Chandrakasan [2] were able to power a load of 18 μW from ambient vibration using magnetic transduction. Kymissis and Paradiso [19] report a power output of 1.8 mW from walking using piezoelectric transduction. Sterken et al [34] report the theoretical use of electret transduction to generate energy from vibration. Miyazaki et al [27] generate 120 nW from ambient vibration using electric transduction. Lee et al [22] generate 680 μW from ambient vibration using magnetic transduction in a device the size of a AA battery. Most experi-

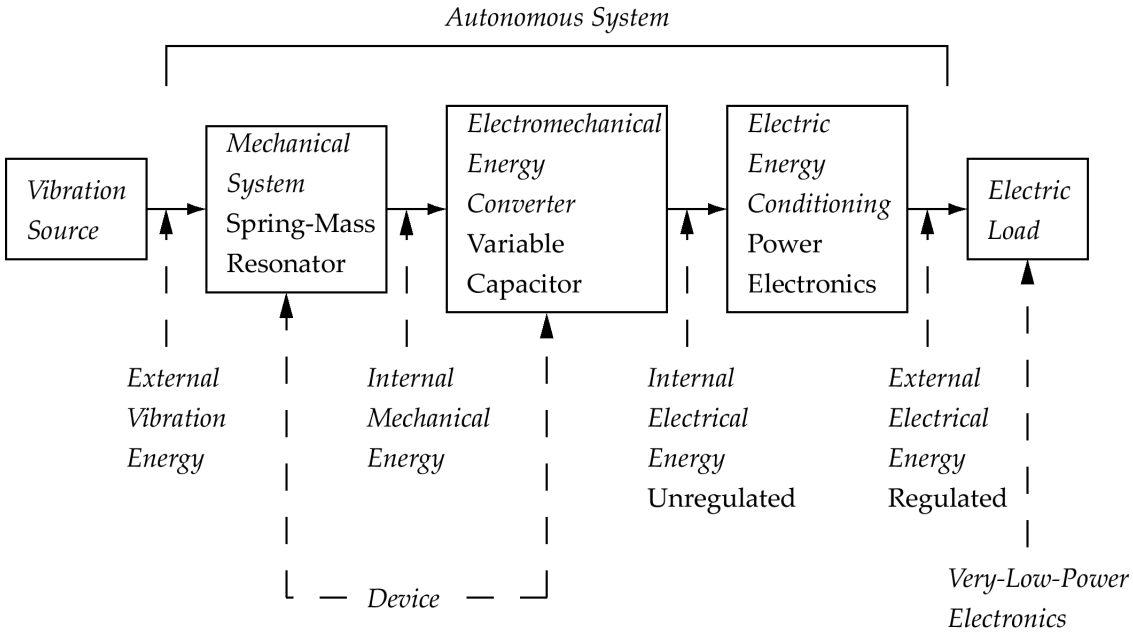

Figure 1-1: System overview of a vibration-to-electric energy converter. Ambient vibration energy is coupled onto a spring-mass resonator. Part of this energy is then transfered into a variable capacitor. The capacitor energy is sent through power electronics into a reservoir. This energy is then available to a load. This thesis focuses in the design of the autonomous system, while keeping in mind the characteristics of available vibration energy sources and the energy requirements of Very-Low-Power electronics [10, 9].

mental devices published rely in magnetic transduction. However, most devices are larger than 1 cm^3. Furthermore, the analyses that focus on electric transducers are centered on the change in capacitance producing an effective damper. There is almost no discussion of energy conversion cycles, power electronics or coupling to external vibration sources.

1.1 System Overview

This thesis will develop the tools to design an autonomous vibration energy harvester in which ambient vibration energy will be converted into electrical energy. This energy flow will be implemented using a resonant mechanical system and a variable capacitor, as shown schematically in Figure 1-1. Ambient vibration will excite the resonant mechanical system which supports a variable capacitor. Changes in the geometry of the resonant system will alter the capacitance and thus the energy stored in the variable capacitor. The energy introduced mechanically into the variable capacitor by the vibration can be extracted elec-

tronically by using clever timing of its power electronics. Electric energy will be introduced into the system when the variable capacitance is at a maximum, and will be extracted when the capacitance reaches a minimum. The extracted energy is transported using power electronics and delivered to a reservoir. The reservoir stores this energy which can then power a load.

1.2 Contributions

This thesis presents a road map for creating an electrostatic vibration-to-electric energy harvester. The road map is divided into different sections, including energy conversion cycle, power electronics, electromechanical analysis, capacitor structure, and suspension design. For each section, an analysis shows the elements of importance in the design of a complete harvester. These analyses are connected to each other, providing a complete road map for the design of energy harvesters. Furthermore, the analyses show technology challenges where more research can improve the performance of the harvesters.

Chapter 2 introduces the concept of obtaining net energy by decreasing capacitance. It establishes that a change in capacitance is needed in order to harvest mechanical energy. The energy extracted is limited by the largest voltage that the electronics can support, or the largest voltage before breakdown. In any case, an expression for energy converted given a maximum voltage is derived for both voltage-constrained and charge-constrained cycles. These analyses establish upper bounds on the amount of energy that can be obtained by electrostatic transduction of energy. Competing cycles are compared and the best cycle is selected. Alternative cycles are devised to maximize the energy conversion, and their ultimate usefulness is examined in light of the power electronics used to implement them.

Chapter 3 looks back at the voltage-constrained and charge-constrained cycles from the second chapter and presents circuits to implement these cycles. The circuits include a reservoir which can power a load. The analysis determines that a charge-constrained cycle is probably the easiest and most energetic cycle to implement given a maximum voltage. Once the circuit to implement this cycle is selected, an experimental setup is used to investigate the performance of the circuit. A complete model of the circuit is simulated, and the simula-

tion results are compared to the test circuit measurements to validate the model. The model is then used to make predictions about circuits with different component values. Specifically, the model shows the minimum change in capacitance necessary to obtain net power out given a set of electric components. This change in capacitance is converted into energy extracted from the harvester. Suggested sensing, control and actuation techniques are discussed, as well as their impact in the overall system design.

Chapter 4 introduces a resonant mechanical system in which the energy extracted from the conversion cycle in Chapter 3 is introduced. The resonator supplies the energy necessary for the conversion cycle by coupling to an external acceleration source. This analysis provides an expression relating the mass, the energy extracted and the acceleration source. These relationships are used in the design of the proof mass and its suspension in order to maximize energy conversion in Chapter 6.

Chapter 5 provides an overview of ambient vibration sources. This overview justifies the use of vibration sources as acceleration sources. It also justifies the assumption of a sinusoidal source and the frequency at which the source operates. Finally, it establishes what levels of acceleration are available for energy harvesting.

Chapter 6 uses the capacitance change requirements from Chapters 2 and 3, and the translation and mass results from Chapter 4 to design and analyze electromechanical structures. Several mechanical design options and issues are addressed. It also introduces the requirements of directional stability and low-shear forces imposed by large travel. These requirements motivate further mechanical design discussions centered on state-of-the-art suspension design. Four-bar linkages, flexure springs and multiple-beam springs are offered as a solution. The requirements on the fabrication technology used to create different capacitive structures are also described.

Chapter 7 addresses how to fabricate the structures designed in Chapter 6. A successful comb-drive converter could not be created using the fabrication process described in this thesis. It lists the problems encountered during fabrication, the workarounds employed and establishes a goal for the creation a successful finger-style harvesters. Several solutions for known problems are offered: compact footprint design with inside-out suspension which does not require bonding prior to a critical through-etch, Pyrex® or quartz substrate which uses

a relatively easy anodic bonding with no parasitic capacitance, and break-off tabs for easy isolation of the parts after the fabrication process is finished. It also relies on current MEMS valve technology to suggest that a successful parallel plate-style converter may be built.

Chapter 8 summarizes the requirements of both the power electronics and fabrication technology imposed by energy harvesters. Next, it steps back to include extra power taxation from sensors, control and actuation in the power budget for a successful autonomous harvester. It includes all the system elements to provide power per volume, power per weight and efficiency metrics for the whole system. It is concluded, for example, that power densities between 1 and 10 μW/cm^3 are feasible from MEMS vibration energy harvesters. Further technology areas are suggested, such as electret oscillations. Startup issues and the transition to steady-state are discussed.

Chapter 2

Energy Conversion Cycle

This chapter explores the fundamental energy conversion cycles that allow the conversion of mechanical energy into electric energy. These cycles are compared based on net power converted within a given voltage limit. Other considerations to be discussed, but justified in Chapter 3, are the ease of implementation and losses in the associated electronics. After the comparisons are made, a particular cycle is chosen to serve as the basis for the design of a mechanical vibration energy harvester. Further chapters will develop this design and its implications.

In electroquasistatic electromechanical systems, energy conversion can be visualized using the QV diagram that describes the conversion [41]. In the QV diagram, any closed loop represents an energy conversion cycle through the system. If the system traverses this path clockwise, mechanical energy is converted into electrical energy.

2.1 Charge-Constrained Energy Conversion Cycle

The energy conversion cycle shown in Figure 2-1 is termed a constant-charge cycle in QV plane since the charge remains constant as the capacitance varies. For any capacitor, a fixed geometry implies a fixed capacitance. As that capacitor is charged, its charge grows along the straight line defined by that capacitance. Thus, if an initially uncharged capacitor of capacitance C_{max} is brought to some voltage V_{low}, it will trace the first line segment from the origin to the point (V_{low}, Q_{high}), where $Q_{high} = C_{max}V_{low}$. A reservoir must provide

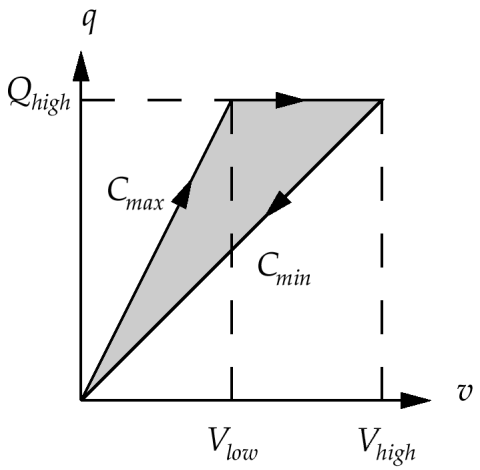

Figure 2-1: Charge-constrained energy conversion cycle.

the capacitor with an amount of energy $\frac{1}{2}C_{max}V_{low}^2 = \frac{1}{2}Q_{high}^2/C_{max}$. If the capacitor is disconnected so that no charge may flow in or out, the system will now be constrained to move along the horizontal line Q_{high}. Since the capacitor is charge-constrained, lowering the capacitance will result in a voltage increase according to

$$Q_{high} = C_{max}V_{low} = C_{min}V_{high} \Rightarrow \frac{C_{max}}{C_{min}} = \frac{V_{high}}{V_{low}} \tag{2.1}$$

This corresponds to tracing the horizontal segment from V_{low} to V_{high} in the QV plane. The energy content in the capacitor will increase to $\frac{1}{2}C_{min}V_{high}^2 = \frac{1}{2}Q_{high}^2/C_{min}$. Note that the reservoir does not provide or receive any energy during this path segment. All the energy gained comes from the mechanical source through the force required to change the capacitance. Derivation of these forces is described in Appendix A. By substituting the relationship between V_{low} and V_{high} of Equation 2.1, the energy inside the capacitor can be compared to its initial energy $\frac{1}{2}C_{max}V_{low}^2$:

$$\frac{1}{2}C_{min}V_{high}^2 = \frac{1}{2}C_{max}V_{low}^2\frac{C_{max}}{C_{min}} \tag{2.2}$$

Thus, the energy content has increased by the factor C_{max}/C_{min}. If this energy is then returned to a reservoir from the capacitor, which corresponds to moving back to the origin in the QV plane, now through the C_{min} line, the amount of energy gained by the reservoir

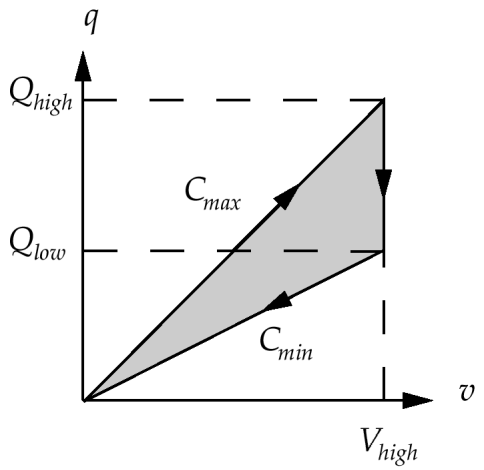

Figure 2-2: Voltage-constrained energy conversion cycle.

will be

$$\begin{aligned}\Delta E_{\text{charge constrained}} &= \frac{1}{2}C_{max}V_{low}^2\frac{C_{max}}{C_{min}} - \frac{1}{2}C_{max}V_{low}^2 \\ &= \frac{1}{2}\Delta C V_{low}^2\frac{C_{max}}{C_{min}} = \frac{1}{2}\Delta C V_{high}^2\frac{C_{min}}{C_{max}} = \frac{1}{2}\Delta C V_{low}V_{high} \end{aligned} \tag{2.3}$$

where $\Delta C = C_{max} - C_{min}$ and all the alternate forms can be derived from Equation 2.1. This quantity is equal to the shaded area inside in the cycle in Figure 2-1. Note that this converted energy will eventually be reduced by any losses incurred in the power electronics that exercise the cycle. Thus, the net converted energy will surely be less than given in Equation 2.3.

2.2 Voltage-Constrained Energy Conversion Cycle

An alternative energy conversion cycle is shown in Figure 2-2. In this cycle, aptly named a voltage-constrained cycle, a capacitor is charged up to some high voltage V_{high} when the capacitor plates are close and the capacitance is again at some C_{max}. Again, the charge at this point will be $Q_{high} = C_{max}V_{high}$, and the energy content provided by the reservoir will be $\frac{1}{2}C_{max}V_{high}^2 = \frac{1}{2}Q_{high}^2/C_{max}$. However, in this case, the plates are connected to the reservoir at constant voltage V_{high}. Thus, when the plates are separated, and the capacitance is decreased, the capacitor will trace the line from Q_{high} to Q_{low}. In order to maintain the

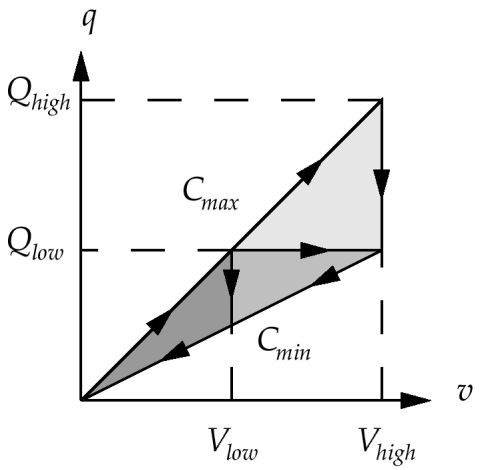

Figure 2-3: Energy cycles compared.

same voltage V_{high}, the capacitor will have to return the change in charge $Q_{high} - Q_{low}$ to the reservoir. Since the reservoir and the capacitor are held at a constant voltage V_{high}, this implies that the capacitor will provide the reservoir with an amount of energy equal to $(Q_{high} - Q_{low})V_{high}$. Again, the energy comes from the mechanical source through the force required for this capacitance change. If the capacitor is then discharged into the reservoir, it will trace the line back to the origin in the QV plane and return to the reservoir an additional amount of energy $\frac{1}{2}C_{min}V_{high}^2$. Thus, at the end of the cycle, the total amount of energy gained by the reservoir will be

$$\Delta E_{\text{voltage constrained}} = \frac{1}{2}C_{min}V_{high}^2 + (Q_{high} - Q_{low})V_{high} - \frac{1}{2}C_{max}V_{high}^2 = \frac{1}{2}\Delta C V_{high}^2 \quad (2.4)$$

Again, this is the shaded area enclosed by the cycle in Figure 2-2, and note that this converted energy will eventually be reduced by any losses incurred in the power electronics that exercise the cycle. Thus, the net converted energy will surely be less than given in Equation 2.4.

2.3 Comparison Between Cycles

Figure 2-3 shows three superimposed energy cycles. The smallest and darkest triangle corresponds to a voltage-constrained cycle where the maximum voltage is V_{low}. The darkest triangle together with the medium-shaded triangle correspond to a charge-constrained cycle

where the capacitor is first charged to V_{low}, but the decrease of the capacitance increases the voltage to V_{high}. All triangles together correspond to another voltage-constrained cycle where the maximum voltage in this case is V_{high}. Recalling that the energy gained by the reservoir at the end of the cycle is equal to the total area inside the cycle, it is easy to see that, for the same values of C_{max} and C_{min}, a voltage-constrained cycle where the maximum voltage is V_{high} will be the one to convert the most amount of energy.

However, the V_{high} voltage-constrained cycle requires a reservoir at voltage V_{high}, whereas the charge-constrained cycle only needs to be charged to V_{low}; it will reach a maximum voltage V_{high} by virtue of charge conservation. The levels of energy to be harvested by this system are likely to be useful only in very-low-power applications, where the voltage levels are typically low [10]. A system where the harvesting occurred at some voltage V_{high} would need a DC-DC converter to bring this voltage down to a useful level. Such an overhead in efficiency would have to be counted against the system. The net result is that a system with one reservoir voltage at some voltage less than V_{low} is probably preferable so that it is studied further here.

If the system has only a voltage source V_{low}, then the voltage-constrained conversion can only reach V_{low}. From Figure 2-3, it is easy to see that the charge-constrained cycle which reaches V_{high} converts far more energy in this case.

Furthermore, a constant-charge is quite easily implemented with a charge pump. While the capacitor is changing from C_{max} to C_{min} a constant-charge path can be made by simply disconnecting the variable capacitor. Implementation of a voltage-constrained cycle using a single voltage source is harder. These issues will be discussed further in the electronics chapter.

Our previous discussion assumes that in the charge-constrained cycle, the voltage on the variable capacitor can rise as high as it may. However, this maximum voltage might be limited by the maximum voltage the electronics can sustain, or by electric breakdown. In this case, Figure 2-4 shows the resulting effect. Since the charge-constrained cycle, shown in horizontal hatching, cannot go beyond V_{high}, it must be discharged as soon as it reaches that limit. Thus, the capacitor must be discharged at some intermediate capacitance $C_{max}\frac{V_{low}}{V_{high}} > C_{min}$, before it actually reaches C_{min}. In this case, a voltage-constrained cycle, shown in vertical

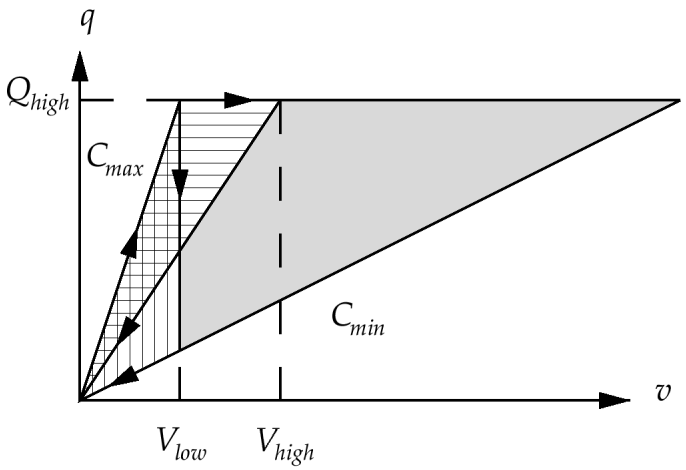

Figure 2-4: Energy cycles compared.

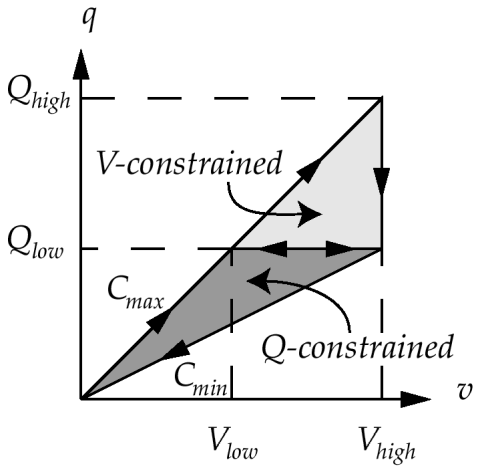

Figure 2-5: Energy cycles compared. The direction in the segment separating the two triangles depends on which cycle is occurring.

hatching, although still limited to V_{low}, can span the full range of capacitance change from C_{max} to C_{min}. Which cycle converts more energy will depend on the relative values of C_{max}, C_{min}, V_{low} and V_{high}. Also, the control system requires some form of sensing the V_{high} limit, which can increase its complexity considerably.

The circuit implementation of a voltage-constrained cycle shown in Figure 3-1 does not fully discharge the variable capacitor. Instead, it disconnects the variable capacitor when it reaches C_{min}, and charges the capacitor again when it reaches C_{max}. The energy conversion cycle corresponds to the upper triangle shown in Figure 2-5. Meanwhile, the circuit implementation of a charge-constrained cycle shown in Figure 3-2 discharges the variable

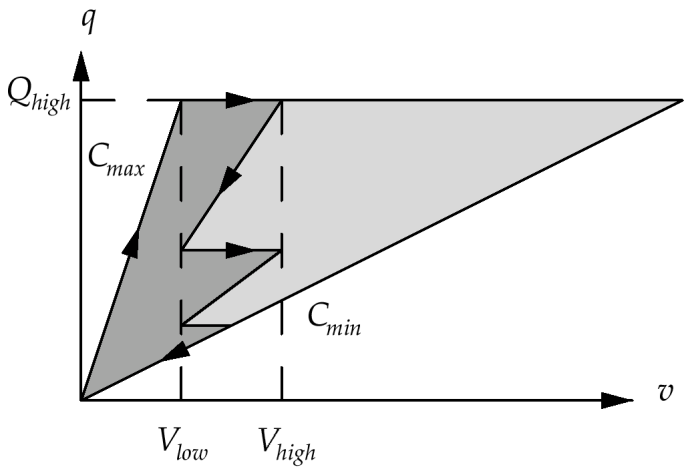

Figure 2-6: "Chatter" energy conversion cycle.

capacitor fully once it reaches C_{min}. Thus, this circuit implements the bottom triangle in Figure 2-5. The triangles share a common base, thus, the ratio of the areas, and hence, of the energy converted by each cycle is simply

$$\frac{\Delta E_{\text{voltage constrained,cropped}}}{\Delta E_{\text{charge constrained}}} = \frac{C_{max} - C_{min}}{C_{min}} \tag{2.5}$$

where $\Delta E_{\text{voltage constrained,cropped}}$ is the energy converted by the cycle surrounding the upper triangle and $\Delta E_{\text{charge constrained}}$ is the energy converted by the cycle surrounding the lower triangle. Given C_{max} and C_{min} for a specific variable capacitor, it is easy to determine which conversion will convert more energy. However, the voltage-constrained cycle still needs a high voltage reference, and it operates with higher voltages and currents, making it likely that the losses incurred by the associated power electronics will be higher.

2.4 "Chatter" Energy Conversion Cycle

The charge-constrained cycle does not have to completely lose all its energy upon reaching V_{high} for the first time. The discharging of the capacitor can be stopped as soon as the voltage reaches V_{low}, as shown in Figure 2-6. Since the capacitance will still decrease, the voltage in the capacitor will rise again. If it reaches V_{high} again, the capacitor can again be discharged until the voltage reaches V_{low}. This process can continue until the capacitor reaches C_{min}, at

which point the capacitor can be fully discharged. By "chattering" in this manner between V_{high} and V_{low}, the resulting cycle will convert an amount of energy larger than a V_{low} voltage-constrained cycle, but still smaller than a V_{high} voltage-constrained cycle. With a sufficiently small-scale chattering, the electronics that implement a charge-constrained cycle can be made to implement a voltage-constrained cycle.

The amount of energy converted by a chatter cycle can be computed by subdividing the complete cycle into a sequence of charge-constrained cycles, where each sub-cycle converts an amount of energy $\frac{1}{2}Q_i(V_{high} - V_{low})$ and Q_i is the constant charge of each cycle. For the first cycle, $Q_{high} = C_{max}V_{low}$. For each consecutive cycle, $Q_{i+1} = Q_i\frac{V_{low}}{V_{high}}$, assuming that all cycles start at V_{low} and end at V_{high}. In particular, if $C_{min} \to 0$, the total energy converted will be

$$\Delta E_{\text{chatter}} = \frac{1}{2}Q_{high}(V_{high} - V_{low})\left[1 + \frac{V_{low}}{V_{high}} + \left(\frac{V_{low}}{V_{high}}\right)^2 + ...\right] = \frac{1}{2}C_{max}V_{low}V_{high} \qquad (2.6)$$

Furthermore, if $V_{low} \to V_{high}$, the energy converted approaches that of a voltage-constrained cycle where $C_{min} \to 0$, as expected.

The problem with the chatter cycle is that the charge transport to and from the reservoir is inevitably lossy. In the simple charge constrained cycle, the capacitor is charged and discharged only once per cycle. The losses associated with the repeated charging and discharging of the capacitor in the chatter cycle will likely offset the benefit obtained from converting extra energy. Furthermore, the control system will be more complicated, presumably adding to its energy tax, and decreasing the overall reliability of the system. It will also need a more active sensing circuit which will further add to the energy tax.

2.5 Added Parallel Capacitance

Another way to increase the energy converted in a charge-constrained cycle is to add a constant capacitance in parallel to the variable capacitance. The resulting cycle is shown in

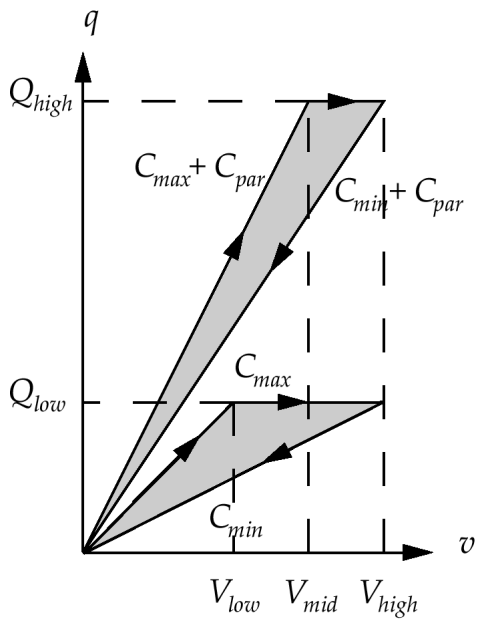

Figure 2-7: Charge-constrained cycle with extra capacitance.

Figure 2-7. The energy gained in the original cycle is

$$\Delta E_{\text{charge constrained}} = \frac{1}{2}\Delta C V_{high}^2 \frac{C_{min}}{C_{max}} \tag{2.7}$$

Adding a constant capacitance in parallel only increases the value of C_{min} and C_{max} by the same amount. Thus, the energy converted by the cycle with a parallel capacitance is

$$\Delta E_{\text{charge constrained, parallel}} = \frac{1}{2}\Delta C V_{high}^2 \frac{C_{min} + C_{par}}{C_{max} + C_{par}} \tag{2.8}$$

As $C_{par} \to \infty$, the fraction $\frac{C_{min}+C_{par}}{C_{max}+C_{par}} \to 1$ and $\Delta E_{\text{charge constrained, parallel}} \to \Delta E_{\text{voltage constrained}}$. Thus, by adding a parallel capacitor, the energy conversion cycle of a charge-constrained cycle approaches that of the voltage-constrained cycle. However, the same problem arises again: by adding more capacitance, the amount of charge to be transported increases accordingly. Therefore, any gain in energy must be weighed against the extra losses incurred by the transport of extra charge through the power electronics.

Note that adding a parallel capacitance to a voltage-constrained cycle will not change the energy converted by the cycle, and will only add to losses in the transport of extra charge. Therefore, in a voltage-constrained cycle, C_{min} should always be as small as possible.

2.6 Summary

A voltage-constrained cycle requires a voltage source at some high voltage. Such a high voltage source requires a voltage level conversion which may render it useless. Alternatively, a high voltage cycle can be approached by chattering at high voltages. However, sensing requires a high-voltage reference and, likely, analog circuitry that will be lossy. A more important objection is that charge is being transported continuously back and forth during chattering, resulting in substantial losses through the power electronics.

A charge-constrained cycle is easier to implement with a charge pump. Furthermore, the voltage of the reservoir is completely divorced from all voltages in the cycle. The value of V_{low} is set by the amount of charge pumped into the capacitor, and V_{high} is set by the change from C_{max} to C_{min}, although this requires a careful design to avoid a V_{high} which may destroy the power electronics. Therefore, this thesis will adopt a charge-constrained energy conversion cycle.

As a baseline, consider a charge-constrained cycle where a C_{max} of 168 pF is charged to 17.7 V. This represents 26.4 nJ of energy into the capacitor. Allowing the capacitor to decrease to a C_{min} of 89 pF, V_{high} will be 33.5 V. The final energy in the capacitor will be 49.8 nJ, which represents a gain of 23.4 nJ. This cycle will be developed in theory throughout the thesis as the basis for a realizable design. The values of C_{min} and C_{max}, as well as V_{high} and V_{low}, and the energy gain are consistent with the design which will be found in future chapters.

Chapter 3

Power Electronics

Suitable electronics must be used to implement the energy conversion cycles discussed in Chapter 2. These electronics may be divided into three sub-circuits: power electronics, control electronics, and sensing electronics. Each is described below, with an emphasis on the power electronics.

The power electronics are responsible for the actual transport of energy to and from the variable capacitor. They should be able to deliver charge to the capacitor, extract charge from the capacitor, hold a constant charge in the capacitor, and/or hold a constant voltage across it. The "and/or" indicates that, depending on the conversion cycle to be implemented, the power electronics may not necessarily have to perform all these functions. The power electronics should also be designed to minimize energy loss during energy transport. Note that energy loss in the power electronics will occur only when energy is transported, and that this loss will scale up with the energy converted in the conversion cycle.

The control electronics are responsible for telling the power electronics when to perform its different functions. Depending on its design, this circuit may use energy all of the time. A more clever design would "wake up" the control electronics whenever they are needed, in which case they would only use energy during a few short periods. In any case, the energy lost in this circuit will not depend on the energy converted in the conversion cycle.

The sensing electronics should provide the control electronics with the information necessary to decide when different events should take place. It is critical to design the sensing electronics such that they drain as little energy from the power electronics as possible. More

than likely, the energy lost in the sensing circuit will scale up with the energy converted in the conversion cycle. The sensing will likely have to occur all of the time, in which case, the energy loss associated with these electronics will be constant in time. However, again, clever design may either actively predict when the sensing is going to be needed, or a passive form of sensing may be employed in which the energy loss will occur only during short periods.

This thesis will concentrate on the power electronics. Other papers [4, 26] have explored the design of sensing and control electronics for this application using the design rules of Very-Low-Power Electronics. Control electronics have also been designed for this application [25]. From these results, it is likely that the bulk of the loss during each cycle will be in the power electronics. In any case, the conclusions in this thesis concerning losses will give minimal requirements for the harvesting of net power. In particular, the following analysis will assume perfect, lossless sensing and control, that is, the power electronics will be assumed to have the necessary information and intelligence to operate as expected. Subsequent work which includes control and sensing losses will only increase those minimal requirements.

3.1 Voltage-Constrained Cycle Implementation

To implement a voltage-constrained cycle, the power electronics must perform three different functions: charge the variable capacitor to the same voltage as the reservoir, hold the capacitor voltage constant as the variable capacitance C_M goes from C_{max} to C_{min}, and finally discharge the remaining charge into the reservoir. As explained in the previous chapter, this cycle suffers from the drawback that there must exist a voltage source at some high voltage. In order to make this voltage available to low power electronics, it must be converted to a low level. Furthermore, as C_M goes from C_{max} to C_{min}, charge must be transferred continuously from the capacitor to the reservoir. This transfer is lossy and will likely dissipate any useful energy that may be obtained from the conversion cycle.

Figure 3-1 shows a circuit which implements the cropped voltage conversion cycle described in Section 2.3. This circuit consists of two sequential charge pumps, borrowing from DC-DC converter technology [18]. In the figure, the high-voltage reservoir is implemented using a capacitor C_R. In this design, MOSFET M_1 is turned on to charge the inductor. This

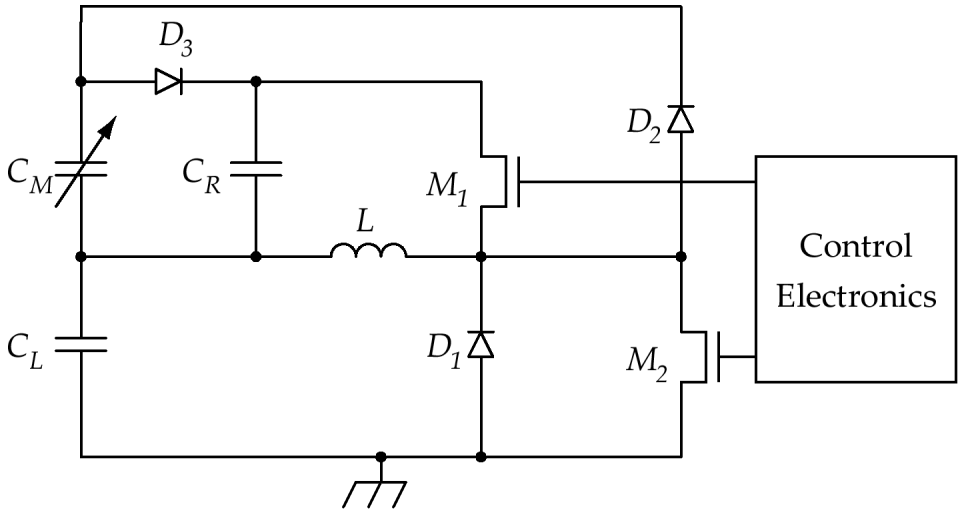

Figure 3-1: Power electronics circuit implementing a voltage-constrained cycle.

transfers energy from the high-voltage reservoir C_R into the inductor. Once the inductor is charged to the desired current, MOSFET M_1 is turned off and the current charges the low-voltage reservoir C_L through D_1. The low-voltage reservoir can be used to power a load. To charge the variable capacitor C_M, MOSFET M_2 is turned on to again charge the inductor. This transfers energy from the low-voltage reservoir C_L into the inductor. Once the inductor is charged to the desired current, MOSFET M_2 is turned off and the current charges the variable capacitor C_M through D_2. Once the inductor is discharged, the MOSFET M_2 is turned off. As C_M goes from C_{max} to C_{min}, diode D_3 will turn on and keep C_M at the same constant voltage as C_R while charge is transferred from C_M to C_R. When the capacitance reaches C_{min}, diode D_3 turns off, isolating the variable capacitor C_M. As C_M goes from C_{min} to C_{max}, its voltage will decrease until it reaches C_{max}. When C_M reaches C_{max}, MOSFET M_2 is turned on again to charge C_M, repeating the cycle. In the mean time, MOSFET M_1 will be turned on and off as necessary to keep transferring energy from the high-voltage reservoir C_R to the low-voltage reservoir C_L so as to keep the voltage across C_L from decreasing. Note that the inductor is shared by both loops in opposite directions, thus, the control will have to be smart enough to avoid turning both MOSFETs on at the same time. The diodes can be replaced by MOSFETs to improve efficiency, and D_1 can be eliminated by using M_2. In addition, by using MOSFETs in place of diodes the variable

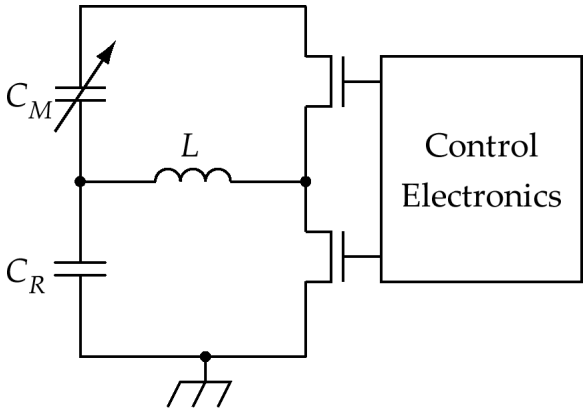

Figure 3-2: Power electronics circuit implementing a charge-constrained cycle.

capacitor C_M can be fully discharged to implement the full voltage-constrained cycle. If the components are all ideal, the circuit in Figure 3-1 is a lossless circuit.

The voltages and currents in this cycle are larger than in a comparable charge-constrained circuit implementation. This implies that the energy loss in the components will be higher and the efficiency of the energy transport will be lower. Also, more intelligent control and voltage sensing should require more power than in a charge-constrained cycle. Nevertheless, further investigation is required to determine the feasibility of this or other circuits implementing a voltage-constrained conversion cycle, specially in an application where a high voltage reservoir is present or desirable. It is not considered further here because of its apparent poor electronic efficiency.

3.2 Charge-Constrained Cycle Implementation

The implementation of a charge-constrained cycle requires electronics that charge the capacitor to a desired voltage, hold the charge in the capacitor as C_M goes from C_{max} to C_{min} and finally discharge the capacitor back into the reservoir. A simple way to realize this circuit is to design a charge pump. Borrowing from DC-DC converter technology [18], the circuit chosen to validate experimentally is presented in Figure 3-2. In the figure, the reservoir is implemented using a capacitor C_R. In this design, the bottom MOSFET is turned on to charge the inductor to some current. This transfers some energy from the reservoir into the inductor. Once the inductor is charged to the desired current, the bottom MOSFET

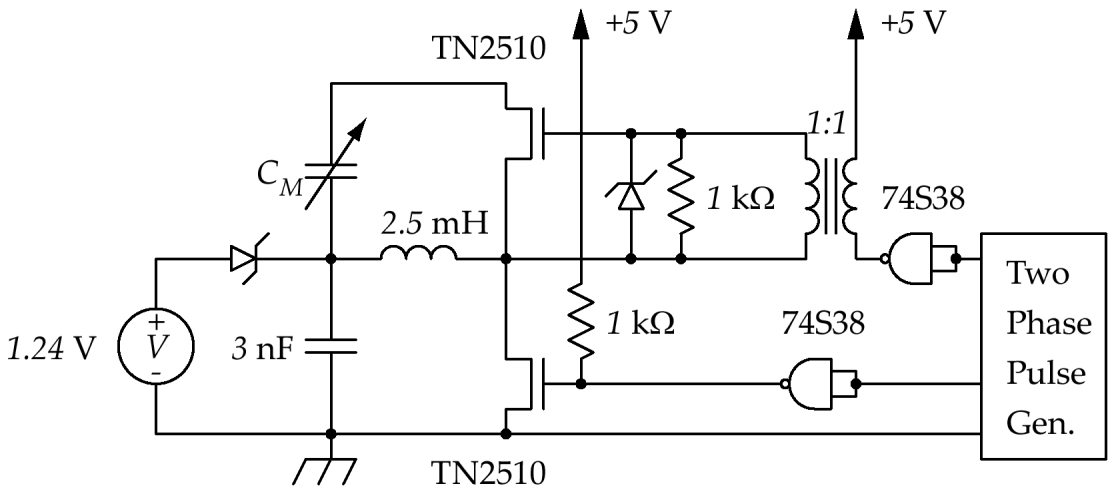

Figure 3-3: Power electronics circuit schematic.

is turned off and the top MOSFET is turned on. The current in the inductor is forced to discharge into the variable capacitor C_M, charging it as desired and transferring all of its energy into the variable capacitor C_M. Once the inductor is discharged, the top MOSFET is also turned off, isolating the variable capacitor as C_M goes from C_{max} to C_{min} and hence keeping its charge constant. When the capacitance reaches C_{min}, the process to discharge the variable capacitor C_M starts. The top MOSFET is turned on to charge the inductor (now in the opposite direction) and transfers all the energy from the capacitor back into the inductor. Once the top capacitor is fully discharged, the top MOSFET turns off and the bottom MOSFET turns on. The current in the inductor is then discharged into the reservoir C_R, and the energy in the inductor is returned to the reservoir. If the components are all ideal, the circuit in Figure 3-2 is a lossless circuit.

The test circuit shown in Figure 3-3 implements a charge-constrained cycle. Its circuit model will be discussed below. This model is validated by comparing a numerical simulation of the model with experimental results of the test circuit.

A 3 nF capacitor is used as the reservoir capacitor. The voltage source V is set at 1.24 V. The saturation current which models the exponential diode is 10^{-14} A, which provides the correct voltage drop measured experimentally. The voltage source V and the diode keep the voltage in the reservoir from dropping to zero if the system does not convert energy sufficient energy to sustain itself. In particular, the voltage source V and diode provide charge to the

reservoir if its voltage goes below 0.6 V. The voltage source V and diode would not exist in a real implementation, although the question of the initial reservoir charge must still be addressed and will be discussed in Chapter 8.

The inductor is characterized using a bridge at a frequency of 10 Hz to measure the DC resistance. The measured inductance is $L = 2.5$ mH, and the DC resistance is $R_L = 8\ \Omega$. The measurement frequency for the core losses, 300 kHz, is the resonant frequency of the inductor and the MOSFET output capacitances, which dominate when both MOSFETs are off. The measured core loss is modeled as a resistance of 360 kΩ in parallel with the inductor. However, setting $R_C = 360$ kΩ in the model results in a slower decay than observed experimentally, probably due to unaccounted losses in the real circuit. Also, the core loss is measured in the bridge at a low voltage, and hence low flux density. The voltages in the test circuit are higher, corresponding to higher losses per volt. The core loss resistor in the model is therefore set at $R_C = 200$ kΩ to account for this discrepancy.

The MOSFETs in the circuit are vertical MOSFETs which have a parasitic diode from source to drain. These diodes may be used to transfer the energy of the inductor once it is charged, and eliminate the need to turn on the corresponding MOSFET for reverse current flow. In practice, however, the parasitic diode is not designed to transfer power and is very lossy. Thus, they are usually bypassed by placing better diodes in parallel with the MOSFETs, or turning on the MOSFET whenever the diode is forward biased so that the current flows through the MOSFET channel instead. Nevertheless, the parasitic diodes are used for energy transport in the experimental validation for the model in order to fully corroborate the MOSFET model.

The data sheet for the TN-2510 MOSFET, included in Appendix D, provides values for the MOSFET model. The ON channel resistance is $R_F = 1.5\ \Omega$, and the saturation current used for the exponential diode is 10^{-30} A, which corresponds to a 1.8 V voltage drop at 1.5 mA. The output capacitance in the model is $C_F = 95$ pF. This is a rough approximation from the data sheet since the output capacitance of a MOSFET increases as the voltage approaches zero.

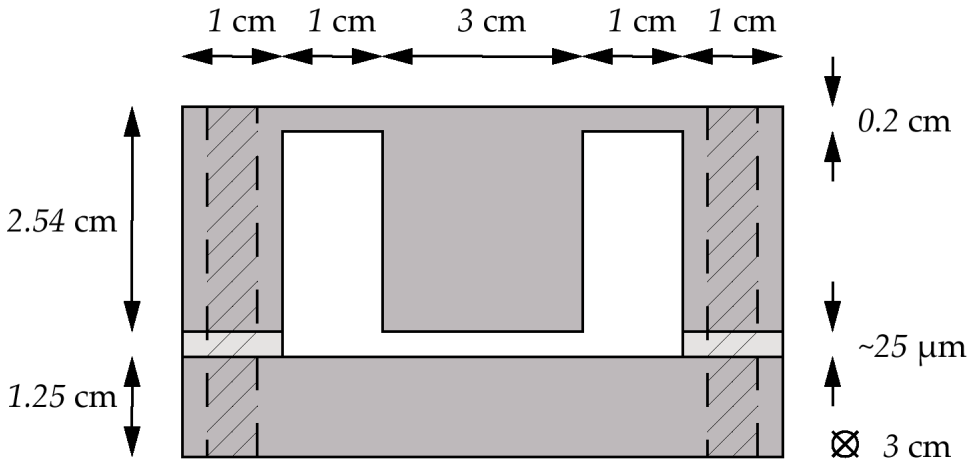

Figure 3-4: Variable capacitor. Dimensions not to scale. The structure is all aluminum. The lighter areas represent Mylar® tape which isolates the two pieces and creates a gap of about 25 μm.

3.3 Variable Capacitor

The variable capacitor, shown in Figure 3-4, consists of a 3 cm $\times$ 3 cm variable-gap, parallel-plate capacitor. The capacitor is built from a solid block of aluminum. A pair of grooves are milled to create beam springs 0.2 cm thick, 1 cm long and 3 cm wide. The two pieces are isolated using 25 μm-thick Mylar® tape on the extremes. The two pieces are joined using screws with nylon washers for electrical isolation.

The capacitance of the device with no shaking is measured with a differentiator circuit and a bridge to be $C_M = 500$ pF. This capacitance is in reasonable agreement if the total area is increased to $(3.5 \text{ cm})^2$ to account for the capacitance of the end columns, and the gap is assumed to be 20 μm to account for compression of the Mylar® tape by the screws. The theoretical capacitance in this case is 540 pF. Another resistor R_M is placed in parallel with the variable capacitor C_M in its model to represent any lossy leakage path for the current in the physical capacitor. The parallel resistance measured with a bridge is $R_M = 10$ MΩ.

The device is fastened to a shaker table and driven with a PA-1000L amplifier, both from Ling Dynamic Systems. The amplifier is driven by a signal generator at 3.8 kHz. This frequency corresponds the mechanical resonant peak of the variable capacitor C_M which provides the largest capacitance variation, and hence, produces the largest voltage variation across it. Three experiments are performed using the test circuit. In each experiment, the

variable capacitor is driven with no shaking, medium shaking and maximum shaking. The maximum shaking corresponds to an input signal of 400 mV peak-to-peak into the PA-1000L amplifier. Higher voltage trips the protection circuitry in the PA-1000L.

The variable capacitor is enclosed in a bag with desiccant and pumped with nitrogen to avoid the formation of water between the plates of the capacitor. Even with this arrangement, water still forms between the plates of the capacitor after about 15 seconds of heavy shaking. Apparently, the speed at which the plates separate is fast enough to reduce the local pressure below the vapor pressure of water and induce the condensation of water from the moisture present in the air. This water dramatically decreases the value of the parallel resistance R_M.

3.4 Pulse Generator

The pulse generator is a pair of TTL 74LS123 monostable multivibrators. They generate pulses of variable length with variable delay using the reference signal from the acceleration source. Thus, the pulses have the same frequency as the acceleration. These pulses turn on the MOSFETs at the desired times in the energy conversion cycle for the desired duration. The delay and duration are set manually to maximize energy conversion, and measured afterward so that they could be introduced in the model. By manually changing the delays, the phase of the pulse generator can be altered arbitrarily.

The on-time of the bottom MOSFET to charge the inductor from the reservoir is defined as t_{charge}. This time in the model is the same as measured, $t_{\text{charge}} = 19.4\mu s$. The on-time of the bottom MOSFET to discharge the variable capacitor into the inductor is defined as $t_{\text{discharge}}$. However, this time in the model was set at $t_{discharge} = 6.2\mu s$, about three times as long from the measurement, in order to correspond with the experimental results. The discrepancy can be explained by noting that the discharge pulse must travel through a transformer and an extra protection diode and resistor, which may slow the speed at which the input capacitance of the top MOSFET can be charged and discharged. The duty cycle, defined as the time the variable capacitor is charged over the total time in one energy conversion cycle, is also set manually to maximize energy conversion and is measured as 62%.

Note that neither the drain nor the source of the top MOSFET are held at constant voltage. If the voltage at the gate is pulsed with respect to ground, the pulse will travel through the input capacitance of the MOSFET into the power electronics. The energy present in the pulse will be rectified by the anti-parallel MOSFET diodes and will appear as energy sent to the reservoir, even when the reservoir is initially uncharged, the variable capacitor is constant and the voltage source V is disconnected. The top transformer is necessary to present the pulse across the input capacitance of the top MOSFET, while allowing the source voltage to be driven only by the power electronics circuit. Once the top transformer is added, the circuit is tested by disconnecting the voltage source V and charging the reservoir initially. The pulse generator is turned on so that the MOSFETs are switching at a frequency $f = 3.8$ kHz. The variable capacitor is not shaken. The voltage across the reservoir decays with the time constant corresponding to the oscilloscope resistance and the reservoir capacitance, as expected.

3.5 Circuit Model

A detailed model of the test circuit is shown in Figure 3-5. The dominant losses in this circuit are the inductor series resistance and core loss, modeled by R_L and R_C respectively, the parasitic diodes D_1 and D_2 present in the MOSFETs, the channel losses in the MOSFETs, modeled by R_{F1} and R_{F2}, and the output capacitance of the MOSFETs, modeled by C_{F1} and C_{F2}. While the MOSFET capacitors are lossless, their presence gives rise to substantial loss mechanism since they become fully charged when the MOSFET is open and this energy is lost when MOSFET turns on and the capacitors are shorted by the MOSFET channel resistance.

The resistors R_{S1} and R_{S2} represent the losses associated with scope probes, which will be necessary to corroborate the experimental results. They will not be present in a real implementation. The oscilloscope probes have the resistance $R_S = 10M\Omega$. Their capacitance $C_S = 10$ pF may be ignored compared to the capacitances present in the rest of the circuit.

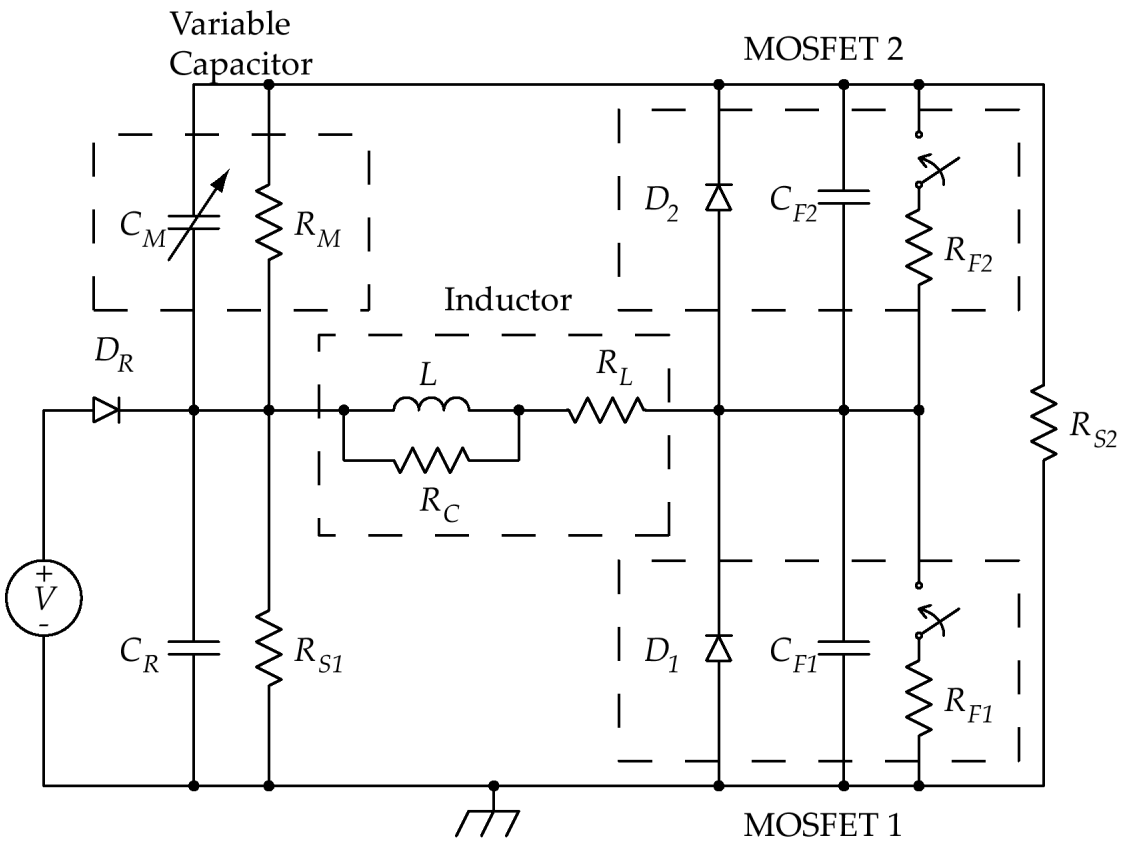

Figure 3-5: Detailed model of power electronics.

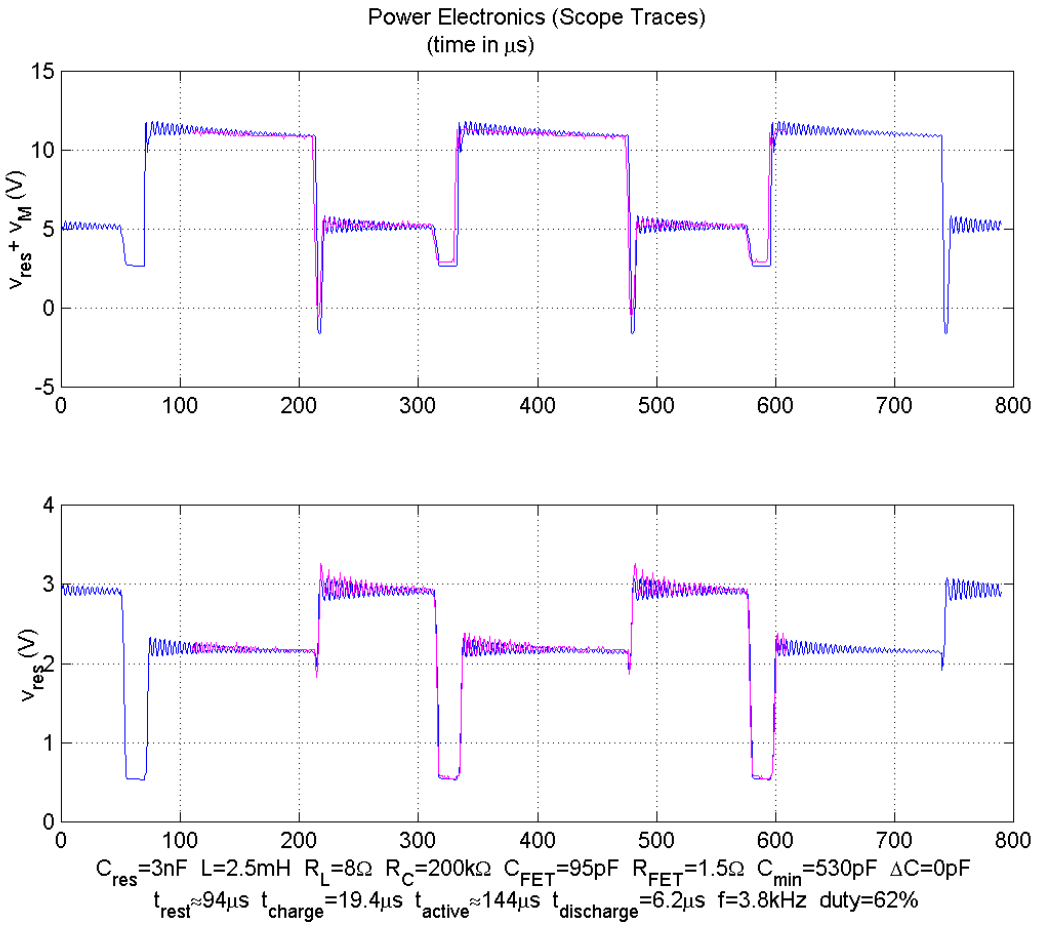

Figure 3-6: Experimental measurements and simulation results combined. The top trace is the voltage at the top of the MOSFETs. The bottom trace is the voltage at the reservoir. The light purple traces are the measured voltages in the test circuit. The blue traces are the simulation results. The bottom lists the values and timing parameters used for the model in Appendix B. The input to the shaker amplifier is 0 mV peak-to-peak.

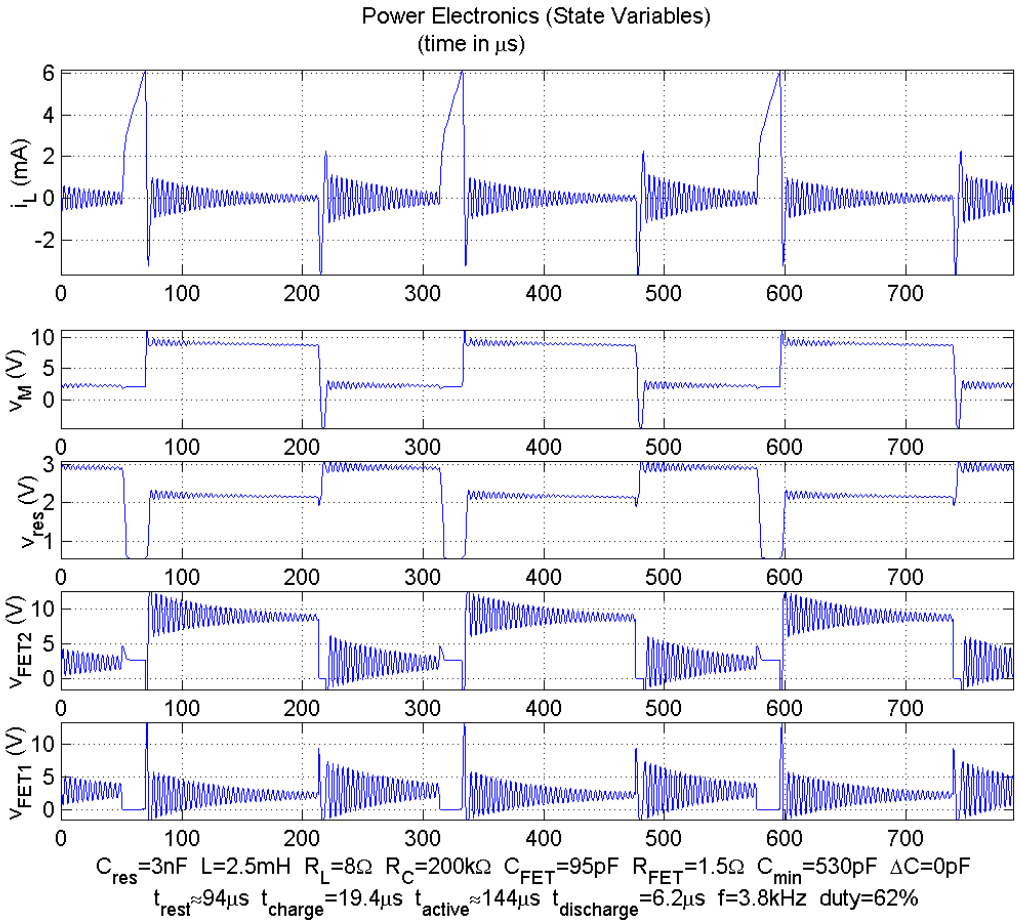

Figure 3-7: State variables of the simulation. The bottom lists the values and timing parameters used for the model in Appendix B. The input to the shaker amplifier is 0 mV peak-to-peak.

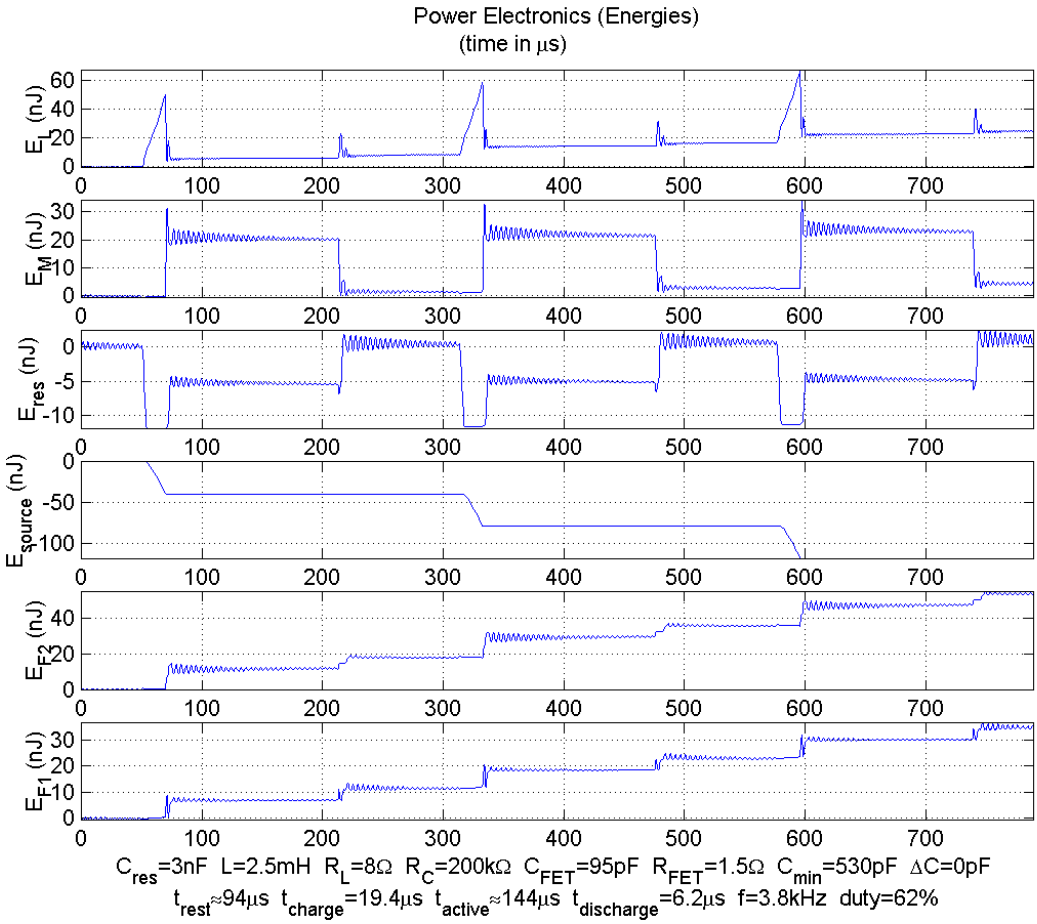

Figure 3-8: Energy absorbed and returned by each element in the simulation. The bottom lists the values and timing parameters used for the model in Appendix B. The input to the shaker amplifier is 0 mV peak-to-peak.

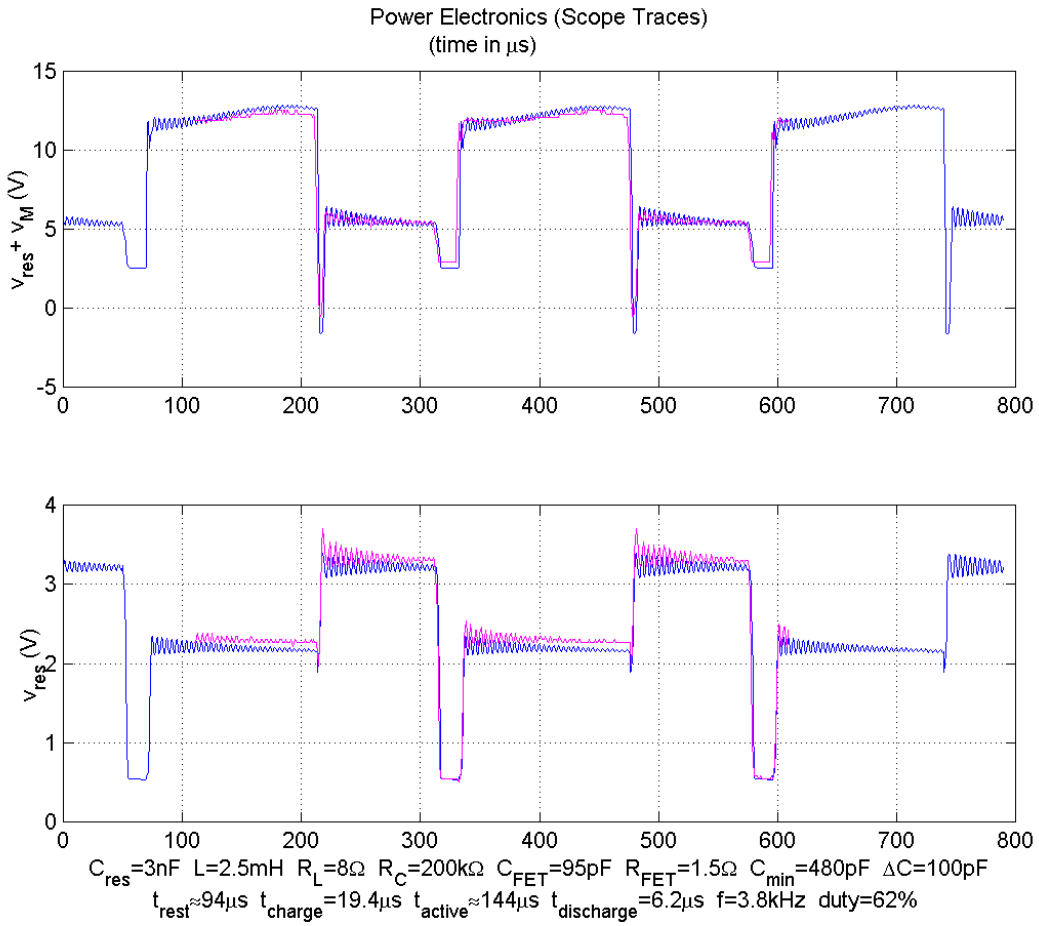

Figure 3-9: Experimental measurements and simulation results combined. The top trace is the voltage at the top of the MOSFETs. The bottom trace is the voltage at the reservoir. The light purple traces are the measured voltages in the test circuit. The blue traces are the simulation results. The bottom lists the values and timing parameters used for the model in Appendix B. The input to the shaker amplifier is 200 mV peak-to-peak.

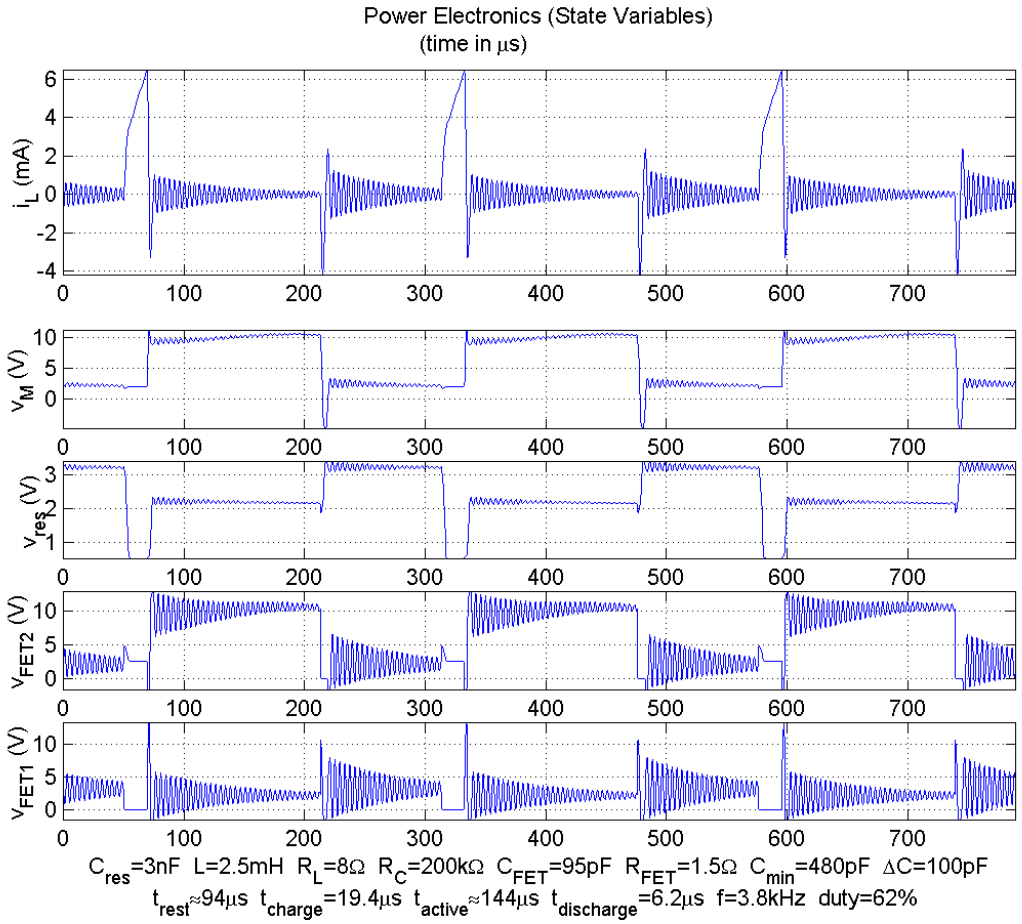

Figure 3-10: State variables of the simulation. The bottom lists the values and timing parameters used for the model in Appendix B. The input to the shaker amplifier is 200 mV peak-to-peak.

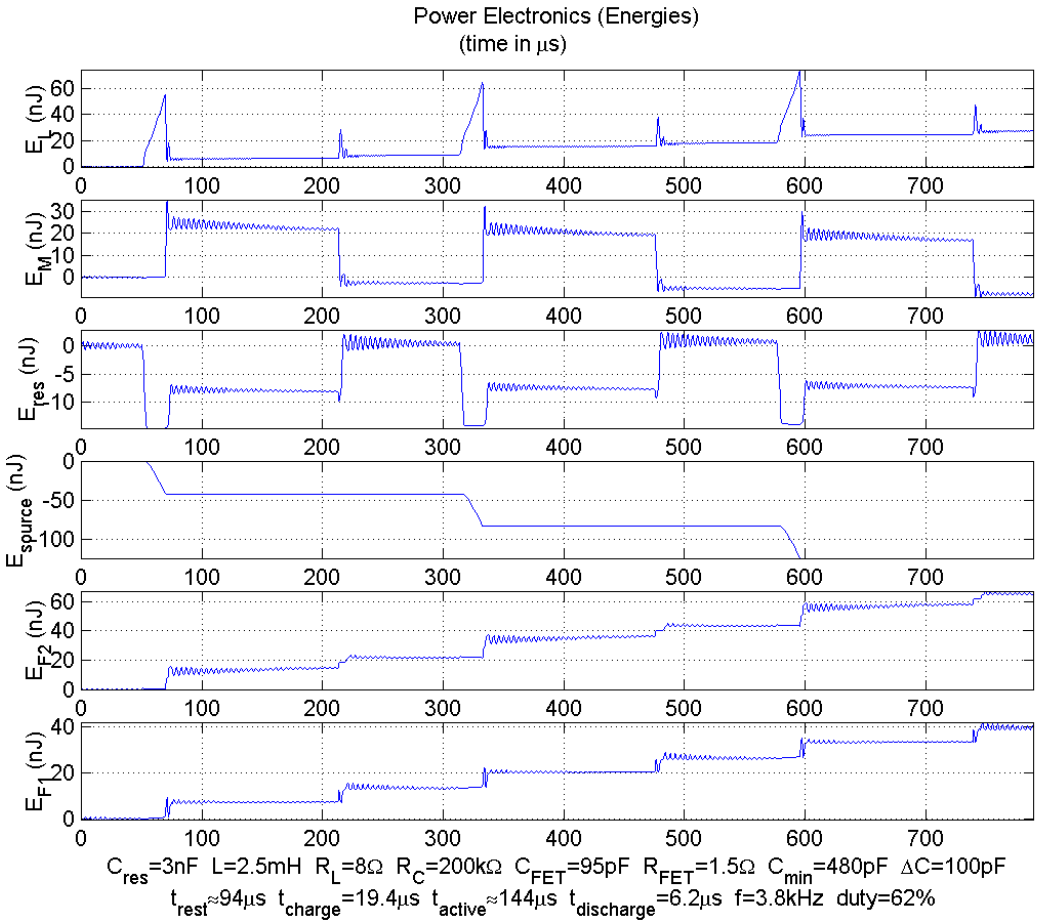

Figure 3-11: Energy absorbed and returned by each element in the simulation. The bottom lists the values and timing parameters used for the model in Appendix B. The input to the shaker amplifier is 200 mV peak-to-peak.

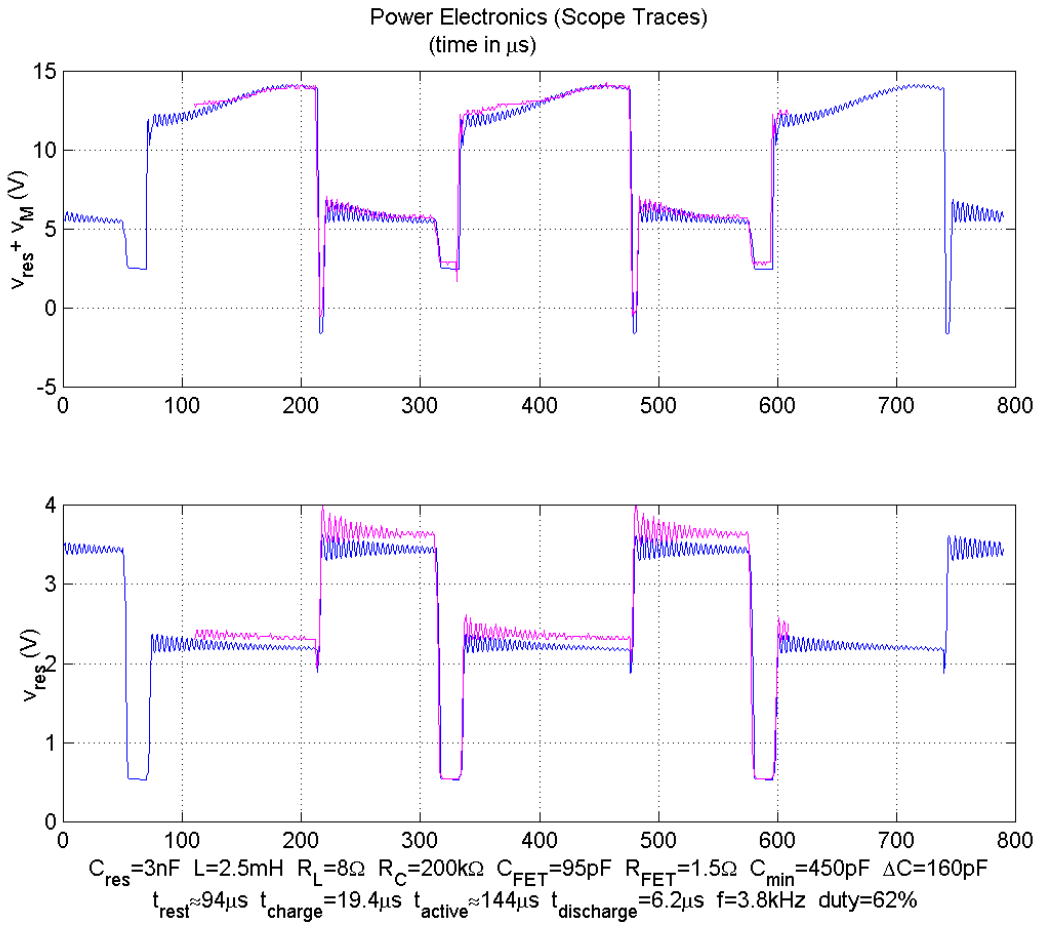

Figure 3-12: Experimental measurements and simulation results combined. The top trace is the voltage at the top of the MOSFETs. The bottom trace is the voltage at the reservoir. The light purple traces are the measured voltages in the test circuit. The blue traces are the simulation results. The bottom lists the values and timing parameters used for the model in Appendix B. The input to the shaker amplifier is 400 mV peak-to-peak.

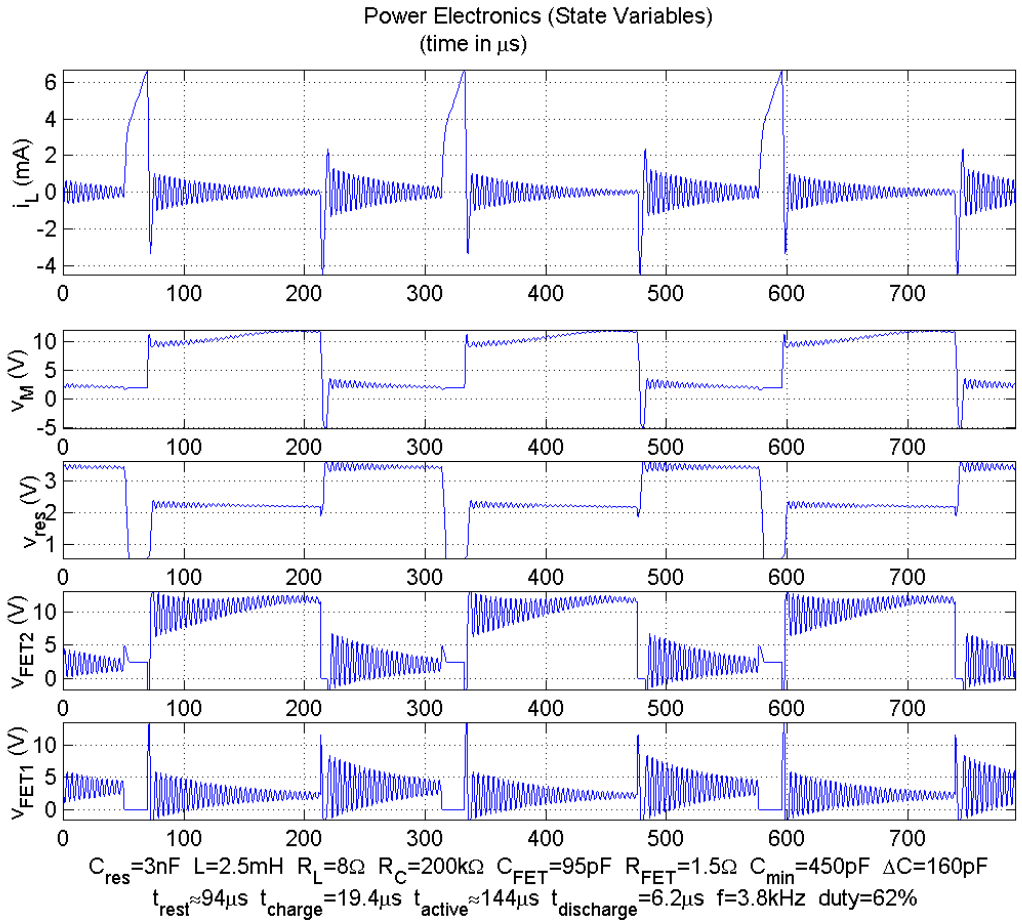

Figure 3-13: State variables of the simulation. The bottom lists the values and timing parameters used for the model in Appendix B. The input to the shaker amplifier is 400 mV peak-to-peak.

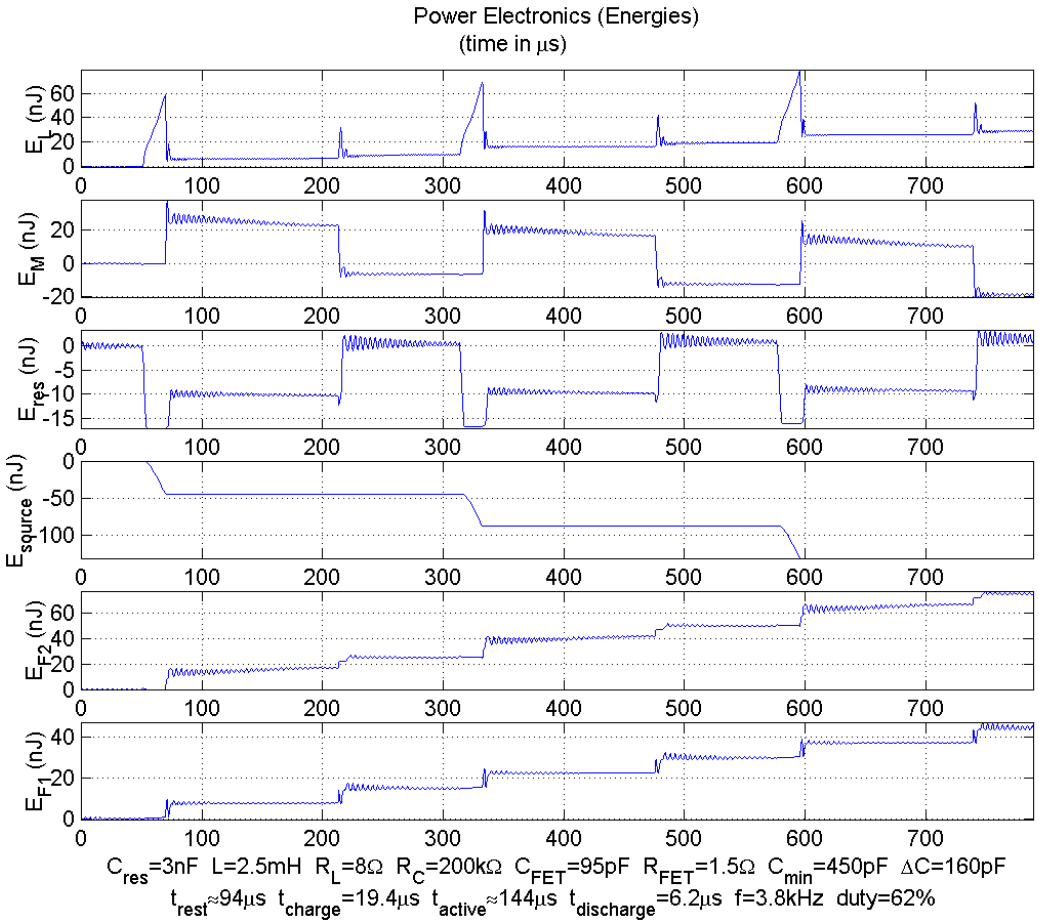

Figure 3-14: Energy absorbed and returned by each element in the simulation. The bottom lists the values and timing parameters used for the model in Appendix B. The input to the shaker amplifier is 400 mV peak-to-peak.

In order to validate this model, the circuit was simulated numerically using MATLAB®. The derivation of the state equations is in Appendix B and the MATLAB® program is given in Appendix C. The experimental results and the corresponding model simulations are shown in Figures 3-6, 3-9 and 3-12, corresponding to no shaking, medium shaking and maximum shaking. Figures 3-7, 3-10 and 3-13 show the state variables of each simulation. Figures 3-8, 3-11 and 3-14 show the energy absorbed and returned by each element during each simulation.

The variable capacitor in the simulation is of the form

$$C_M = C + \Delta C \sin(\omega t) \tag{3.1}$$

where $C_{min} = C - \Delta C$ and $C_{max} = C + \Delta C$. The value of C for the simulation which best fits the experimental results is 530 pF, in reasonable agreement with the theoretically expected value of 540 pF and the value obtained from bridge measurements of the device of 500 pF.

The ΔC used in the simulation that best fits the experimental results is 100 pF for medium shaking and 160 pF for maximum shaking. In both cases, the value of C is kept at 530 pF, in accordance with the no shaking results. Thus, for medium shaking, C_{min} is 480 pF and C_{max} is 580 pF. Correspondingly, the gap variation is about 9%. Assuming a nominal gap of 20 μm, this variation implies a travel amplitude of ± 1.8 μm. For maximum shaking, C_{min} is 450 pF and C_{max} is 610 pF. Following the same argument, this implies a gap variation of 15%, or ± 3 μm. The excellent match between the measured and the predicted traces validates the accuracy of the model and enables its use to predict the behavior of the power electronics constructed with other component values.

3.6 Revised Circuit

The results of the previous section validate the model of the power electronics. The power electronics will now be redesigned to perform better. The circuit model will be used to test the behavior of the redesigned power electronics, instead of building a new circuit. The

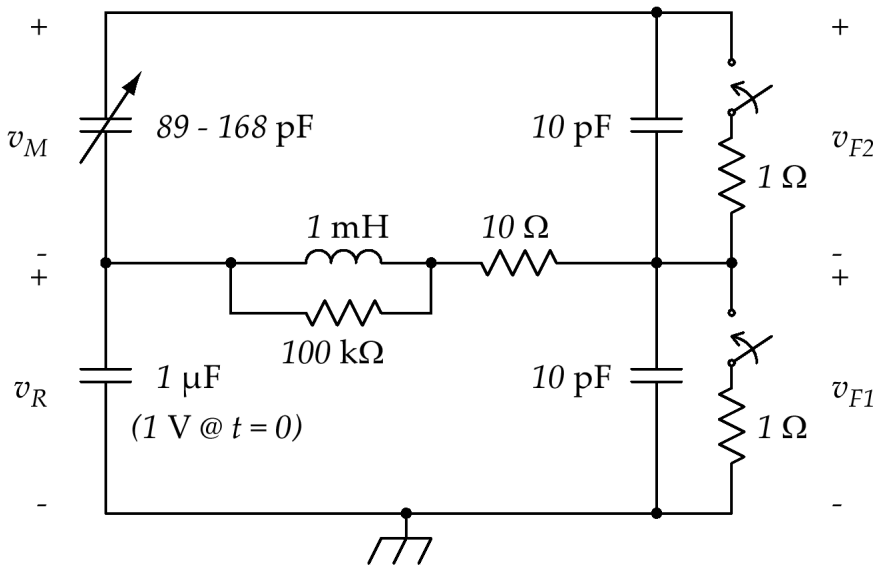

Figure 3-15: Improved power electronics for the simulation of a charge-constrained cycle. These values will be used to simulate the behavior of this circuit using the model in Appendix B. The variable capacitor will oscillate sinusoidally between C_{max} and C_{min}, as shown in the Figure, at a frequency of 2.5 kHz. In order to maximize energy conversion, the power electronics will operate at a 50% duty cycle.

redesigned circuit and its simulation will be the basis for the design of another variable capacitor structure in the rest of the thesis.

Figure 3-15 shows the circuit for the new design of the power electronics. The resistances associated with oscilloscope probes are not present. The inductor values are chosen to reflect a real inductor. The MOSFETs are now lateral. Lateral MOSFETs do not have a parasitic diode associated with them, and they have a smaller output capacitance. The MOSFETs will be switched on every time they are required to pass current. Lateral MOSFETs which do not have diodes associated with them will also prevent losses when both MOSFET are off and the circuit rings through the output capacitance of the MOSFETs. Also, MOSFETs with smaller output capacitance will minimize the loss associated with the charging and shorting of these capacitor as the MOSFETs switch on and off.

The variable capacitor will vary sinusoidally at a frequency of 2.5 kHz, in accordance to the charge-constrained cycle proposed in the previous chapter. A carefully fabricated variable capacitor should not have any appreciable leakage current so that the parallel resistance R_M may be ignored. The values of C_{min} = 89 pF and C_{max} = 168 pF, as well

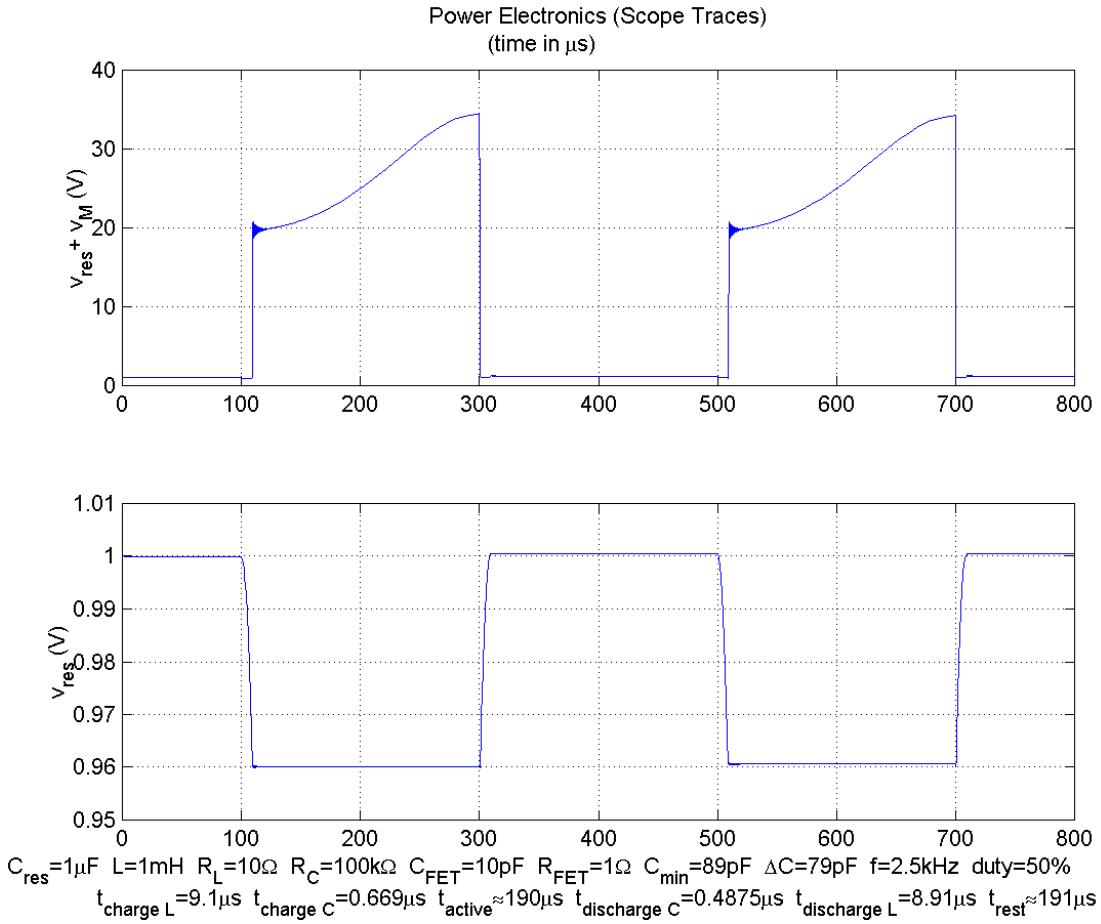

Figure 3-16: Voltage levels at the top of the circuit and the reservoir.

as the final voltage across the variable capacitor of 33.5 V were chosen using the simulation to maximize the power output while minimizing the required change of capacitance $\Delta C = C_{max} - C_{min} = 79$ pF. The final voltage across the variable capacitor was manipulated by changing the initial charging time of the inductor, $t_{\text{charge L}}$.

Finally, there is no external source or sink of power. The reservoir capacitor will be assumed to have some initial voltage, and successful energy conversion will show the voltage level rise after energy is returned at the end of the conversion cycle.

Figure 3-16 shows the simulated voltages where the oscilloscope probes were located in the experimental test circuit. Note the change in the voltage of the top trace (v_M) as C_M goes from C_{max} to C_{min}, and the rise in voltage of the reservoir (v_{res}). Figure 3-17 shows all the voltages and the current in the circuit. Note that the final value of the voltage across

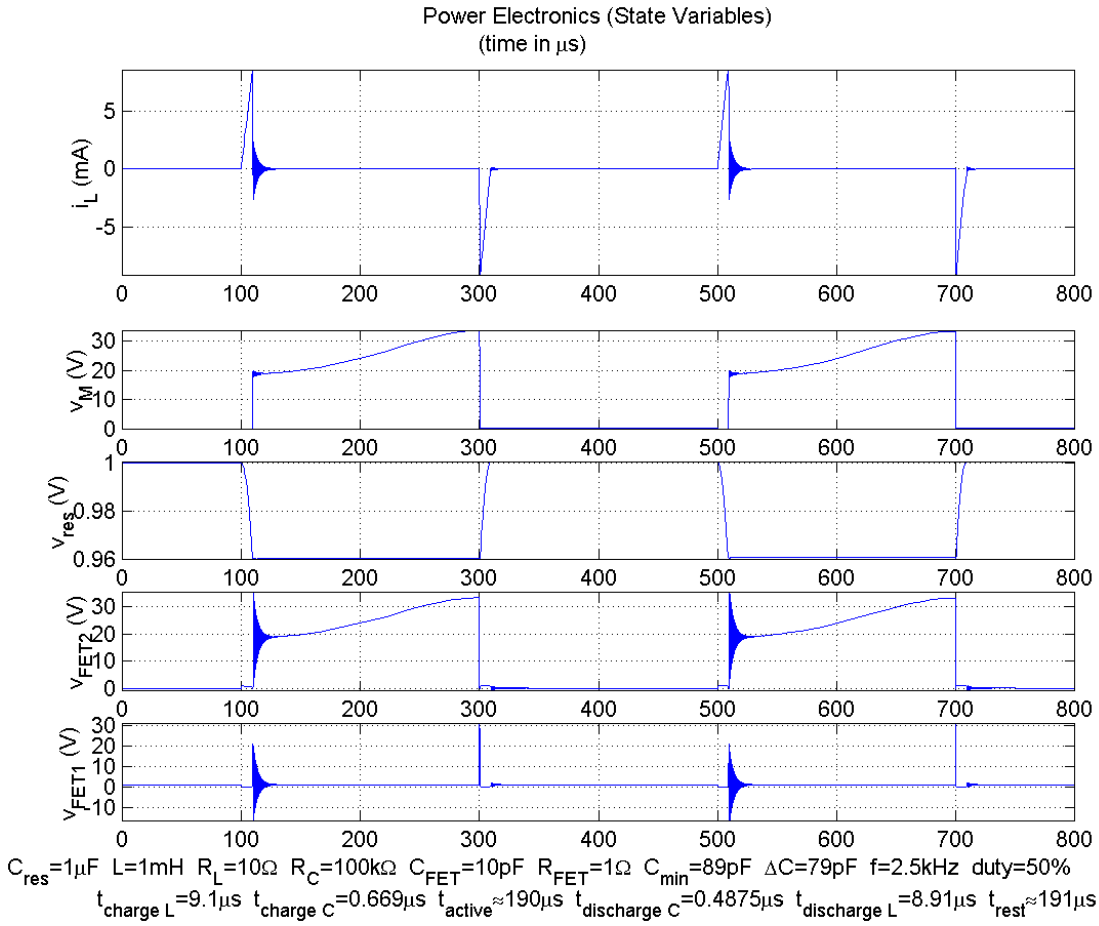

Figure 3-17: State variables of the power electronics circuit.

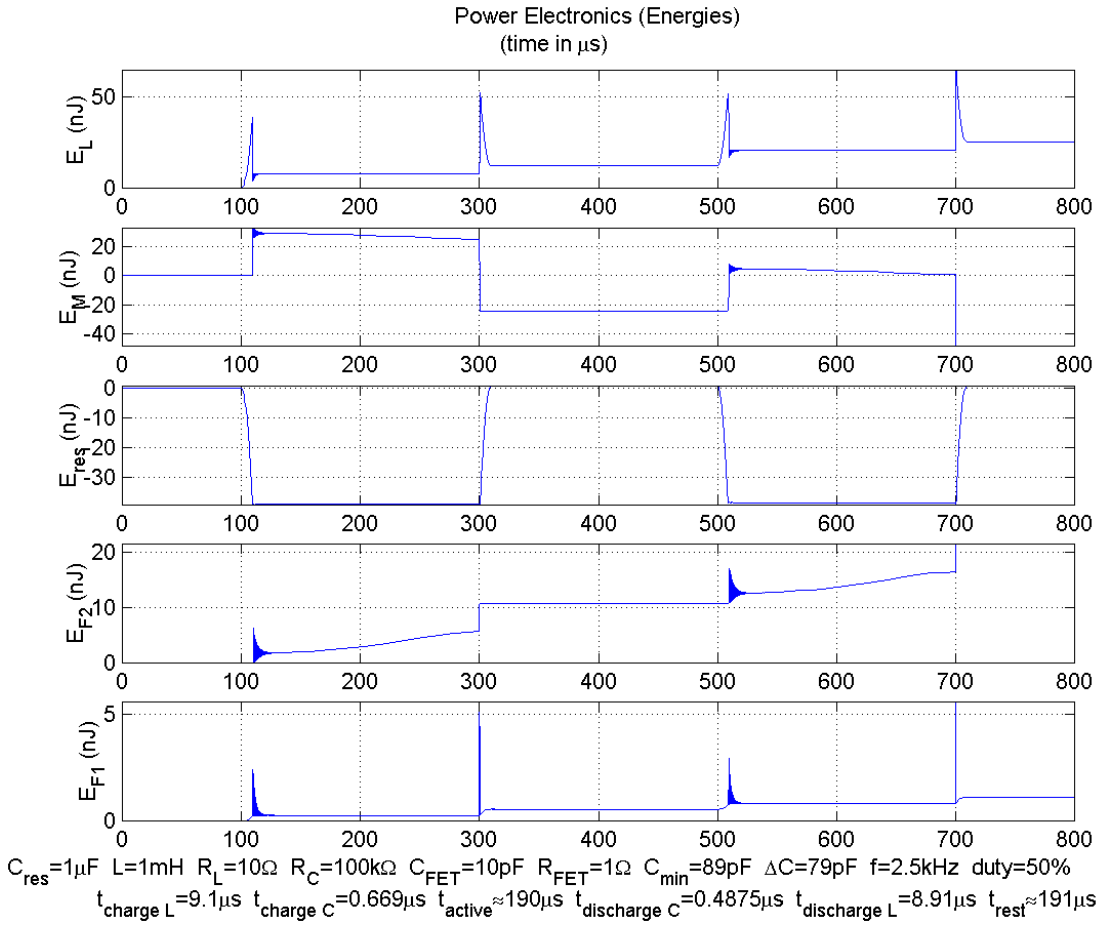

Figure 3-18: Energy analysis of the power electronics circuit.

the variable capacitor in the simulation before discharging, 33.5 V is in accordance with Equation 2.1.

Figure 3-18 shows the energy level of all the elements of the circuit. After one cycle, the capacitor has provided 24.4 nJ, in accordance with Equation 2.3. The energy dissipated in the inductor is 12.6 nJ. The energy dissipated in the bottom MOSFET is 0.5 nJ, but the energy dissipated in the top MOSFET is 10.7 nJ. The net energy gained by the reservoir is 0.5 nJ. This energy represents a power output of 1.3 μW at 2.5 kHz. The electrical efficiency, defined as the energy gained by the reservoir over the electric energy converted by the variable capacitor is 2%.

Note that almost all of the energy provided by the variable capacitor was lost in the inductor and the top MOSFET. This stresses the importance of choosing better elements or using a different strategy, such as zero-voltage-switching (ZVS) to minimize these losses.

Furthermore, after the initial charge is delivered to the inductor, all the timing parameters are set strictly by the component values of the power electronics. Failure to switch at the precise time decreases even more the efficiency of the energy transport through the power electronics.

3.7 Summary

The circuit topology proposed in this chapter implements the charge-constrained cycle proposed in Chapter 2. The experimental setup proves that energy was extracted from the vibration source, even though the power electronics circuit is not efficient enough to translate this energy gain on the variable capacitor to an energy gain in the reservoir. Nevertheless, the close match between the model and the experiment give confidence that the model captures the behavior of the real circuit.

The simulation also shows the sources of loss in the power electronics of the test circuit. A redesigned version of the same circuit is proposed which addresses these issues. Also, a larger capacitance change is assumed, which will be justified in Chapter 6. The simulation of the improved system shows a net gain in energy of 0.5 nJ, which corresponds to a power

output of 1.3 μW at 2.5 kHz. The energy converted by the variable capacitor is 24.4 nJ, which implies an efficiency of 2%.

Note that the simulation results also show that the vast majority of the energy obtained from the conversion cycle is lost in the power electronics, and that the precise timing of the MOSFET's switching is essential to obtain the maximum efficiency possible from the power electronics.

Chapter 4

Electromechanical Dynamics

The simulation of the power electronics circuit proposed in Section 3.5 indicates that the charge-constrained cycle proposed in Section 2.6 generates enough power to overcome the losses in the power electronics. Furthermore, both the simulation and Equation 2.3 show that 24 nJ can be harvested by the example energy conversion cycle. The extraction of this power from the resonator acts as a damper. This damper will impose constraints on the mass of the resonator and its travel so that a given vibration source can transfer enough energy into the resonator to overcome the losses of the damper.

This chapter develops a generalized linear model of a resonator driven by a vibration position source where two dampers represent the electrostatic energy conversion and the mechanical losses. The result indicates that the resonator couples to the acceleration of the source, and that the power output is proportional to the resonator mass and its travel along with the acceleration. Furthermore, the analysis shows constraints in terms of the Q of the system for the validity of this analysis.

4.1 Model Analysis

The model shown in Figure 4-1 represents a generalized energy harvester and is described by

$$M\frac{d^2x}{dt^2} + b_m\frac{dx}{dt} + b_e\frac{dx}{dt} + Kx = -M\frac{d^2y}{dt^2} \tag{4.1}$$

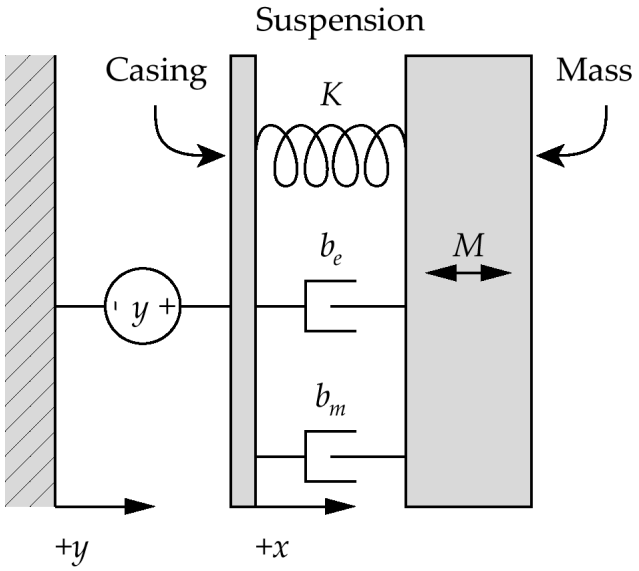

Figure 4-1: Electromechanical model of the generalized energy harvester.

where x is the distance between the moving mass and its casing, M is the mass of the moving block, b_m is mechanical damping, b_e is electrostatic damping, K is spring coefficient of the suspension, and y is the position of the source. The source is assumed to be sinusoidal with complex amplitude $\hat{Y}$ and frequency ω. This assumption will be justified in the next chapter.

Transient solutions of the system will be ignored in this analysis. The system will be assumed to operate in sinusoidal steady state. With the system operating in sinusoidal steady state, Equation 4.1 reduces to

$$-M\omega^2\hat{X} + j\omega(b_m + b_e)\hat{X} + K\hat{X} = -M\omega^2\hat{Y} \tag{4.2}$$

where $\hat{X}$ is the complex amplitude of x. Define $X = |\hat{X}|$ and $Y = |\hat{Y}|$. Solving for X,

$$X = \frac{M\omega^2 Y}{\sqrt{(K - M\omega^2)^2 + (b_e + b_m)^2\omega^2}} \tag{4.3}$$

The power output is the average power converted by the electrostatic damper,

$$P_e = \frac{1}{2} b_e \omega^2 X^2 \tag{4.4}$$

Substitution of Equation 4.3 into Equation 4.4 yields

$$P_e = \frac{1}{2} b_e \frac{M^2 \omega^6 Y^2}{(K - M\omega^2)^2 + (b_e + b_m)^2 \omega^2} \tag{4.5}$$

This expression for power output is maximized if the resonant frequency of the spring mass system $\sqrt{K/M}$ matches the driving frequency ω. Under this assumption,

$$P_e = \frac{1}{2} \frac{b_e}{(b_e + b_m)^2} M^2 \omega^4 Y^2 \tag{4.6}$$

and

$$X = \frac{M\omega Y}{b_e + b_m} \tag{4.7}$$

Substitution of Equation 4.7 into Equation 4.6 yields

$$P_e = \frac{1}{2} \frac{b_e}{b_e + b_m} M \omega^3 Y X \tag{4.8}$$

Note that $\omega^2 Y$ is the acceleration magnitude of the source. Defining $a = \omega^2 Y$,

$$P_e = \frac{1}{2} \frac{b_e}{b_e + b_m} M \omega a X \tag{4.9}$$

The power dissipated by the mechanical losses is

$$P_m = \frac{1}{2} b_m \omega^2 X^2 \tag{4.10}$$

Following an argument identical to that used to analyze the electrostatic power P_e, Equation 4.10 yields

$$P_m = \frac{1}{2} \frac{b_m}{b_e + b_m} M \omega a X \tag{4.11}$$

The power input must equal the total power converted and dissipated by the system. Thus,

$$P_{in} = P_e + P_m = \frac{1}{2} M \omega a X \tag{4.12}$$

The energy provided by the source in one cycle is $E_{in} = P_{in}/f$, where $1/f = 2\pi/\omega$, and is given by

$$E_{in} = E_e + E_m = 2\pi\frac{1}{2}MaX \tag{4.13}$$

The electrostatic energy conversion and mechanical loss of the system can be assumed to behave linearly because the details of the electrostatic force and the mechanical damping are irrelevant to the analysis as long as the energy converted and lost in the system is much smaller than the energy stored in the spring-mass resonator. This requirement can be expressed in the terms of the quality factor Q of the system; Q is defined as

$$Q = \sqrt{KM}/(b_e + b_m) \tag{4.14}$$

At resonance,

$$Q = \frac{M\omega}{b_e + b_m} \tag{4.15}$$

Multiplying Equation 4.15 by $\frac{\frac{1}{2}\omega X^2}{\frac{1}{2}\omega X^2}$,

$$Q = \frac{\frac{1}{2}M\omega^2X^2}{\frac{1}{2}(b_e + b_m)X^2\omega} = 2\pi\frac{\text{Energy stored}}{\text{Energy lost}} >> 1 \tag{4.16}$$

for the analysis to hold, since $\frac{1}{2}M\omega^2X^2$ is the energy stored in the spring-mass resonator, and $\frac{1}{2}(b_e + b_m)\omega^2X^2\frac{2\pi}{\omega}$ is the energy converted and lost per cycle. Furthermore, since the energy converted and lost per cycle equals the energy supplied by the source, Equation 4.16 may be written as

$$Q = 2\pi\frac{\frac{1}{2}M\omega^2X^2}{E_e + E_m} = \frac{\frac{1}{2}M\omega^2X^2}{\frac{1}{2}MaX} = \frac{\omega^2X}{a} >> 1 \Rightarrow X >> Y \tag{4.17}$$

Note that the last result relates the acceleration of the mass ω^2X to the acceleration of the external source, and the displacement of the mass to the displacement of the source. Again, as long as Equation 4.17 holds, the analysis above is accurate independent of the details of the physics behind b_e.

4.2 Summary

Equations 4.12 and 4.13 relate the energy requirements of an electrostatic harvester to the mass and travel of the system and the acceleration of the vibration source. Chapter 2 proposed an energy conversion cycle which extracts 23.4 nJ. Chapter 3 develops power electronics that are able to produce 1.3 μW at 2.5 kHz from this cycle. Next, Chapter 5 will find that acceleration magnitudes of 0.02 g_E, where $g_E = 9.81$ m/s^2 is the acceleration of gravity on Earth, can be assumed, as well as justify our assumption of a sinusoidal vibration source operating at 2.5 kHz. These numbers constrain the product MX using Equations 4.12 and 4.13, assuming the mechanical power losses may be neglected. A choice of $M = 195\ mg$ and $X = 200\ \mu$m fulfills this constraint. This choice of X and M will be the basis of a proposed variable capacitor in Chapter 6.

Once X has been chosen, the requirement imposed by Equation 4.17 can be checked. Assuming $X = 200\ \mu$m, $a = 0.02\ g_E$ and $f = 2.5\ kHz$, the resulting Q is 250,000. This Q clearly satisfies $Q >> 1$. However, note that the choice of M and X neglects any mechanical losses. However, mechanical Q's of similar devices operating in vacuum may be as low as 10,000. In this case, these losses may not neglected, and X and M must be chosen such that the energy input E_{in} is sufficient to cover both losses, as dictated by Equation 4.13. For the purposes of this thesis, the mechanical losses are ignored. Note that the requirement of a high mechanical Q dictates that a successful energy harvester must be operated in vacuum.

In conclusion, it is worthwhile to reiterate what is learned from Equation 4.12. Assuming that $E_e >> E_m$, $P_e \approx \frac{1}{2} M\omega a X$. Therefore, for a given M and X, as limited by fabrication and structural constraints, the converted power will be maximized by maximizing the product ωa. This product will become a useful metric in Chapter 5 with which to compare the available spectrum peaks. This observation is independent of the exact means of mechanical to electric energy conversion.

Chapter 5

Ambient Vibration Sources

The design of a vibration energy harvester depends on the nature of the available vibration sources. These vibration sources must be explored in order to generate a model for them that will serve as a foundation for the design of a harvester. The goal of this chapter is to choose a type of vibration to use as a source, and generate a reasonable model which may be incorporated in subsequent analysis.

The character of vibration sources varies depending on the source. Vibration energy from biological sources tends to be in the range of frequencies below a few hundred hertz, have very small accelerations and not be very stiff. Mechanical vibration frequencies are usually higher. Yet, these frequencies are still related to the dimensions of the vibrating device. Fluid flow vibrations are usually caused by turbulence, and exhibit a wide frequency range. Rotating machinery vibrations are commonly caused by bearing components, gear teeth, reciprocating elements, turbine blades and the like, and have a discrete spectrum based on the fundamental frequency of rotation [42].

Among all these options, rotating machinery appears an attractive choice for energy harvester design. Their vibration levels are usually among the highest and their frequency spectrum is predictable and repeatable. Much work has been done in the description of their spectra as a means of diagnosing the condition of bearings, shaft alignment, and other common problems with rotating machinery [42]. The relative concentration of energy in high-frequency peaks enables the design of high-Q harvesters which resonate at those peaks.

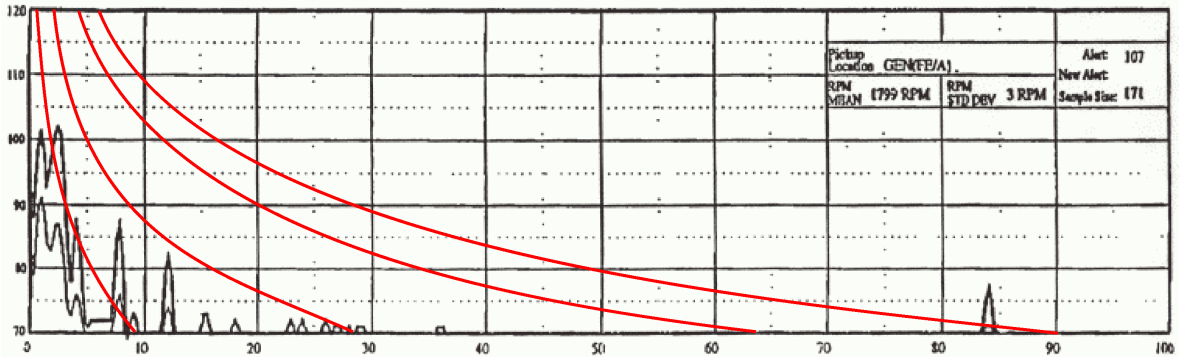

Figure 5-1: Vibration spectrum of a gas turbine generator that rotates at 1,800 rpm. The vibration spectrum is measured in RMS velocity (in dB above 10^{-2} μm/s) versus frequency in harmonics of 1,800 rpm (30Hz). The smooth solid lines are constant frequency-acceleration products. The uppermost line has a constant frequency-acceleration product equal to 2π(2,520 Hz)(0.082 g_E), where g_E = 9.81 m/s^2 is the acceleration of gravity. The second, third and fourth lines have products equal to half, a tenth, and a hundredth of the first line, respectively. Courtesy of Charles Stark Draper Laboratories.

Chapter 4 assumed a sinusoidal vibration source, consistent with the assumption of coupling to a narrow vibration peak. Furthermore, the model indicates that a resonating harvester couples to the acceleration of these peaks. Thus, a reasonable model of the vibration source of a rotating machine is an acceleration source operating at a single frequency. Since these sources are also very stiff, the impedance of the source may be neglected.

Once the form of the model is assumed to be a sinusoidal source, analysis of vibration spectra will indicate what range of frequencies can be expected to have the largest accelerations. The peak which produces the highest power will be chosen. This is the peak with the greatest acceleration-frequency product.

5.1 Vibration Spectra

Figure 5-1 shows the vibration spectrum of a gas turbine generator that rotates at 1,800 rpm. The vibration spectrum is measured in RMS velocity (in dB above 10^{-2} μm/s) versus frequency in harmonics of 1,800 rpm (30Hz). Note that the vibration energy is present at discrete frequencies. The maximum acceleration is found at 2520Hz (84th harmonic), where the measured velocity is 0.051 mm/s; note that the vertical axis of the figure is velocity. The displacement at this peak is 3.2 μm. The acceleration at this peak is 0.81 m/s^2, or 0.08 g_E,

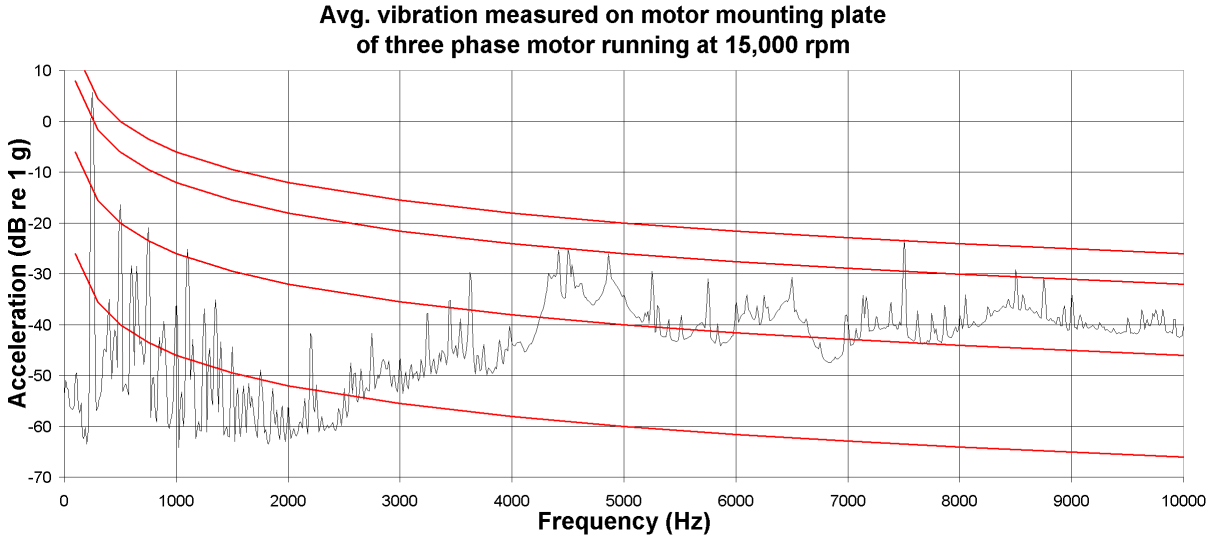

Figure 5-2: Vibration spectrum of a three-phase motor running at 15,000 rpm. This represents a fundamental frequency of 250 Hz. Acceleration of -40 dB is 0.01 g_E in the graph above; -20 dB is 0.1 g_E. The smooth solid lines are constant frequency-acceleration products. The uppermost line has a constant frequency-acceleration product equal to 2π(5 kHz)(0.1 g_E). The second, third and fourth lines have products equal to half, a tenth, and a hundredth of the first line, respectively. Courtesy of RH Lyon Corporation.

where $g_E = 9.81$ m/s^2 is the acceleration of gravity. Superimposed onto Figure 5-1 are curves of constant acceleration times frequency. In Chapter 4, it was found that this product is proportional to converted power for a given mass and displacement. These curves are provided to indicate the relative power available from the 84th harmonic and other spectral peaks.

As a second example, Figure 5-2 shows the vibration spectrum of a three-phase motor. Again, vibration energy is present at discrete frequencies and extends to high frequencies. Note the three peaks above 0.03 g_E (-30dB) between 4 kHz and 5 kHz. An acceleration magnitude of 0.03 g_E at 4.5 kHz translates into a velocity 0.01 mm/s and a displacement of 0.4 nm. Again, as in Figure 5-1, curves of constant acceleration-frequency product are provided to facilitate a comparison of vibration peaks.

Figure 5-3 is a maintenance chart for rotating machinery, and provides critical levels of vibration as a function of frequency. Note that vibration levels as high as 0.2 g_E are still noted as acceptable, which implies that rotating machines routinely have peaks at that level. Note also that, although the graph ends at 1 kHz, the acceleration line is still constant. Peaks at higher frequencies are usually present.

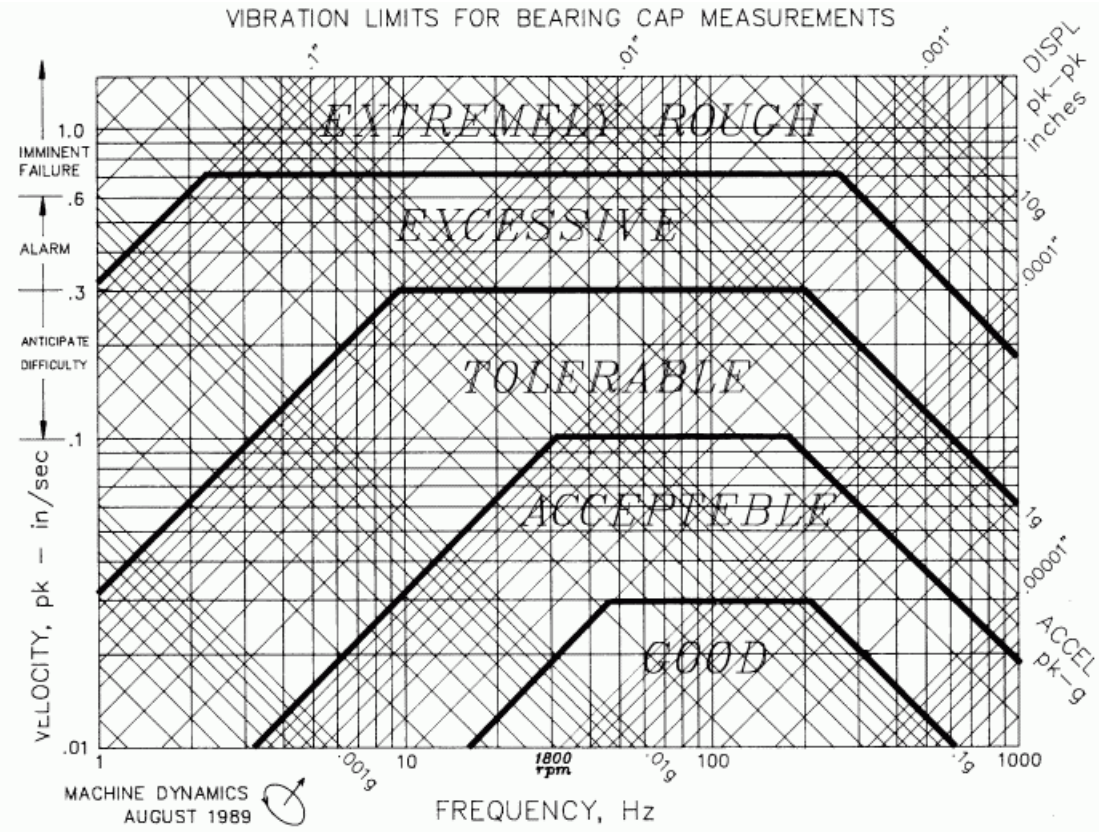

Figure 7.4 Vibration severity judgment chart.

Figure 5-3: Vibration magnitude as a function of frequency [42].

Although the magnitudes and location of peaks differ between the examples shown in Figures 5-1 and 5-2, they both show spectra with high peaks up to a few kilohertz. Furthermore, they are consistent with Figure 5-3 in having acceleration peaks between 1% to 10% of g_E at these frequencies. These similarities allow modeling these sources as sinuosidal accelerations with and expected magnitude within a window of frequencies.

5.2 Resonator Constraints

As a rule of thumb, mechanical devices whose structural resonances are above 1 kHz are easier to handle during fabrication. Furthermore, the next section shows that the peaks with produce the highest amount of energy are located at higher frequencies. Thus, the resonant frequency of the spring-mass system, as well as other structural resonances of the variable capacitor will be kept above 1 kHz to ensure the mechanical robustness of the variable capacitor during handling. This is to avoid breakage. Mechanical resonances below this frequency have large displacements. These displacements may result in high stress points in the structure, leading to breakage. Furthermore, low frequency resonances can easily be excited. Dropping or hitting a device can easily provide the sufficient energy to excite a low frequency resonance to the point where the structure breaks. Note, however, that this is just a convenience rule, given that vibration peaks below 1 kHz will have less power than those above. Although careful design and fabrication can produce devices who resonate at frequencies below 1 kHz, it appears from the discussion of Section 5.1 that this is not necessary given typical vibration spectra.

The robustness limit imposes a constraint on how low a MEMS device can be made to resonate, if it is to safely survive its fabrication process. The resonant frequency at which the harvesting occurs should be above 1 kHz, in order to insure the mechanical reliability of a resonator during normal fabrication. If a particular application requires a resonator below 1 kHz, the constraints on the mechanical structure increase dramatically. The suspension, in particular, must be designed to handle stresses much larger than those found in normal operation. These extra requirements can have a detrimental effect in the overall performance of the energy harvester.

5.3 Power Constraints

The results of Chapter 4 indicate that the energy output of an energy harvester is proportional to the acceleration of the source, assuming the displacement is constrained to a reasonable and achievable maximum. Power output is equal to this energy times the frequency at which the device operates. Therefore, the power output is linearly proportional to both frequency and acceleration magnitude. Thus, the product of the magnitude and frequency of the acceleration must be maximized when selecting a source vibration frequency peak in order to maximize power output.

The vibration data shows that peaks above 5 kHz decay rapidly, and while some peaks around 1 kHz might be higher, the product of magnitude and frequency is higher at larger frequencies until the decay starts. The vibration data also indicates that these peaks vary among the different types of machines, and even among similar or identical machines depending on the condition of their bearings, shaft alignment or mechanical structure. If the energy harvester is custom-designed for a particular machine, it might easier to identify the ideal peak at which to operate. However, if the energy harvester is designed to operate with different machines, choosing the right peak can be more challenging, since the harvester may produce a lot of power in a particular machine and little or none in the next. Different solutions must be devised to address these issues, such as creating low-Q resonators (within the constraints explained in Chapter 4), employing different resonators with different resonances in parallel, or adjusting the resonant frequency of the mechanical device during operation to choose the optimal operating point. This last option can be done with electrostatic tuning of the spring, although such functionality will bring an added energy tax on the system.

5.4 Summary

Mechanical robustness during fabrication of the variable capacitor imposes a minimal frequency constraint on useful vibration energy of about 1 kHz, although this is not a strict rule. The data from rotating machinery indicates that peaks with acceleration magnitudes as high as 2% of g_E exist until about 5 kHz. These two limits define a range of 1-5 kHz

where vibration harvesters for rotating machinery should be designed to operate. Vibration levels in this range can be expected to have acceleration magnitudes of 2% of g_E in discrete peaks. Within this window, maximization of power output indicates that the peak with the highest acceleration-frequency product should be chosen. However, the location of this peak is unknown a priori. Nevertheless, such a peak is expected to exist. Thus, the design in this thesis assumes the existence of a stiff acceleration peak within the range of 1-5 kHz having a magnitude of 2% of g_E. In particular, this peak will be modeled as a sinusoidal acceleration source at 2.5 kHz, which is in accordance with the data from the turbine generator in Figure 5-1, and a magnitude 2% of g_E, in accordance with the rest of the data. Note, however, that the acceleration magnitude in the turbine example is 8% of a g_E, four times larger). The acceleration source is also assumed to have no impedance, in accordance with the assumption of a stiff source. This is a reasonable assumption given the small mass of the harvester in comparison with the machine, and given that a rigid package and mounting for the harvester can be designed.

Chapter 6

Structural Design

This chapter designs a variable capacitor with the mass of 195 mg and the travel of 200 μm required by Chapter 4 to couple to an external vibration source of acceleration 0.02 g_E, where $g_E = 9.81$ m/s^2 is the acceleration of gravity, at a frequency of 2.5 kHz, as assumed in Chapter 5. Furthermore, this structure must provide the C_{min} of 89 pF and C_{max} of 168 pF assumed in Chapter 3 to generate the 24 nJ required by charge-constrained cycle of Chapter 2. If different numbers are desired, the design process will be identical.

The devices proposed in this chapter are created using MEMS fabrication technology. The fabrication process to create these devices will be discussed in Chapter 7. Since a specific fabrication technology is assumed to create these devices, the mass requirement must be achieved using materials used in this technology. The shuttle mass can be reasonably assumed to be made out of silicon, although metal electroplating can be used to increase mass if desired. The shuttle mass is assumed to be a 1 cm square in a standard wafer of 500 μm thickness. This square has a mass of 116 mg, given that the density of silicon is 2300kg/m^3. However, recall that Chapter 4 required 195 mg of mass in order to require a 200 μm travel. If the mass is decreased, the required travel must increase accordingly. In order to reach 195 mg of mass, a layer of gold, which has a density of 19,300 kg/m^3, may be electroplated on top of the 1 cm square mass. The necessary thickness of the gold is 41 μm in order to reach 195 mg.

The power electronics constrain the minimal energy necessary from the energy conversion cycle in order to produce a net gain in energy at the reservoir. In turn, the energy required by

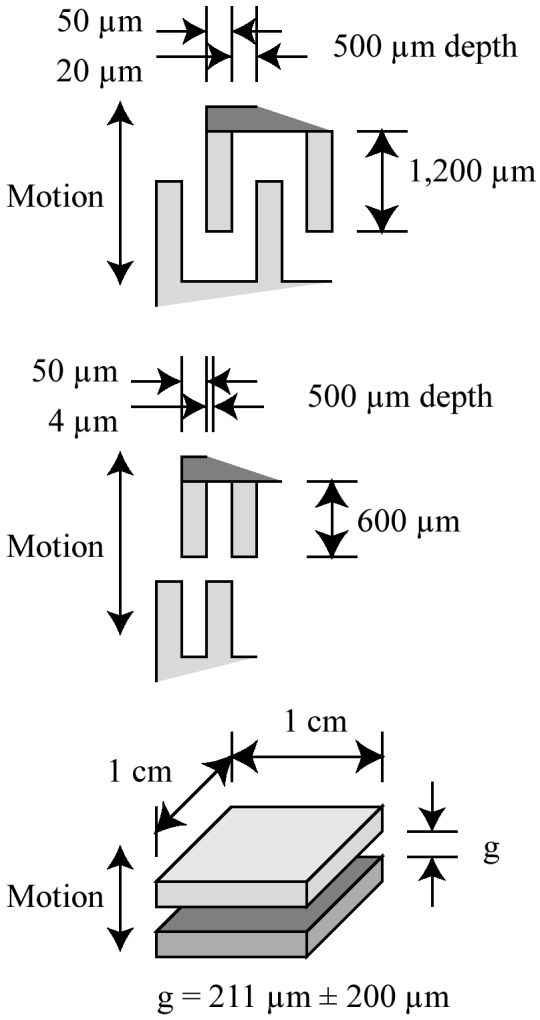

Figure 6-1: Capacitor structures considered. The first two are constant-gap converters and the last is a variable-gap converter. All structures are shown as fabricated.

the conversion cycle constrains the C_{max} and C_{min} of the structure. Note that the variable capacitor need only provide the change in capacitance $\Delta C = C_{max} - C_{min}$. Additional capacitance can easily be added with an external constant capacitor in parallel with the variable capacitor.

Variable capacitors can be divided according to the fundamental mechanism by which they create the variation in capacitance. Figure 6-1 shows the capacitors considered in this thesis. While these designs are not exhaustive, they are intended to represent the two fundamental mechanisms, and their analysis can be extended to other structures. The first type, constant-gap capacitors, rely on capacitor plates that move laterally while keeping the

gap between them constant. The overlap of the plates in these capacitors varies. The second type, variable-gap capacitors, rely on plates that move away and toward each other, changing the distance between them. The overlap area of the plates in these capacitors is constant. Appendix A derives the force-voltage relationship for each capacitor type. However, the detailed dependence on motion of the forces may be ignored if the electrostatic energy they extract is small compared to the stored mechanical energy, as justified in Chapter 4.

While both constant-gap structures shown in Figure 6-1 operate in an identical fashion, the constraints imposed by the fabrication technology are much different. The top-most capacitor has a gap that is constrained by the minimum feature size of the etch used to fabricate it. The gap of the middle capacitor is limited by the characteristic of the etch used, specifically the straightness of the wall. This last limitation allows for the creation of much smaller gaps than the limitation imposed by the minimum feature size of the etch.

6.1 Variable-Gap Converter

The capacitance $C(t)$ of a variable-gap capacitor is

$$C_{\text{variable gap}}(t) = \epsilon_0 \frac{A}{g(t)} \tag{6.1}$$

where ϵ_0 is the permittivity of free space, A is the overlapping area of the plates, and $g(t)$ is the time-varying gap. The time varying-gap can be expressed as

$$g(t) = g + X\sin(\omega t) \tag{6.2}$$

where g is the nominal gap when the shuttle mass is at rest, X is the travel amplitude of the shuttle mass and ω is the driving frequency of the acceleration source. The motion of the shuttle mass can be assumed to be a sinusoid under the requirement that the energy extracted by the electrostatic force is much less than the energy stored in the mass-spring resonator, as discussed in Chapter 4. The resulting expression for capacitance is

$$C_{\text{variable gap}}(t) = \epsilon_0 \frac{A}{g + X\sin(\omega t)} \tag{6.3}$$

In order to achieve large capacitance changes in a variable gap converter, the critical design parameter is the minimum gap $g-X$ necessary to create C_{max}. The capacitance is inversely proportional to this gap; therefore, the minimum capacitance is quickly reached and is typically a very small value. The majority of the change in capacitance occurs only when the gap is very small since the capacitance as a function of time is proportional to $\frac{1}{1+X/g\sin(\omega t)}$. This imposes critical timing constraints on the power electronics in order to charge the capacitor at the correct moment. In order to create a large capacitance change, the minimum gap must be small. This implies that the shuttle mass must travel almost all the nominal gap. Thus, $X \approx g$. With this assumption, the change in capacitance of a variable-gap capacitor is

$$\Delta C_{\text{variable gap}} = \epsilon_0 \frac{A}{g-X} - \epsilon_0 \frac{A}{g+X} \approx \epsilon_0 \frac{A}{g-X} \tag{6.4}$$

Figure 6-2 shows a plan view of a proposed variable-gap energy harvester. The moving silicon/metal mass moves in and out of the page. The bottom of this mass is the moving plate of the variable capacitor. Below the mass is a layer of metal that acts as the fixed plate of the variable capacitor. A side view of the structure is shown in Figure 7-2. If the gap is brought down to 11 μm, Equation 6.4 dictates a change of capacitance of 80 pF. Assuming a travel amplitude of 200 μm, proposed in Chapter 4, the nominal gap g must be 211 μm, and $X \approx g$ as expected. Recall that the power electronics proposed in Chapter 3 require a capacitance change of 168 pF $-$ 89 pF $=$ 79 pF. Thus, this device can provide the necessary change in capacitance by adding a parallel capacitor of 88 pF. Some of this capacitance will surely come in the form of parasitic capacitors.

The large area surrounding the mass can be used to create a membrane spring as a suspension. Assuming a 2 mm spring length, and using the whole perimeter of a 1 cm square as the width, as shown in Figure 6-2, a silicon spring with a Young's Modulus of 155 GPa needs to be 40 μm thick, which is easily constructed [43]. The maximum stress on this membrane spring occurs when the displacement of the mass is 200 μm. As a rule of thumb, the maximum stress in the beam must be kept below 1% to avoid fractures. The stress on the beam is 0.3% of the Young's Modulus of silicon, which satisfies this rule.

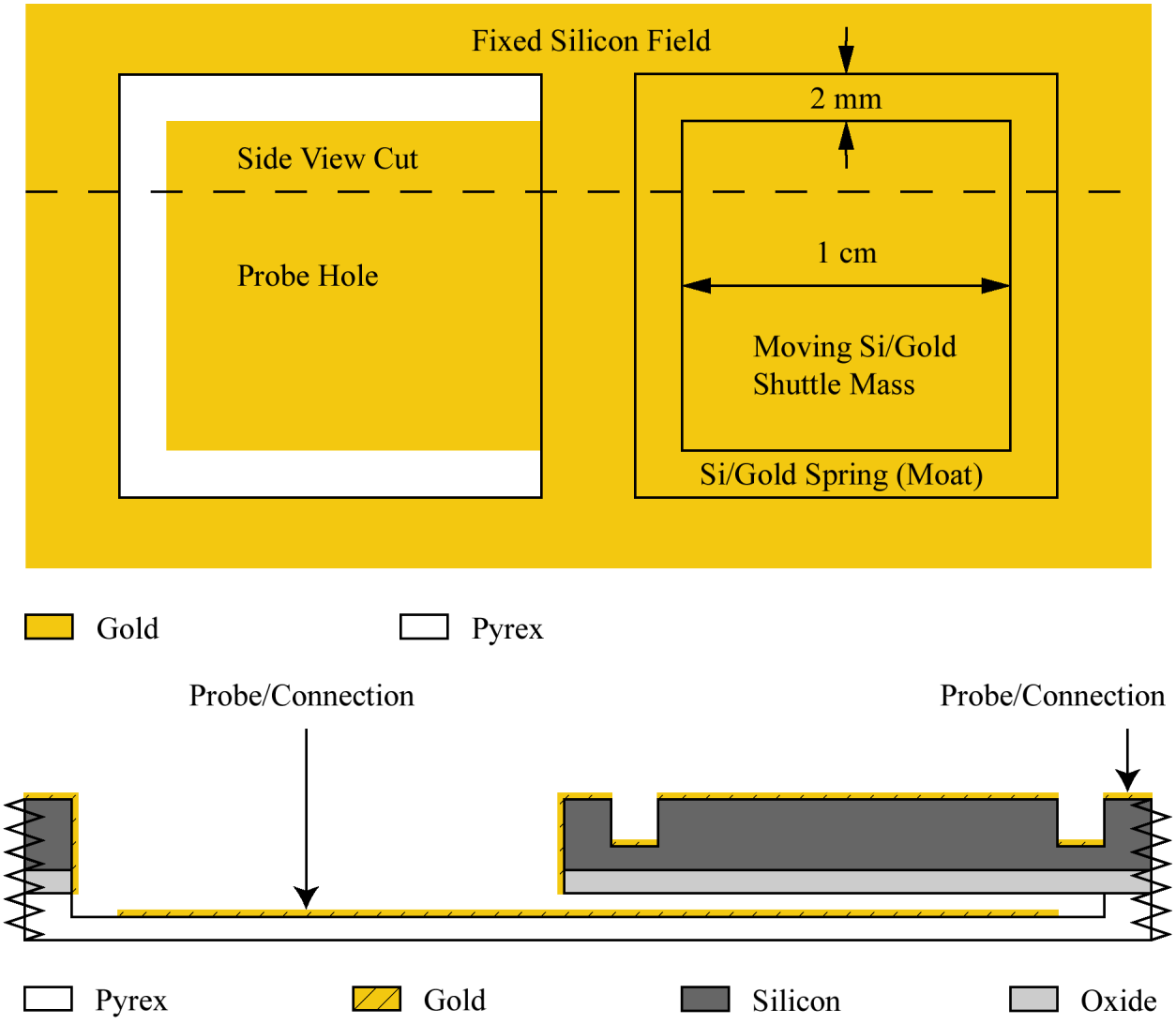

Figure 6-2: Plan view of a variable-gap energy harvester. The shuttle mass is the 1 cm square on the right. The shuttle mass moves in and out of the page. The 2 mm-wide moat around it acts as a membrane spring. The metal in the probe hole on the left is below the moving silicon/metal mass and acts as the fixed terminal of a variable-gap capacitor. A side view of this structure is shown in Figure 7-2 and repeated here for convenience.

Appendix E contains a derivation of the spring constant and maximum stress of a spring beam.

6.2 Constant-Gap Converter

The advantage of a constant-gap capacitor is constant force, which minimizes timing and stability requirements, at the cost of capacitance change. The capacitance of a constant-gap capacitor is

$$C_{\text{constant gap}}(t) = \epsilon_0 \frac{T X_o(t)}{g} \tag{6.5}$$

where ϵ_0 is the permittivity of free space, g is the constant gap between the plates, T is the non-changing overlap distance of the plates, and $X_o(t)$ is the time-varying overlap distance of the plates. The time varying-overlap can be expressed as $X_o(t) = X(1+\sin(\omega t))$, where X is the travel amplitude of the shuttle mass and ω is the driving frequency of the acceleration source. Note that the overlap goes from zero to $2X$, and when the comb is stationary, the fingers overlap half of the maximum distance. As before, the motion of the shuttle mass can be assumed to be a sinusoid under the condition that the energy extracted by the electrostatic force is much less than the energy stored in the mass-spring resonator, as discussed in Chapter 4. The resulting expression for capacitance is

$$C_{\text{constant gap}}(t) = \epsilon_0 \frac{T}{g} X(1 + sin(\omega t)) \tag{6.6}$$

The change in capacitance is

$$\Delta C_{\text{constant gap}} = \epsilon_0 \frac{T}{g} 2X \tag{6.7}$$

Note that the capacitance change is proportional to the travel X and the depth-to-gap ratio T/g. In order to obtain a reasonable capacitance change, the requirements on travel and aspect ratio are hard to achieve. For example, a change in capacitance of 79 pF requires an aspect ratio of 113:1 and total travel of 8 cm. Both propositions seem hard to create with current MEMS fabrication technology. Thus, instead of having a single pair of traveling

plates, multiple plates connected can travel shorter distances. This is the basic idea behind a comb-drive.

A comb-drive, shown in Figure 6-3, consists of several fingers which travel alongside each other. In this case, the requirements on aspect ratio and travel are reduced by multiplying the number plates sliding past each other. For a comb-drive, the total change in capacitance is

$$\Delta C_{\text{comb drive}} = \epsilon_0 \frac{T}{g} 2X \frac{L}{w+g} \tag{6.8}$$

where ϵ_0 is the permittivity of free space, g is the constant gap between the plates, T is the non-changing overlap distance of the plates, and X is the travel amplitude of the shuttle mass, w is the width of each finger and L is the total length of the comb-drive, shown as 1 cm in Figure 6-3.

The fingers gliding past each other experience a balanced electrostatic pull sideways. However, this equilibrium is unstable. If a finger starts to bend sideways, the electrostatic force to the side to which the finger is bending will be stronger than the electrostatic force to the other side. This effect is known as electrostatic instability. This effect requires a minimal width of the finger to avoid bending. Furthermore, the mechanical resonance of each must be kept, as a rule of thumb, about ten times higher than the frequency of the source vibration to avoid collision of the fingers.

The aspect ratio of the fingers is constrained by the technology used to create them. Using deep reactive ion etching (DRIE), the gap between the fingers can be expected to be around 20 μm for a through-etch of a 500 μm-thick silicon wafer, for an aspect ratio of 25:1 [7]. In order to compare this capacitor structure to the variable gap structure proposed in the previous section the length of the comb L is assumed to be 1 cm. Note that the beams have a length of approximately 0.3 cm and that each beam only has to be displaced half of the total travel distance. Using the rule of thumb that the stress must be less than 1% of Young's Modulus and 50 μm-thick beams, results in a maximum theoretical travel X of 1,200 μm. Assuming 50 μm-thick fingers the total change of capacitance is

$$\epsilon_0 \frac{500\ \mu\text{m}}{20\ \mu\text{m}} 2 \cdot 1,200\ \mu\text{m} \frac{1\ \text{cm}}{50\ \mu\text{m} + 20\ \mu\text{m}} = 76\ \text{pF} \tag{6.9}$$

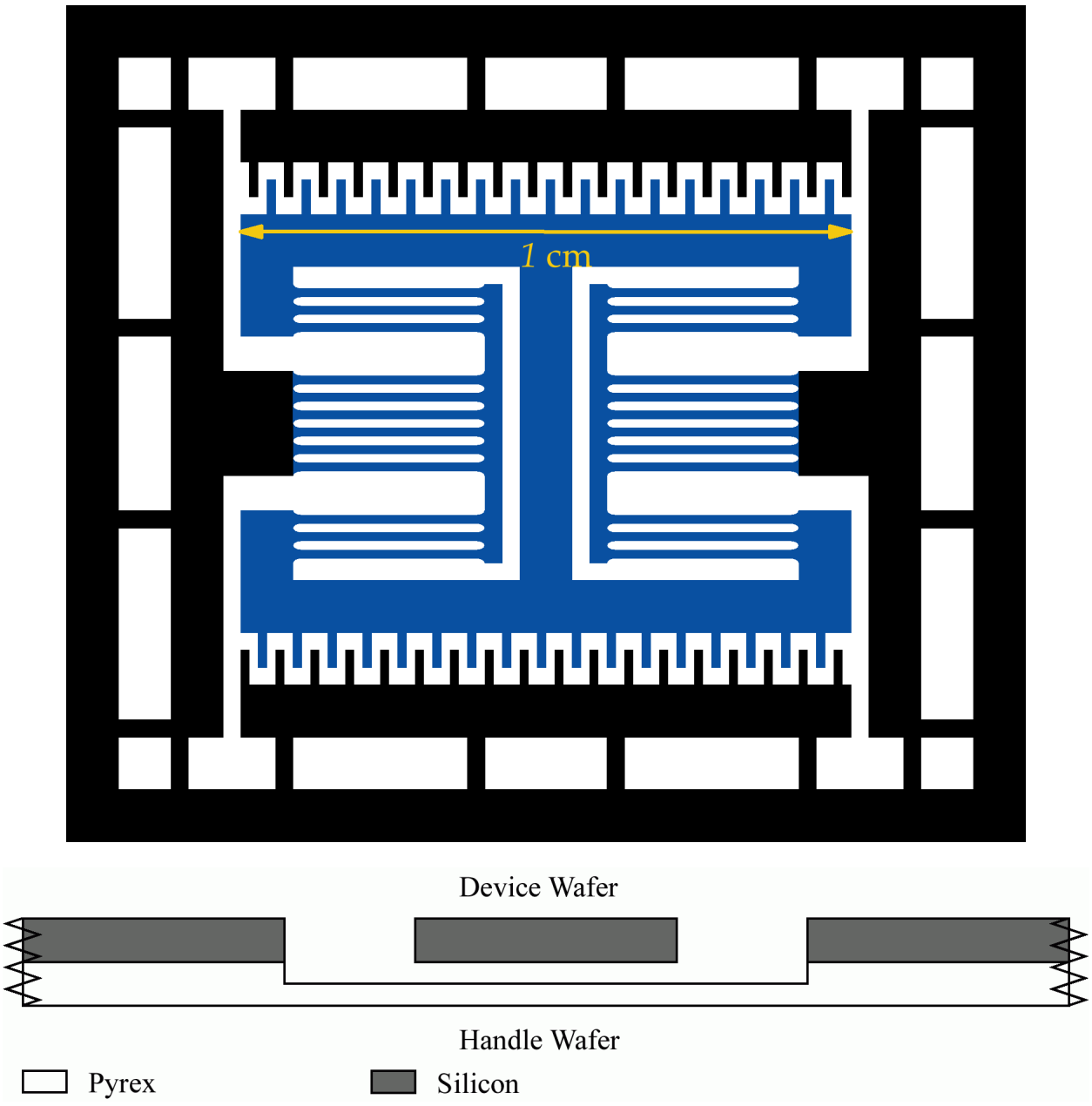

Figure 6-3: Plan view of a variable-gap energy harvester with overlapping fingers. The shuttle mass is the blue I-shape in the center. The shuttle mass moves up and down. The black area is the non-moving anchors and fingers. The horizontal beams form the suspension. A side view of this structure is shown in Figure 7-1 and repeated here for convenience.

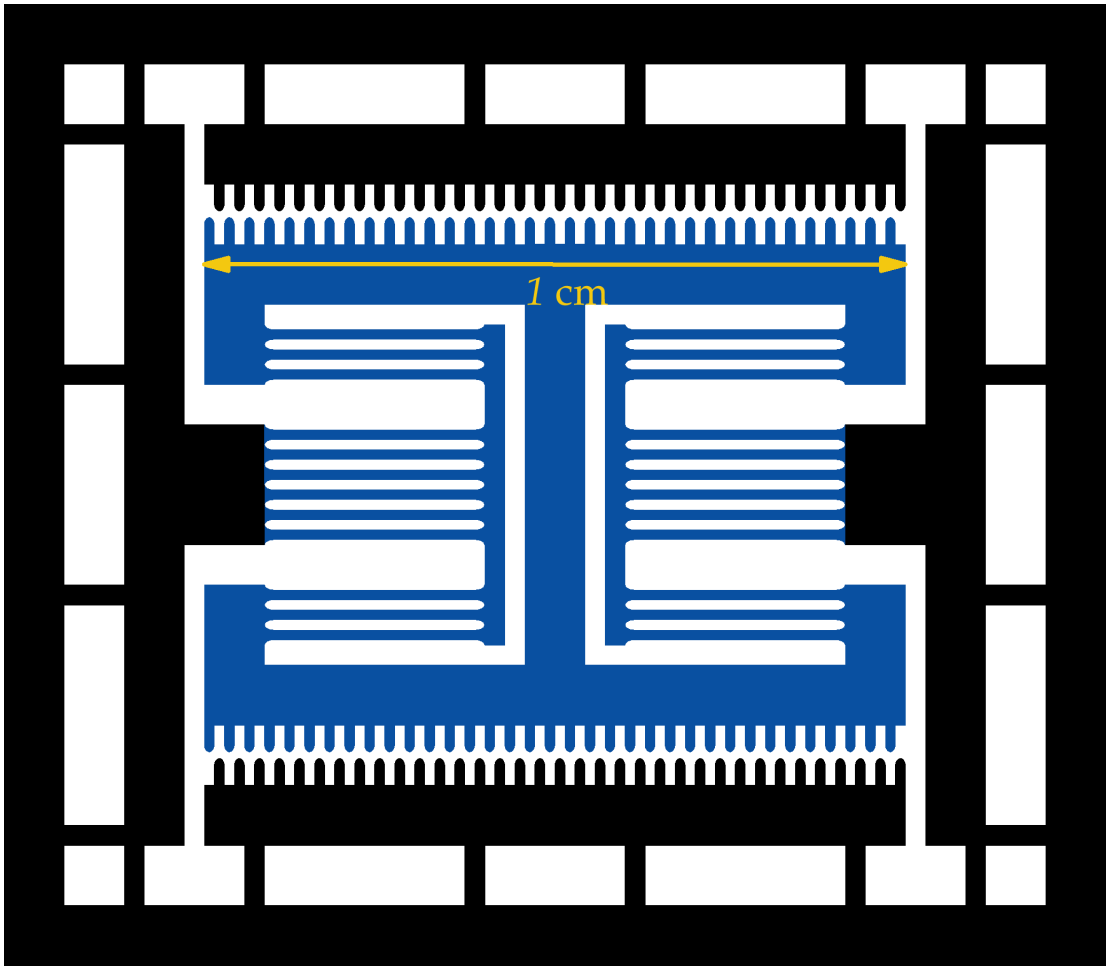

Figure 6-4: Plan view of a constant-gap energy harvester with non-overlapping fingers.

which is slightly smaller than the desired 79 pF change.

An alternative design, shown in Figure 6-4 constructs non-overlapping fingers to minimize the gap between them. This sacrifices the effective travel distance by a factor of two. The minimum gap is now limited by the straightness of the vertical walls and the run-out of the etch which limits how close can the etch be performed reliably. State-of-the-art etching [35] shows that the the wall can be expected to vary 2 μm. This constraints the average minimum gap to 2 μm. To insure that the surface irregularities don't scrape past each each, the gap will be assumed to be 4 μm. With this design, a comb-drive with 50 μm-thick fingers and total width of 1 cm, which effectively travels now 600 μm will provide a change of capacitance of

$$\epsilon_0 \frac{500\ \mu\text{m}}{4\ \mu\text{m}} 2 \cdot 600\ \mu\text{m} \frac{1\ \text{cm}}{50\ \mu\text{m} + 4\ \mu\text{m}} = 246\ \text{pF} \tag{6.10}$$

which is enough to provide the desired 79 pF change. The fabrication of such a device was attempted, but fabrication issues made it impossible to obtain a useful device. These issues will be discussed in Chapter 7. Further research can determine if the fabrication problems can be overcome without compromising the requirements of this design.

6.3 Large-Travel Spring Design

Large-travel motion with minimal yaw and lateral translation is essential for applications with long comb fingers and narrow gaps, or those requiring precise alignment of its parts [40, 16, 15], as does the comb-drive designs of the previous section. The suspension must permit long travel along one axis of the supported mass, while rejecting travel along the other two axes and rotation about all three axes to keep the fingers from crashing. Current bending-beam suspensions offer between 5 and 10 μm travel with 200 μm-long beams [14, 36], 30 μm travel with 800 μm-long beams [16], and 130 μm travel with 1100 μm-long beams [21]. None of these references describe the lateral translation or yaw rotation of their suspension.

Furthermore, the constant-gap variable capacitors shown in Figures 6-3 and 6-4 have masses much smaller than that of the constant-gap variable capacitor described previously. Recall that Chapter 4 fixed the product of MX so that the resonating mass-spring could extract 24 nJ from the available acceleration of $0.02g_E$. The values chosen for the constant-gap variable capacitor were a mass of 195 mg and a travel of 200 μm. The mass needed to be plated with 41 μm of gold to reach the required mass.

The area of a constant-gap variable capacitor is much smaller than that of a constant-gap variable capacitor. The alloted 1 cm $\times$ 1 cm has to house the suspension and the combs. The resulting mass is only 36 mg, compared to the 116 mg of the variable-gap capacitor, assuming all the mass is silicon with a standard wafer thickness of 500 μm. However, the constant-gap devices can travel farther, reducing the mass requirement. With the travel computed in the previous section of 1,200 μm, a sixfold increase over the 200 μm required travel, the required mass is reduced to 32 mg. The previous section explored the design of suspensions composed of multiple thin beams. This section explores the design of long-travel suspensions which address the problems of minimal yaw and lateral translation which may

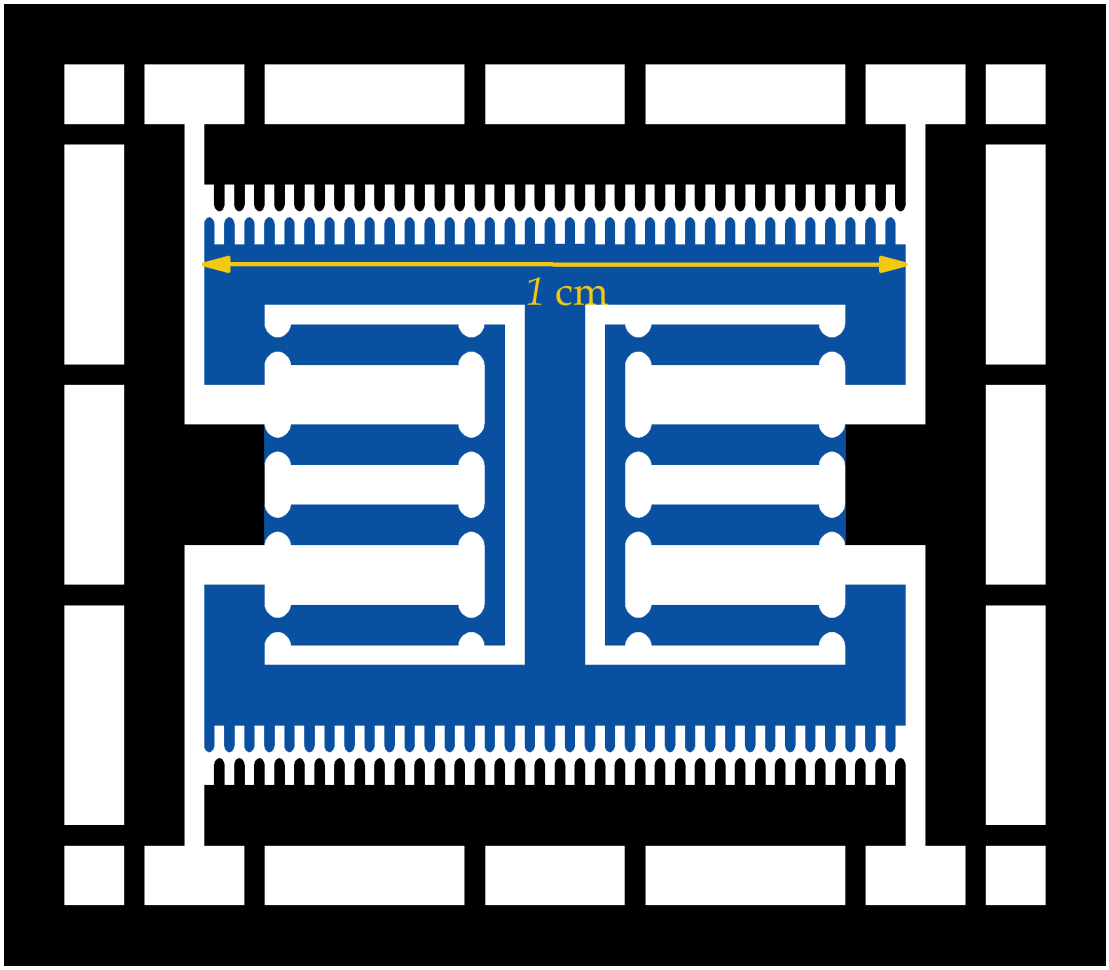

Figure 6-5: Plan view of a constant-gap energy harvester with non-overlapping fingers and four-bar linkage suspension.

arise with long-travel using a suspension composed of flexure spring and thick, rigid beams. These suspensions will also be compared to the multiple-beam suspensions of the previous section.

The suspension shown in Figure 6-5 consists of thick free rigid beams, compact flexure springs and anchors. The beams are arranged to form two nested pairs of four-bar linkages, one pair on each side of the mass, and are joined by the flexure springs. The lateral translation and yaw rotation in this suspension is dictated by the location of the flexure springs, not by any beam width or flexure dimension. Thus, its kinematics are robust against fabrication errors, and its in-plane motion can be limited to simple linear travel. Additionally, because

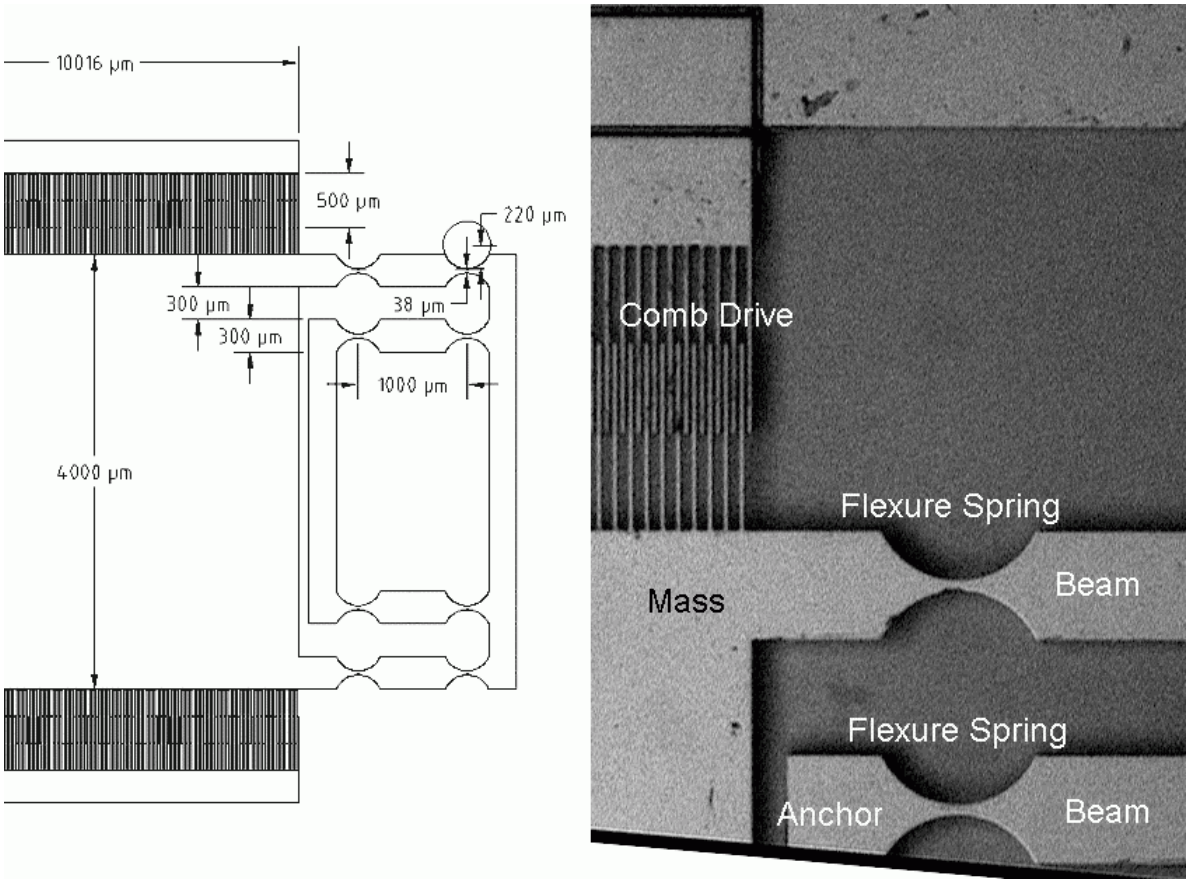

Figure 6-6: Fabricated example of a four-bar linkage with flexure suspension. The device depth is 90 μm. The resonant frequency is $f = 1.3$ kHz, with a maximum stress at $X = 250$ μm of 0.5% of the Young's Modulus of silicon (155 GPa).

the beams and flexure springs have a large thickness, the suspension offers considerable stiffness against out-of-plane translation and rotation.

The suspension is folded into the mass to allow a more compact design and open some members to allow construction as a single connected piece, to be separated later using break-off tabs. This allows the critical high-risk etch to be performed first, before any subsequent processing is performed.

Existing suspension designs which involve long bending beams as springs [16, 15, 14, 36, 21] are sensitive to errors in fabrication resulting in differences in beam thickness, which affect their ability to limit lateral translation and yaw rotation. The direction of travel of the suspension shown in Figure 6-5 is determined only by the location of the flexure springs, and not by the thickness of any member of the suspension.

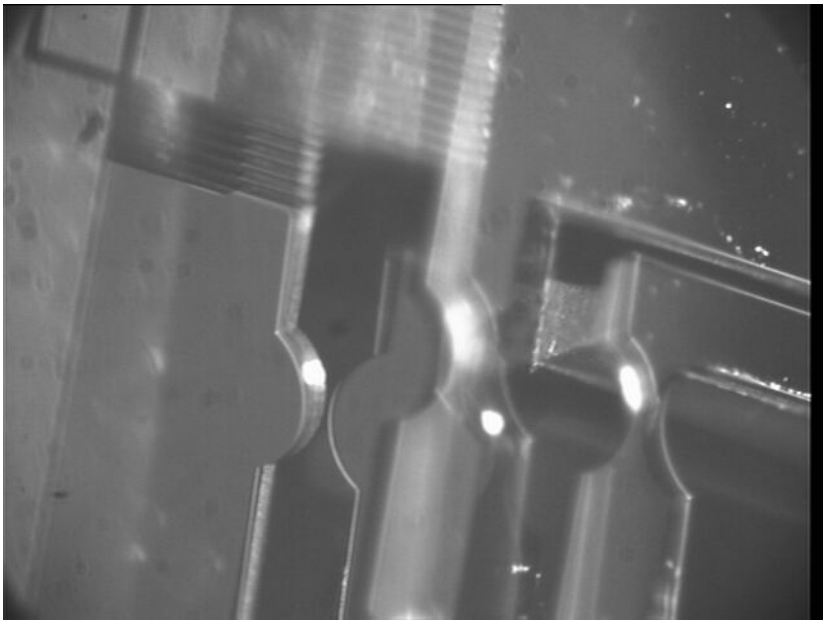

Figure 6-7: Fabricated example of a four-bar linkage with flexure suspension. The angled perspective shows part of the comb in the upper-left corner, part of the shuttle mass in the upper-right corner, the anchor to the left, the flexure springs in the center and part of the rigid suspension beams to the bottom. The reflection in the center shows the spring flexure from below.

Figures 6-6 and 6-7 show a fabricated example of a four-bar linkage with flexure suspension. The flexure spring thickness is 38 μm and the flexure spring radius is 220 μm. The depth of the structure is 90 μm, and the rigid beam length is 1,000 μm. The shuttle mass has dimensions of 4,000 μm $\times$ 10,000 μm. This yields a mass of 8.4 mg. Appendix F derives the equations for spring constant and maximum stress of this suspension. Using the design shown here, the resonant frequency of the device is $f = 1.3$ kHz, and for a maximum displacement $X = 250$ μm, the maximum stress in the flexure is 0.5% of the Young's Modulus of silicon (155 GPa). As a rule of thumb, the stress should not exceed 1% of Young's Modulus to avoid fractures.

The drawback of this design is that the internal stresses on the flexure spring may be too large for the required travel. Internal stress in the flexure springs may be reduced by changing a few thick springs into several thin springs, as shown in Figures 6-3 and 6-4. This design still keeps the advantages of a four-bar linkage, but is sensitive to fabrication errors which may alter beam width.

6.4 Summary

This chapter explored constant-gap and variable-gap capacitors and provides designs for each type which can provide the 79 pF capacitance change required in Chapter 3, as well as the mass and travel required in Chapter 4. This chapter assumes that MEMS fabrication technology will be used to create these devices. Chapter 7 will propose fabrication processes to create these, offer solutions to some problems that arose in the fabrication of these devices and discuss other problems that made impossible the creation a working harvesters.

Constant-gap capacitors appear to be ideal to create variable capacitor in which the change of capacitance is not critically sensitive to variations in travel distance and timing errors. However, they require long travel distances due to their reduced mass and in order to create the necessary capacitance. The suspensions proposed in this chapter, although in theory should not present any major problems, have not been experimentally tested. However, constant-gap capacitors also required high aspect-ratio etches. Etching these structures using MEMS fabrication technology proved extremely difficult, and Chapter 7 will address all the issues encountered.

Variable-gap capacitors, while less attractive from a control standpoint due to their capacitance change over time, are able to create larger capacitance changes with less travel, while providing more area to achieve a large mass. More importantly their fabrication process relies on well established fabrication techniques which do not require high-risk steps. Chapter 7 will also propose a fabrication process to create these structures.

Chapter 7

Fabrication Processes

This chapter proposes fabrication processes to create the variable capacitors described in Chapter 6 using MEMS fabrication technology. The processes rely heavily on deep reactive ion etching (DRIE). The process for creating a variable-gap capacitor is only described. Given its similarity with other projects [43], no experimental runs were attempted. The process for creating a constant-gap capacitor is also described. This process was attempted, but no working devices were created. A discussion of the problems arising from fabrication follows. Explanations for some of these problems will be discussed, as well as tried and proposed solutions. Finally, the variable-gap capacitor will be recommended as a lesser-risk choice over the constant-gap capacitor from the standpoint of fabrication, although the latter is preferred from a performance standpoint. Goals in fabrication technology that will enable the creation of successful constant-gap variable capacitors using the techniques described in this thesis will be discussed in Chapter 8.

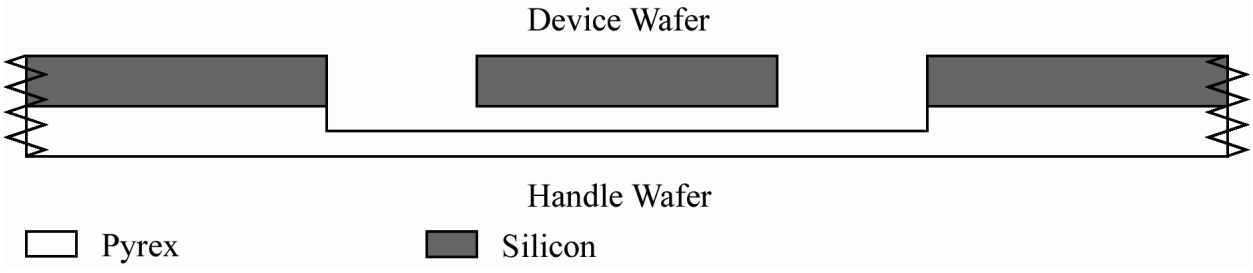

Figure 7-1: Side view of a constant-gap energy harvester.

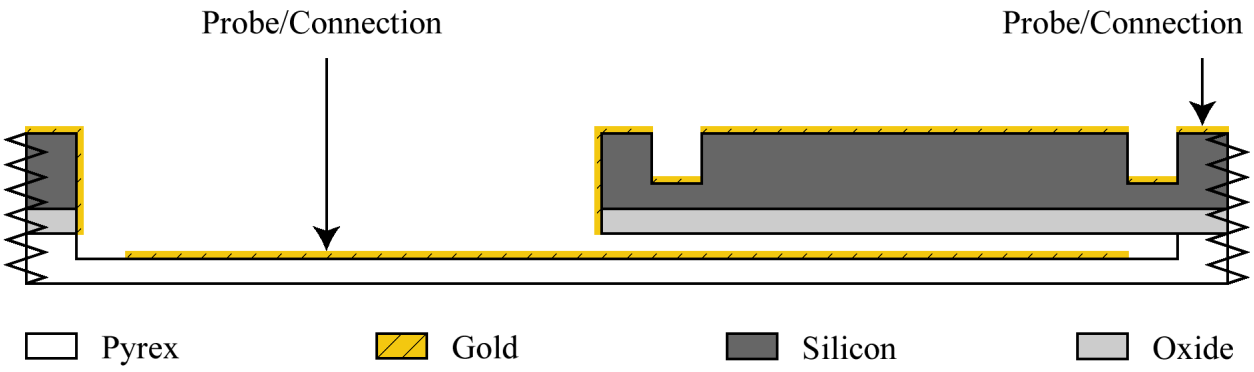

Figure 7-2: Side view of a variable-gap energy harvester.

The fabrication process of both the variable-gap and the constant-gap converters are designed to be a simple as possible. The fabrication process of the constant-gap energy harvester is the simplest process, but the DRIE step required to define its features used in this thesis is not adequate. Since the structure, as drawn, is completely connected, the first step is the through-etch of the actual design in a 500 μm-thick silicon wafer. This critical etch is done in a Surface Technology Systems (STS) etcher using the Bosch process [6, 5, 7]. The wafer must have a high enough doping concentration to be considered a perfect conductor. Once the critical etch is done, the next step is to etch pit holes in a quartz or Pyrex® wafer [23]. These pits must be deep enough for the moving mass to glide above them. A distance of about 10-20 μm has been found sufficient in similar applications [28, 29, 23]. Once both wafers are ready, an anodic bond can join them. Once the device is securely bonded, the small tabs connecting the device to the field silicon can be broken off, achieving electrical isolation. Figure 7-1 shows a side view of the final device. A detailed fabrication process for the constant-gap energy harvester can be found in Appendix G.

The variable-gap device requires a more complex fabrication process, but the process has been refined in other projects [43]. Furthermore, none of the fabrication steps is considered particularly critical. Again, the process starts with a DRIE step on a heavily doped silicon wafer. However, the etch is timed, so that the thin membranes that will act as springs are left at the bottom of the wafer. If needed, a layer of metal may be deposited over the wafer to insure a good connection between the shuttle mass and the field silicon. Also, the bottom of the shuttle mass will travel down closing the gap. In order to a void pull-in problem, it

may be necessary to etch stops on the backside of the wafer. Again, a Pyrex® or quartz wafer is etched to allow the vertical travel of the shuttle mass. However, the depth of the etch is now critical, as it defines the minimal gap of the capacitor. Furthermore, this is a deep etch (about 200 μm for the proposed design), and such deep etch of Pyrex® presents challenges, while it may be even harder or impossible for a quartz wafer. Once this critical etch is performed, the bottom of the pit must be covered with metal using a shadow mask. This metal layer creates the other terminal of the variable capacitor. Once both wafers are ready, an aligned anodic bond will finish the device. The detailed fabrication process for this variable-gap harvester is in Appendix G.

7.1 Fabrication Challenges And Recommendations

No attempts were made to fabricate a variable gap converter since creation of similar devices is documented [43]. A proposed mask for this design is shown in Appendix H. Although several successful comb-drive structures have been reported, none has the necessary depth or travel to satisfy the capacitance requirements. Appendix H shows a pair masks designed to create both overlapping and non-overlapping constant-gap harvester. Several runs were attempted to fabricate this device, but none yielded a working device due to the problems explained in this section. Furthermore, fabrication problems imposed constraints which eroded the device performance, as discussed below.

The first problem with the through-etch occurs with different etch rates of different width gaps. Since the Bosch process alternates between passivation and etching cycles, byproducts from each reaction have to dissipate before the next step can take place. With wide open spaces this transport is not a problem. However, the small gaps in between the fingers etch more slowly than other open spaces. Open spaces will clear through a 500 μm wafer in about 2-3 hours. Small spaces can take as long as 6-8 hours. Cleared structures overetch sideways and break or disintegrate. Figure 7-3 shows overetched fingers after an 8.5 hour etch. Furthermore, the etch rate is uneven across the wafer leading to some devices left either underetched or overetched.

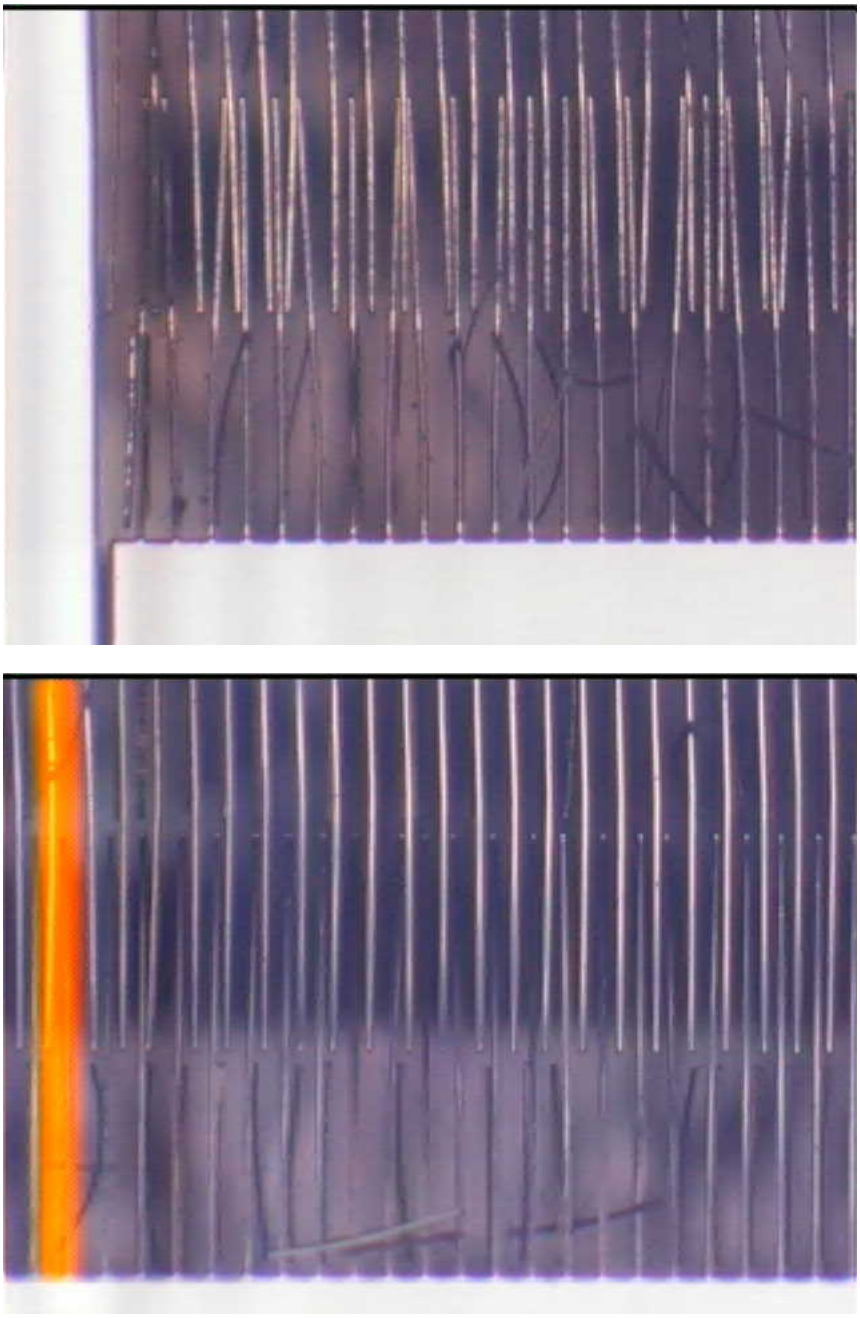

Figure 7-3: Overetched fingers on a wafer etched with the Bosch process for 8.5 hours.

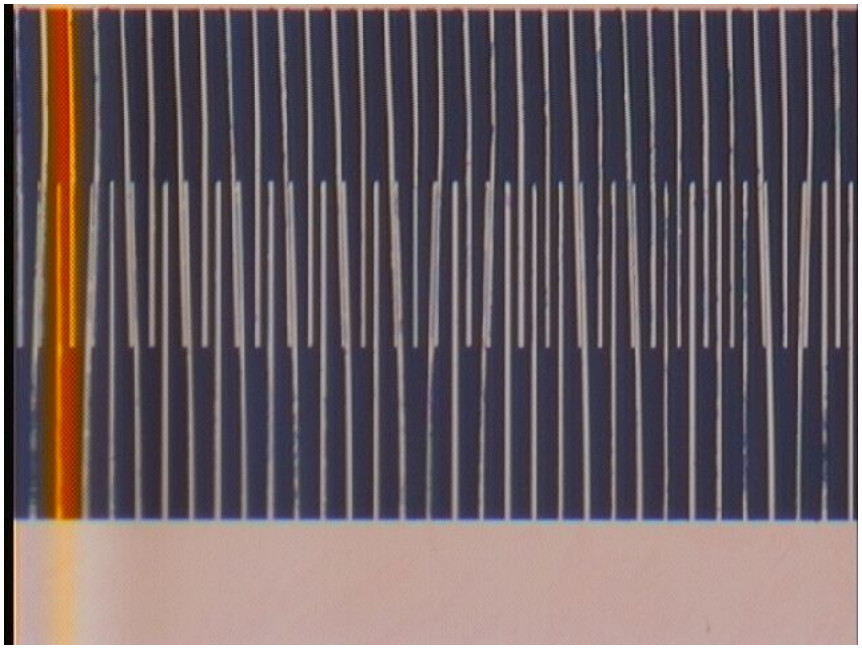

Figure 7-4: Fingers fused by stiction.

The solution to the problem of differing etch rates is to use halo pieces in the large spaces that fall out after the etch is completed. These halo pieces even the gaps presented to the etcher so that the fingers don't clear first. This means that a through-etch will extend even longer leading to thermal problems discussed later. Also, some halo pieces are very small and can easily become lodged in crevices, or between the fingers. Even if these pieces don't actually lodge physically, they exarcebate the problems with subsequent wet processing.

In general, wet processing of the etched structure must be avoided. Even though the fingers may be designed to withstand electrostatic attraction, the surface tension of water as it drains is far larger. Fingers can easily fuse together, as shown in Figure 7-4. If halo pieces are used, this problem is multiplied. One solution to this problem is to avoid wet processing altogether, or to freeze dry the wafer using methanol [13]. These solutions are not perfect, and the sticking is compounded by the presence of resist on the wafer. The primary reason to use wet processing after the through-etch is to eliminate the resist used as a mask. One of the best ways to clean the wafer after etching is to use a piranha clean. The violent action of the hydrogen peroxide bubbles serves to mechanically dislodge the debris. Oxygen plasma may also be used to remove the resist, but the amount of debris left over in the chamber makes it undesirable for a shared clean room device. Other brute force techniques such as

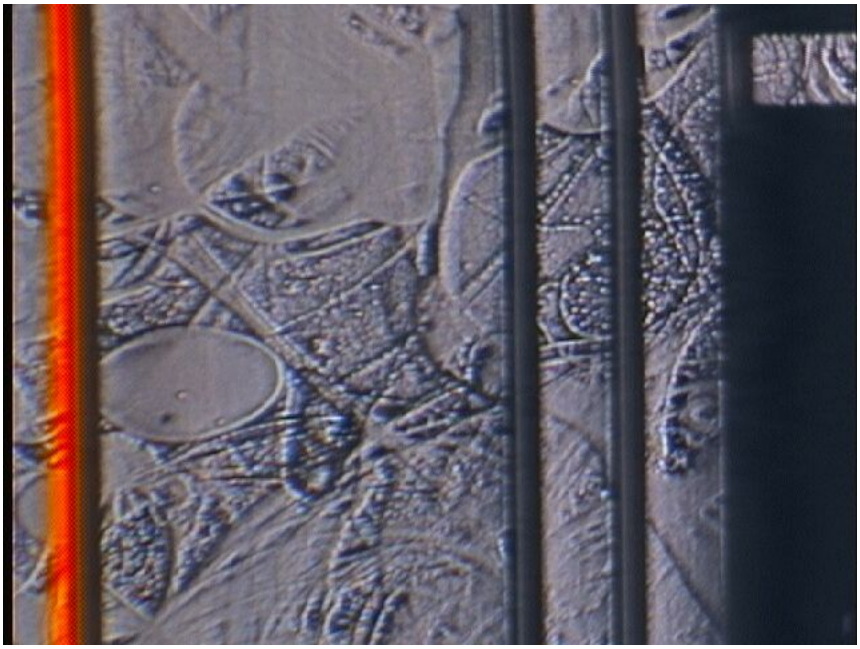

Figure 7-5: Surface roughness after resist burned.

tapping the wafer of using tweezers can easily lead to destruction of devices and even larger amounts of debris. Note that a comb-drive device needs to be perfectly isolated in order to hold the charge constant. A single piece of debris will render an otherwise perfect device useless.

Another problem with comb-drive fabrication is the mechanical release and electrical isolation between the different sections of the device. The easiest approach is to allow the etch to separate fully the pieces as it etches through. This solution usually works well in short etches. In long duration etches, the temperature of the wafer rises dramatically. If the heat is not allowed to escape, the temperature will burn away the resist quickly, rendering it useless. Once the resist is burned, it will not protect the wafer properly and the etch features will quickly be deformed, as shown in Figure 7-5. If the pieces become mechanically isolated during the etch, they will not be able to release the heat to the rest of the wafer. Thus, the resist on top of localized isolated sections will burn prematurely. If long duration etches are necessary, the wafer must remain thermally connected at all times.

Even with a fully connected wafer, some parts will not be able to release the heat properly depending on the path the heat must take. In particular, very thin fingers must rely on their thickness to transfer the heat outside. Thus, to avoid the finger's resist from burning off, the

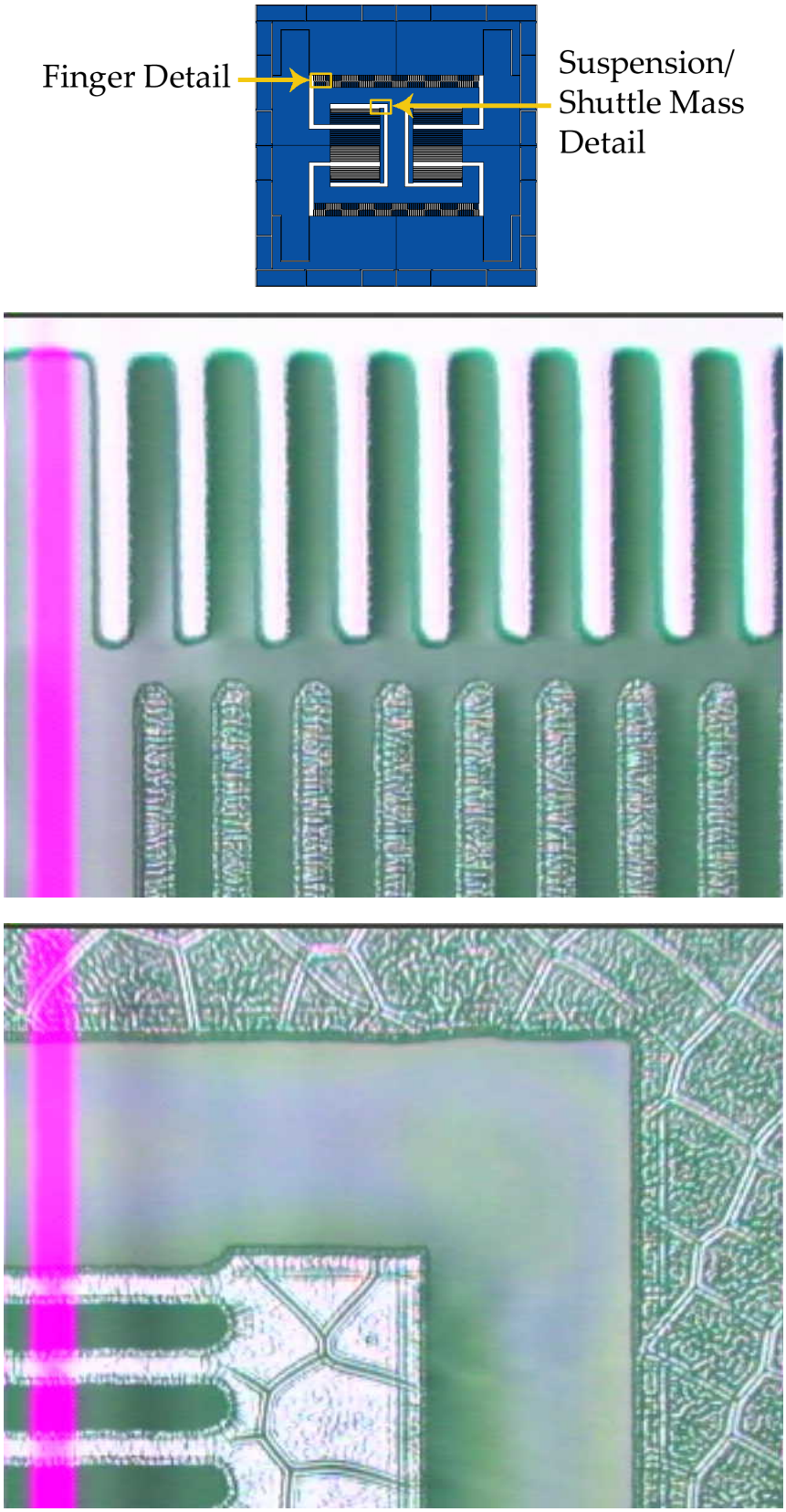

Figure 7-6: Burned resist on a device etched with the Bosch process for 3 hours.

thickness must be larger than what can theoretically be achieved with the Bosch process. Another source of thermal resistance is the suspension structure. As it clears, all the heat contained in the shuttle mass must dissipate through the thin beams of the suspension. Figure 7-6 shows a 500 μm wafer with a 1 μm thermal silicon oxide mask and 10 μm thick photoresist. The wafer is mounted on a quartz wafer. The quartz wafer is fully covered with thin resist at about 5,000 rpm to minimize the thickness of the resist and maximize the heat transfer between the device wafer being etched and the quartz handle wafer. The mounted wafers were baked for 20 minutes at 90°C. After a three-hour etch, almost all features had cleared through the 500 μm wafer, except the 50 μm narrow channels between the springs and the 50 μm channels between fingers. The zigzag channel between the two sets of fingers did clear much faster, and provided thermal isolation between the top and bottom anchors and the central shuttle mass. The I-shaped shuttle mass shows signs of burned resist. The severity of the burned resist decreases from the shuttle mass through the suspension toward the side anchors. The first figure shows an overview of the device, marking the areas of detail shown in the next two pictures. The second figure shows a detail of the comb drive. The bottom fingers, attached to the shuttle mass, show burned resist. The top fingers, attached to the top anchor, show the resist in perfect condition. The third figure intends to show the gradual transition from burned resist in the I-shaped shuttle mass to the resist on the side anchors which showed no signs of burn damage. The floating beam, halfway in the thermal path between the shuttle mass and the side anchors, shows some signs of burning, but not as dramatic as in the shuttle mass. The condition of the side anchors was as good as that of the top and bottom anchor.

Another method to create isolation between devices is to die saw across dividing gaps. Figure 7-7 shows a die saw cut across such a structure, where the pieces to the right are now isolated from each other. The problem with the die saw is that is it both a process that creates a lot of debris and uses water to cool down the blade and wash out the excess debris. However, some of the resulting slurry may short the devices and cause stiction problems. The wafer can be covered with tape to avoid some of these issues, but removing the tape tends to tear away fingers and spring beams.

Figure 7-7: Device isolation using a die saw. Corner detail of a die from Mask 7 H. The darker line with rough edges to the left is the die saw trail.

Probably the best solution is to use break-off tabs, such as the ones shown in Figures 6-3 and 6-4. These tabs have been used successfully in other devices [28, 29, 23]. However, break-off tabs reintroduce the thermal conduction problem since now all of the heat in a device must escape through them to reach the silicon field. However, the device shown in Figure 7-6 has break-off tabs surrounding the device. The resist on the top and bottom anchors did not show any signs of burning, nor did the resist on the large side masses to which the suspension is attached. This implies that the thermal path through the break-off tabs can be sufficient to avoid burning the resist if the tabs are large enough. Furthermore, since the area of silicon they enclose is larger, the thermal capacity is increased, as well as the thermal conduction down through the bottom of the wafer.

Chapter 8

Conclusion

The primary goal of this chapter is to bring together the analyses presented in earlier chapters to examine the practical performance of electrostatic vibration energy harvesters. To this end, Section 8.1 begins with a summary of what has been learned. Section 8.2 brings this knowledge together to investigate performance. This is done first in the context of the design example that has run throughout this thesis, and then more generally. Section 8.3 provides a system view of the overall design and computes some useful metrics. Finally, Sections 8.4 and 8.5 provide general conclusions and suggestions for future work, respectively.

8.1 Summary

Chapter 2 derives the equations that describe an energy conversion cycle in the QV plane. For a charge-constrained cycle, Equation 2.3 shows that the energy converted is

$$\Delta E_{\text{charge constrained}} = \frac{1}{2}\Delta C V_{low} V_{high} \tag{8.1}$$

Similarly, for a voltage-constrained cycle, Equation 2.4 shows that the energy converted is

$$\Delta E_{\text{voltage constrained}} = \frac{1}{2}\Delta C V_{high}^2 \tag{8.2}$$

The advantages and disadvantages of each cycle are discussed. A voltage-constrained cycle seems a worse proposition to implement because it requires a high voltage source and the associated power electronics might suffer from more losses than a charge-constrained cycle which converts a comparable amount of energy. Therefore, this thesis focused on a harvester built around a charge-constrained energy conversion cycle. A charge-constrained cycle where the variable capacitor is charged to 17.7 V at a C_{max} of 168 pF, and discharged when its capacitance reaches 89 pF converts 23.4 nJ of energy. The highest voltage in the variable capacitor is 33.5 V. This cycle is the basis of a proposed energy harvester which is developed throughout the thesis.

Chapter 3 explores power electronics to implement the conversion cycles described in Chapter 2. A test circuit is built to implement a charge-constrained cycle. A model of this test circuit is simulated. The agreement between the results and the measurement validate the model. Next, new power electronics are proposed to implement the example charge-constrained cycle described in Chapter 2. These include MOSFETs with an output capacitance of 10 pF and an inductor with a Q of 50. These power electronics are simulated using the model. The results indicate that the power electronics implement a charge-constrained cycle where the variable capacitor harvests 24 nJ. The power electronics deliver 2% of this energy, for a final energy gain of 0.5 nJ at the reservoir. The bulk of the energy is dissipated in the inductor and the MOSFETs. The inductor dissipates 12.6 nJ and the MOSFETs dissipate 11.3 nJ. Section 8.2 uses the simulation to find the effect of using better components. For instance, by decreasing the MOSFET output capacitance from 10 pF to 1 pF, the efficiency increases to 54%. In the original design of the power electronics, the energy gain of 0.5 nJ implies a power output of 1.3 μW at 2.5 kHz. The system is assumed to operate at 2.5 kHz; this is justified in Chapter 5.

Chapter 4 develops a generalized linear model of the harvester which applies as long as Equation 4.17 holds. The requirement on the Q of the system is

$$Q = 2\pi \frac{\frac{1}{2}M\omega^2X^2}{E_e + E_m} = \frac{\frac{1}{2}M\omega^2X^2}{\frac{1}{2}MaX} = \frac{\omega^2 X}{a} >> 1 \tag{8.3}$$

Given that this requirement is fulfilled, Equation 4.13 constrains the mass and travel of the shuttle mass using the acceleration of the source and the energy conversion cycle,

$$E_{in} = E_e + E_m = 2\pi\frac{1}{2}MaX \tag{8.4}$$

For the energy conversion cycle proposed in Chapter 2, the energy harvested by the variable capacitor is 24 nJ. Again, the frequency of the energy vibration source is assumed to be 2.5 kHz. Furthermore, the magnitude of the acceleration of the vibration source is assumed to be $a = 0.02g_E$, where $g_E = 9.81$ m/s^2 is the acceleration of gravity. This assumption is also justified in Chapter 5. With these numbers, Equation 4.13 is satisfied with a mass $M = 195\ mg$ and a travel amplitude of $X = 200\ \mu$m, for example. This mass and displacement serve as the basis of the design of the structure of the variable capacitor in Chapter 6.

Equation 4.17 is checked using ω, a and X. The resulting Q is 250,000, which satisfies $Q >> 1$. However, similar systems in the literature report mechanical Q's as low as 10,000 at these low frequencies [24, 37, 38], so that the mechanical energy loss E_m may not be ignored. Once this energy loss is known, it can be incorporated into Equation 4.13, which will constrain the product MX further. However, for purposes of this thesis, the mechanical losses are assumed to be zero.

Equation 4.12 states that, assuming $E_e >> E_m$, $P_e \approx \frac{1}{2}M\omega aX$. Therefore, for a given M and X, as limited by fabrication and structural constraints, the converted power will be maximized by maximizing the product ωa. This product will become a useful metric with which to compare the spectrum peaks of a vibration source. This observation is independent of the exact means of mechanical to electric energy conversion.

Chapter 5 explores sources of vibration energy and justifies modeling the source as a sinusoid at 2.5 kHz with an acceleration magnitude of 2% of g_E. In fact, using the metric of maximum ωa product, as discussed in Chapter 4, it was seen from typical vibration spectra that the best frequency at which to operate a vibration-to-electric energy converter is in the 1-5 kHz range, regardless of the actual transduction method used. The relatively high

acceleration magnitudes observed in rotational machinery, such as turbines and compressors, make these machines the best initial targets for this application.

Chapter 6 describes two different types of variable capacitors: constant-gap and variable-gap. Equation 6.4 states that the change in capacitance for a variable-gap capacitor is

$$\Delta C_{\text{variable gap}} \approx \epsilon_0 \frac{A}{g - X} \tag{8.5}$$

where $g \approx X$ for the approximation to hold. The change in capacitance required by the energy conversion cycle of Chapter 2 is 79 pF. A 1 cm $\times$ 1 cm variable-gap capacitor is proposed. Assuming a shuttle mass travel of $X = 200$ μm, the nominal gap must be $g = 11$ μm. In order to achieve the required mass of 195 mg from Chapter 4, 41 μm of gold can be electroplated on top of the 500 μm of silicon provided by a standard thickness wafer to make the variable capacitor. A simple suspension consisting of a membrane spring which surrounds the shuttle mass is proposed. To insure low stress, the length of the membrane spring is set at 2 mm, so that the travel of 200 μm represents only 10% of the membrane spring length. Taking all four 1 cm sides as the width of the spring, the thickness of the silicon necessary to resonate at 2.5 kHz with 195 mg is 40 μm.

Equation 6.7 states that the change in capacitance for a constant-gap capacitor is

$$\Delta C_{\text{constant gap}} = \epsilon_0 \frac{T}{g} 2X \tag{8.6}$$

However, this type of constant-gap capacitor requires the travel X or the ratio T/g to be too large. A better design is a comb-drive, in which multiple constant-gap capacitors are connected and the total capacitance change is

$$\Delta C_{\text{comb drive}} = \epsilon_0 \frac{T}{g} 2X \frac{L}{w + g} \tag{8.7}$$

as stated in Equation 6.8. Even with this design, the requirements placed by fabrication technology on the width of the fingers and the gaps yield a change in capacitance too small. A better design creates non-overlapping fingers where the finger density can be increased at the cost of effective travel. With current DRIE technology, the gap is expected to be 4 μm [35].

The finger width is set at 50 μm to insure dynamic structural and electrostatic stability. The design shown in Figure 6-4 packs these fingers into a 1 cm-long comb. The suspension beams are 3,000 μm long, and the shuttle mass is expected to travel 1,200 μm. However, since the fingers overlap only during half of the travel of the shuttle, the effective travel is only 600 μm. With wafer thickness of 500 μm, Equation 6.8 predicts a change in capacitance of 246 pF, which is more than the desired 79 pF. However, fabrication problems with this device are discussed in Chapter 7.

Chapter 7 proposes fabrication processes to create both the constant-gap and variable-gap capacitors described in Chapter 6. The fabrication process for the constant-gap capacitor mimics well-established processes for creating valves [43], so that experimental investigation was not pursued. Attempts to fabricate a constant-gap capacitor were unsuccessful, and the problems encountered during fabrication are discussed, as well as some solutions attempted or proposed. Even though a constant-gap capacitor is preferred in terms of electric performance, in light of the fabrication experience a variable-gap capacitor seems easier to create using current MEMS fabrication technology.

8.2 Design

The design process described in this thesis is highly iterative. This thesis shows that no single design is preferred. The first step is to choose a conversion cycle and an associated power electronics to implement this cycle. The losses in the power electronics will feed back to the design of the cycle. This analysis bounds the restrictions on ΔC and C_{min}.

With this information, the type of device which can provide this change of capacitance must be chosen. The electromechanical analysis indicates whether the travel and mass are adequate to couple to external vibration, as dictated by Equation 4.12. The structure of the capacitor indicates what changes in capacitance can be achieved by this device, and what are the constraints it imposes on the control electronics.

Once a suitable mechanical design has been found, the technology which can more easily create such a device must be chosen. Further constraints from the chosen technology can

feed back to the ability of the device to provide the necessary capacitances or to couple to external vibrations.

The proposed energy harvester consists of a square centimeter with 195 mg of mass which travels ± 200 μm. This mass and travel can couple to a sinusoidal acceleration source of $0.02 g_E$ at 2.5 kHz, typical of rotating machinery so as to bring 24 nJ into the converter per cycle. In order to resonate at this frequency, a simple membrane spring of 2 mm length, surrounding the shuttle mass, has to be 40 μm thick. Adding a capacitor of 88 pF in parallel with this device will result in the capacitance change from 168 pF to 89 pF required by the 24 nJ charge-constrained cycle proposed in Chapter 2. This device can be attached to the proposed power electronics of Chapter 3, which will implement the charge-constrained cycle and deliver 0.5 nJ back to the reservoir for a total power output of 1.3 μW at 2.5 kHz.

The power electronics, however, are very lossy, with an efficiency of 2%. If this efficiency is increased, the energy required on the conversion cycle is smaller. This allows some vibration energy to be used to cover the mechanical loss in the resonator, as well as the energy consumption of the control and sensing electronics associated with the power electronics. Furthermore, it also relaxes the requirements on travel and mass to couple to an external vibration source. A lower energy requirement also relaxes the requirements on the variable capacitor so that its fabrication might be easier.

A variable-gap capacitor seems to accommodate even larger masses and travel without paying a penalty in capacitance change as long as the minimal gap is achieved. However, as the ratio of travel to gap increases, the capacitance change will be increasingly difficult to capture, and small variations in travel will result in large variations of capacitance. A constant-gap capacitor does not suffer from this drawback since the capacitance change occurs throughout the whole or at least half of the travel of the mass. Small variations in travel will result in correspondingly small variations in capacitance change. Furthermore, as the travel is extended to accommodate other constraints, the relation between variations in travel and capacitance change holds proportionally. However, creation of large capacitance changes in a constant-gap capacitor is more difficult since it requires aspect ratios that are hard to create with current fabrication technology. Furthermore, the area of the shuttle mass

is smaller due to the space needed for the suspension and the combs. Thus, achieving the desired mass is more difficult.

Decreasing the losses in the power electronics will a have major impact in the power output of the harvester. The losses in the power electronics of Chapter 3 are dominated by the inductor and the MOSFETs. The inductor used has a realistic Q of 50 and MOSFET capacitances of 10 pF. These result in a conversion of only 0.5 nJ out of the 24 nJ presented by the variable capacitor, for a 2% efficiency and a power output of 1.3 μW at 2.5 kHz. Increasing the Q of the inductor to 500 by lowering the series resistance and core losses, while keeping the energy conversion cycle the same, results in an energy output of 8 nJ out of 24 nJ, for an efficiency of 33% and a power output of 20 μW. Decreasing instead the MOSFET output capacitance to 1 pF, while also keeping the energy conversion cycle the same, results in an energy output of 13 nJ out of 24 nJ, for an efficiency of 54% and a power output of 33 μW. Increasing the Q to 500 and decreasing the output capacitance to 1 pF results in an energy output of 21 nJ out of 24 nJ, for an efficiency of 88% and a power output of 50 μW.

Increasing the inductor Q to 500 seems harder than decreasing the MOSFET output capacitance to 1 pF. Furthermore, the gain resulting from lowering the output capacitance is larger than the gain resulting from increasing the Q of the inductor. This argues strongly for the use of integrated circuits in which the output capacitance of the MOSFET can be tailored to this application.

Note that the voltage levels in the cycle, 34 V, are higher than what normal Very-Low-Power electronics technology would allow. In order to make MOSFETs that can withstand these high voltages, a mixed circuit technology must be used. On the other hand, reducing the amount of charge delivered to the variable capacitor also minimizes the maximum voltage of the circuit. If V_{high} is set at 19 V, so that the maximum voltage across both MOSFETs is 20 V, the resulting conversion cycle will produce 7.4 nJ instead of 24 nJ. Simulating this cycle with an inductor Q of 50 and an output capacitance of 1 pF results in 4.5 nJ delivered to the reservoir, for a power output of 11.3 μW and an efficiency of 61%. Note that this result is in perfect agreement with the power output square-voltage dependance. Note that Amirtharajah computed that only 170 nW were necessary to make a useful computation [3].

Company (Part)	Q	DCR (Ω)	f_{test} (kHz)	I_{max} (mA)	SRF (MHz)	W×L×H (mm)	Notes
TOKO (395GN-0090IB=P3)	70	7.3	252	57		6×6.8×4.3	
TOKO (262LY-102K)	80	9.0	252	50	2.1	8(dia.)×6.2	
ctparts.com (CTDS1608C-105)	40	3.4	100	150		6.6×4.45×2.92	shielded
ctparts.com (CTDS1608BL-105)		9	100	100	2	6.6×4.45×2.92	>10 MΩ insulation core-winding, shielded
ctparts.com (CTLQ2220C-102M)		14.42	10	150	1.7	6×5.3×5	

Table 8.1: Surface-mounted inductors with $L = 1$ mH $\pm$ 20%.

Thus, the maximum voltage may be reduced to avoid a mixed circuit technology if the decrease in power output is acceptable.

8.3 System Integration

The harvester as designed in this thesis would be an autonomous device. In this case, the complete system would include the actual device, associated power electronics (including an inductor and a reservoir capacitor) and control and sensing electronics. The total area of the variable capacitors proposed in this thesis is about 2 cm^2. The inductor used in the experiment was large; Table 8.1 shows the dimensions for smaller, surface-mounted inductors. Another square centimeter is added to account for both the inductor and the reservoir capacitor. The rest of the electronics can presumably be incorporated into the device itself. The thickness is in the order of 0.5 cm to account for the inductor. The total volume would thus be about 1.5 cm^3. The weight of this package would in the order of one gram, noting that most of volume would not be solid. An inductor smaller than 1 mH would reduce the size and weight further, but the requirements on the timing circuitry will increase accordingly.

Useful metrics must be devised to compare the effectiveness of this device as an energy source against other sources. If the vibration energy source may be assumed to be an infinite source of energy, one of these metrics could be power output/weight or power output/volume.

The proposed device has power output of 1.3 μW, so the final power per volume would be 0.87 μW/cm^3 and the power per weight would be 1.3 μW/g.

If the energy source cannot be assumed infinite, another useful metric would be efficiency. The proposed design outputs 0.5 nJ per cycle (1.3 μW at 2.5 kHz) and absorbs 24 nJ. The energy associated with shaking the rest of the mass (one gram) is on the order of 10^{-3} nJ. The efficiency of this device would thus be 2%.

Note that the power necessary to run control and sensing electronics has not been taken into account. Meninger [25] discovered in his design that control electronics imposed an energy tax of roughly half the energy produced. This would decrease the efficiency to 1% and the power densities to 0.43 μW/cm^3 and 0.65 μW/g, respectively. Furthermore, the energy tax imposed by the power electronics scales with voltage, but the energy tax imposed by the control electronics is fixed, since they operate at a low voltage regardless of the voltages inside the power electronics.

Note that these efficiencies are heavily dependent on the power electronics used. In the previous section it is found that decreasing the MOSFET capacitance from 10 pF to 1 pF increases the power output to 33 μW, which corresponds to an energy output of 13 nJ at 2.5 kHz, and an efficiency of 54%. The associated power densities increase to 8.7 μW/cm^3 and 33 μW/g, without taking into account the control and sensing electronics losses.

In all the analyses so far, the limiting factor is the power electronics. Even with power electronics which provide 100% efficiency the power output is limited by the power input from the vibration source. Equation 4.12 states that the power provided by the energy conversion is limited by the energy absorbed into the system. The maximum power output achievable, in the presence of no mechanical or electric losses is $\frac{1}{2}M\omega aX$. Note that the energy required to shake the package, by design, is inconsenquential compared to the energy required to shake the shuttle mass inside. Thus, the total mass of the system effectively scales with the mass of the shuttle itself. The maximum power per mass is bounded to $\frac{1}{2}\omega aX$, or 308 μW/g in the proposed design.

The limit imposed by Equation 4.13 applies to all vibration harvesters, regardless of the technology used to implement the conversion. It shows that harvesters with larger mass and displacement will produce more power than smaller ones. Thus, use of small, light harvesters

will ultimately be limited to niche applications which can use the small amounts of power they can produce.

The question of the initial charge remains. The device designed in this thesis must be externally charged initially, and as long as the vibration source exists it should function indefinitely.

If the vibration source stops or is intermittent, the device and its associated load will reduce the charge in the capacitor. If the charge falls below a certain level, the system will no longer operate, and it will lose its remaining energy. If this is unacceptable, a way to maintain the charge should be devised. The simplest solution is to increase the size of the reservoir. The more charge it can hold, the longer it can survive without energy input. A larger reservoir will add to the total weight and size of the system.

Alternatively, an external source or energy, such as a chemical battery, could be used to restart the system. This might defeat the initial benefit of not having dangerous chemicals in a specific environment. However, it does provide a larger effective reservoir, especially if the system can recharge the external battery when there is an energy surplus. Such a system needs a higher level control and power electronics to deal with the transfer of energy to and from the external energy source, which will add complexity to overall design and decrease its reliability.

Even if the chemical battery is allowed to exist, the system described here could extend the lifetime of the battery by several orders of magnitude, depending on the amount of time it can power the load without tapping into the battery energy.

In order to minimize the mechanical loss, Chapter 4 concluded that these variable capacitors must be operated in vacuum. Packaging the structures designed in Chapter 6 in vacuum is hard. The structures used as variable capacitors have a very large surface area to volume ratio. Other studies have shown than achieving vacuum in this type of structure is difficult to achieve due to outgassing on the walls [20].

8.4 General Conclusions

Vibration-to-electric energy converters will exist in the near future. This thesis proves their feasibility, and provides a complete road map on how to design them.

Although the chosen method in this thesis to create these devices is MEMS fabrication, there is nothing that requires the use of this technology. Other technologies such as LIGA, SU-8 and precision machinery can be used. The design criteria still applies. Also, the devices considered here have a size of a few centimeters. Larger and smaller devices will obey the same principles, although they will present different challenges. Smaller device will have to deal with problems coupling to external vibrations, such as sufficient mass and long travel. Larger devices will have to ensure large enough capacitance changes by minimizing gaps over large areas.

Amirtharajah [3] shows that 170 nW is enough to make useful computations using very-low-power (VLP) technology. The power electronics have been analyzed and have proven that the present technology is likely to be enough to create these power levels. Furthermore, the analysis has shown the most important directions where research can improve the performance of the conversion cycle and relieve the constraints on the electromechanical device. Specifically, the use of integrated circuits, where the MOSFET output capacitance can be tailored, can have a major impact in the power output of these devices.

The simulation of the power electronics has been proven to be an accurate description of the real performance of the power electronics. Note, however, that these equations are very stiff, and care must be taken when solving them. Incorrect or inefficient numerical solvers can easily hang up, take large amounts of time, and return inaccurate or incorrect results.

The mechanical losses have been shown to be comparable, and maybe even larger than the energy converted electrostatically. These losses must be kept at a minimum in order to avoid undesirable restrictions on the design of the variable capacitor. Thus, in order to minimize these losses, these devices must likely be operated in strong vacuums [30].

Analysis of vibration sources has not only shown that they provide the necessary levels of vibration and the frequencies at which they exist, but also points out which details of the vibration spectra are useful for this application.

As a method to create this type of device, fabrication technology has its advantages and disadvantages. The existing body of knowledge from VLSI fabrication provides a useful starting point on how to use this technology to create mechanical devices. Current research is rapidly expanding the array of tools to create more complex devices, such as the use of new materials, multi-wafer bonding and DRIE [12]. It is also a technology amenable to integration of electronics within the device itself since they share the same fabrication process.

This thesis pushes the requirements of fabrication in the areas of DRIE. The state-of-the-art in aspect ratio of features is about 30:1. As this ratio is further improved, and the variations within vertical wall are reduced, better devices can be built for this application. Furthermore, better wall quality will improve the strength of the suspension, allowing the creation of beams and flexure springs which can withstand higher internal stresses.

The fabrication process developed here provides some useful solutions to known problems. The design of a fully connected device, where the mechanical isolation occurs after the critical etch has several advantages. Etch after bonding leads to pressure differentials across the wafer that bow the etch surfaces and might break the bond or structure itself. Furthermore, planar surfaces allow high-quality lithography. The use of anodic bonding and the protection of the bonding surfaces throughout processing leads to easy bonding [23, 28, 29]. Silicon to silicon fusion bonds used in other applications are far more problematic and the requirements on wafer planarity are more stringent.

Several release mechanisms were tested and the use of break-off tabs has been found to be the most effective, above etch or die saw release [23, 28, 29].

The suspensions presented here provide large travel, minimize shear forces, have extremely high directionality while keeping a footprint much smaller than current suspensions.

While the losses imposed by the power electronics suggest that a charge-constrained conversion cycle might be better, improvements in the power electronics can easily swing the advantage back to a voltage-constrained cycle, or to some hybrid, such as the chatter conversion cycle described in Chapter 2. Better MOSFETs and inductors can reduce the cost associated with transport of charge. Furthermore, different designs which avoid MOSFETs losses by cleverly switching when the voltage across the is zero or nearly zero have been

Source	Power density (μW/cm^3)
Solar (Direct sun)	15,000
Solar (Cloudy day)	150
Solar (Office desk)	6
Vibrations	100
Acoustic noise (75 dB)	0.003
Acoustic noise (100 dB)	0.96
Temperature gradient (10°C)	15
Shoe inserts	330
Batteries (non-rechargeable lithium)	90
Batteries (rechargeable lithium)	15
Hydrocarbon (micro heat engine)	320
Fuel cells (methanol)	220

Table 8.2: Comparison of energy sources [30].

Reference	Power output (μW)	Method
Kymissis and Paradiso [19]	1,800	piezoelectric
Lee et al [22]	680	magnetic
Sterken et al [34]	100	electret (theoretical)
Amirtharajah and Chandrakasan [4]	18	magnetic
This thesis	1.3	electric (theoretical)
Shearwood and Yates [32]	0.3	magnetic
Miyazaki et al [27]	0.120	electric

Table 8.3: Power output from vibration transducers.

described in the literature [1]. Zero-volt-switching (ZVS), or resonant, converters increase the complexity of the power electronics, but could provide a more efficient transport of energy.

Table 8.2 compares the power density of different sources of energy [30]. It is also valuable to compare vibration energy harvesters that use different method of transduction, such as variable capacitance [27], moving electrets [34], moving magnets [32, 4, 22], variable inductance (none in the literature) and piezoelectrics [19]. Table 8.3 summarizes the power output from different vibration energy harvesters in the literature. Note that all harvesters are constrained by Equation 4.12. In order to extract energy from vibration, all have requirements placed on their mass and displacement. Compatibility with fabrication favors electric transduction, but higher masses can be achieved using magnetic materials.

8.5 Future Work

The method of electrostatic conversion described in this thesis uses structural variations in a charged capacitor to change its energy content. During the development of the experimental device, one of the techniques tried to avoid the shorting of the two plates was to cover one plate with Mylar® tape. If the structure was shaken, the capacitor voltage changed with no charge in it. In order to prove the model proposed, this was not acceptable. However, it does suggest a different method to generate energy.

The reason a changing voltage was observed is due to the fact that the tape is not electrically neutral. By itself, a layer of charge will not produce energy. But if this layer is moved with respect to another terminal, the change in electric field will change the voltage between the layer and the other terminal. This method of producing energy is analogous to moving a magnet inside a coil, where the changing magnetic field induces currents in the coil. The changes in voltage observed were even larger than those produced by the change in capacitance. This method of conversion should be developed as a fundamentally new method of converting vibration into electric energy.

The method of sensing and controlling the power electronics needs to be designed and studied. A simple way of sensing is to leave a part of the device (a few fingers in a comb-drive or a section of the area in a variable-gap converter) disconnected from the main power circuit and use it independently as a capacitance sensor. Another method would to observe the voltage waveform across the active device. Both these method have the danger of affecting adversely the power circuit by draining useful energy. Furthermore, amplifiers are too costly in terms of energy and are likely not advisable. Creating a low-energy sensor and control electronics remains a challenge associated with this device.

A clever way of controlling the power electronics is to observe the level of the energy returned after each cycle and change the timing parameters to maximize the observed output using adaptive control. It is not clear whether this method would work, although Meninger [25] has done some preliminary work in this direction.

Further attempts to create a comb-drive capable of producing sufficient change in capacitance are also needed. If the method of choice for creating this device is still fabrication

technology, this represents pushing the envelope in large-aspect-ratio etching, as well as addressing the other concerns of stiction, thermal conduction and wafer processing.

A simpler development of this project would be to adapt current valve technology [43] to create a device as the one described in this thesis.

More clever power electronics, such as zero-volt-switching (ZVS), and less lossy components should be studied to minimize the losses in transporting energy to and from the active device.

Recall that the Q of the resonant system is 250,000. This implies that the resonant peak is very narrow. If the source vibration energy is not located at exactly this frequency, the power output will decrease drastically. Reducing the Q is not a good option since it brings the output power down with it. Thus, in situations where the either the resonant frequency of the spring-mass system or the frequency of the vibration source may drift, it is crucial to provide some form of active tuning of the resonant system. For instance, part of the variable capacitor may be used to change the effective spring constant of the spring-mass system. Alternatively, the variable capacitor itself could be excited with a bias voltage that electromechanically tunes the effective spring constant, and hence the resonant frequency, of the energy harvester.

Appendix A

Voltage-Force Relationship

The energy conversion cycles described in Chapter 2 convert mechanical energy into electrical energy [41]. The gain of electric energy results from the force of electric origin which opposes the motion changing the geometry of the capacitor and lowering its capacitance. The integral of this force over the motion distance is equal to the mechanical power converted. This appendix employs energy arguments to derive the relationship between the force and the capacitance of the system, and derives expressions for this force in a constant-gap and variable-gap capacitor.

In order to derive the relationship between stored energy and force, consider a lossless electromechanical transducer with stored electrical energy W, as shown in Figure A-1. Conservation of energy for this transducer states that

$$\frac{dW}{dt} = vi - fu \tag{A.1}$$

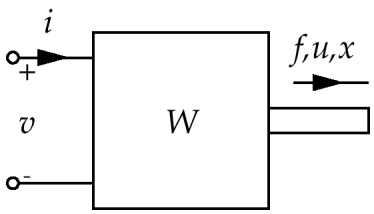

Figure A-1: Electromechanical transducer; f is the force of electric origin acting in the direction of positive velocity u and displacement x.

where f is the force of electric origin acting in the direction of positive u. The transducer developed in Chapter 1 is an electroquasistatic system (EQS), where $i = \frac{dq}{dt}$. With this definition, Equation A.1 may be rewritten as

$$\frac{dW}{dt} = v\frac{dq}{dt} - f\frac{dx}{dt} \tag{A.2}$$

where x is the displacement caused by u. In differential form

$$dW = vdq - fdx \tag{A.3}$$

Since W is a conservative state function that is determined by q and x, that is, since $W = f(q, x)$, then

$$dW = \left.\frac{\partial W}{\partial q}\right|_x dq + \left.\frac{\partial W}{\partial x}\right|_q dx \tag{A.4}$$

where the subscript indicates the variable that is held constant. Since Equations A.3 and A.4 must hold for all independent values of q and x, it follows that

$$v = \left.\frac{\partial W}{\partial q}\right|_x \tag{A.5}$$

$$f = -\left.\frac{\partial W}{\partial x}\right|_q \tag{A.6}$$

In order to compute the energy dW in the transducer, integrate W in the q, x plane first along the x axis from $x = 0$, $q = 0$ and then perpendicular to it to x, q. Since, by assumption, the transducer does not store mechanical energy, all forces must be of electrical origin. Further, it is assumed that if $q = 0$ then $f = 0$, since this derivation considers only electric energy transduction. This assumption precludes permanent electrets. Thus, the integral may be computed as

$$W = \iint_{W(0,0)}^{W(q,x)} dW = \int_{x'=0}^{x'=x} -f|_{q'=0}dx' + \int_{q'=0}^{q'=q} v|_{x'=x}dq' \tag{A.7}$$

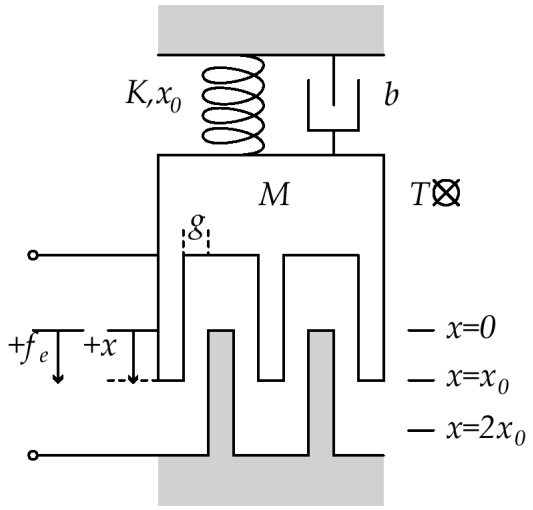

Figure A-2: Electromechanical model of the constant-gap energy harvester.

The first integral is zero since $f(q'=0)=0$. For the second integral, recall that $v = q/C(x)$. Thus,

$$W = \int_{q'=0}^{q'=q} \left.\frac{q}{C(x')}\right|_{x'=x} dq' = \frac{1}{2}\frac{q^2}{C(x)} \tag{A.8}$$

The energy stored in an electrically linear capacitor is $W = \frac{1}{2}\frac{q^2}{C(x)}$. Therefore, the electrical force is

$$f = \frac{1}{2}\frac{q^2}{C(x)^2}\frac{dC}{dx} = \frac{1}{2}v^2\frac{dC}{dx} \tag{A.9}$$

In a constant-gap energy harvester, shown in Figure A-2

$$C = \frac{\epsilon_0 T n x}{g} \tag{A.10}$$

where T is the structure thickness, g is the gap between the fingers, x is the overlapping distance of the fingers, and n is the number of gaps in the comb. Applying Equation A.9, the force exerted on the shuttle by the electrostatic field is

$$f = \frac{1}{2}\frac{\epsilon_0 T n}{g}v^2 \tag{A.11}$$

In a variable-gap energy harvester, shown in Figure A-3

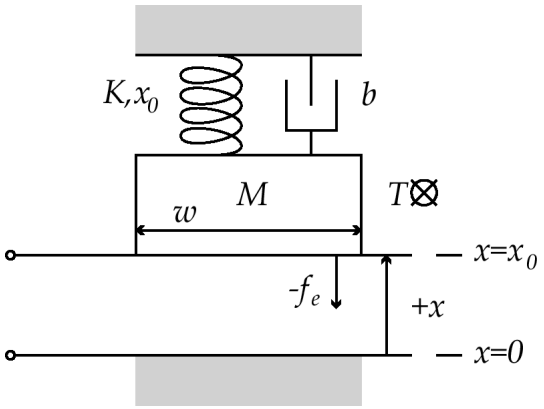

Figure A-3: Electromechanical model of the variable-gap energy harvester.

$$C = \frac{\epsilon_0 TW}{x} \tag{A.12}$$

where T is the device thickness, W is the width of the capacitor, and x is the distance across the gap. Applying Equation A.9, the expression for the electrostatic force is

$$f = -\frac{1}{2}\frac{\epsilon_0 TW}{x^2}v^2 \tag{A.13}$$

Appendix B

MATLAB Power Electronics Model

The circuit to be analyzed, shown in Figure 3-5, is shown again for convenience in Figure B-1. It is a model of the test circuit implementation of the charge-constrained cycle shown in Figure 3-3. This Appendix derives a set of state equation which will be used to numerically simulate the circuit using the MATLAB® program in Appendix C. The numerical values of all the variables used here are given in the text of Chapter 3, as well as below every figure in Chapter 3 which presents a simulation result. The state vector of the model will consist of $[i_L\ v_{F2}\ v_R\ v_{F1}]$. Note that it is not necessary to introduce v_M as a state because it can be determined from v_R, v_{F1} and v_{F2}. The switches will be assumed to be closed for the derivation of the state equations. The first state equation, for $\frac{d}{dt}i_L$, is obtained using KVL through nodes e_1, e_2 and e_3. The result is

$$v_R = L\frac{d}{dt}i_L + R_L i_{LT} + v_{F1} \tag{B.1}$$

Note that the current through R_L, i_{LT}, is

$$i_{LT} = i_L + \frac{L}{R_C}\frac{d}{dt}i_L \tag{B.2}$$

Combining Equations B.1 and B.2, the equation for i_L is

$$\frac{d}{dt}i_L = -\frac{R_C R_L}{R_C + R_L}\frac{1}{L}i_L + \frac{R_C}{R_C + R_L}\frac{1}{L}(v_R - v_{F1}) \tag{B.3}$$

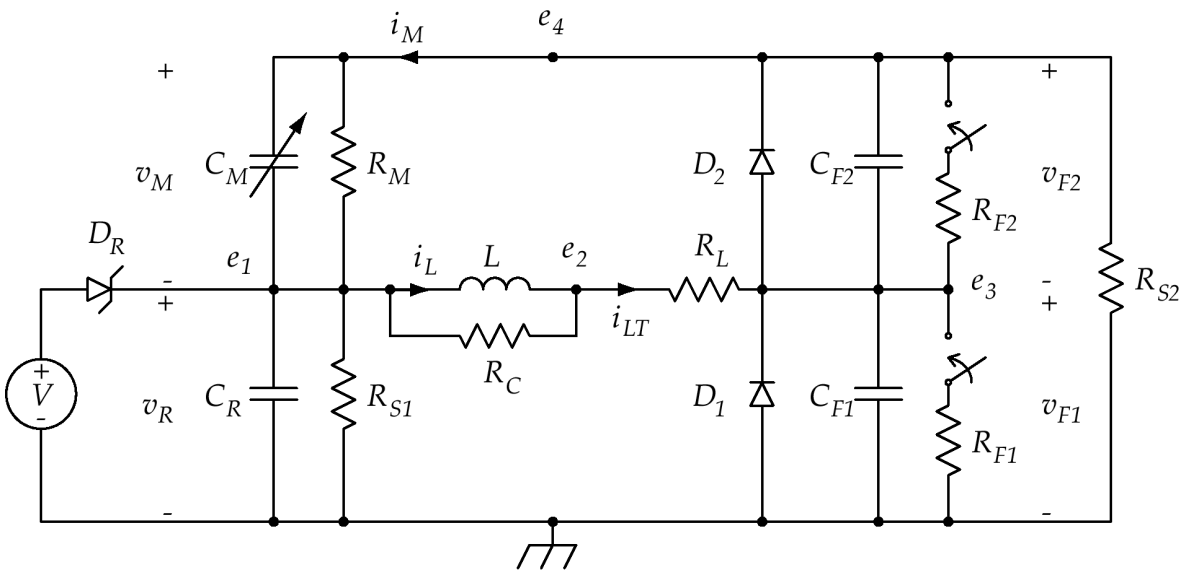

Figure B-1: MATLAB® model of the power electronics circuit.

Furthermore, i_{LT} can now be expressed in terms of state variables only as

$$i_{LT} = \frac{R_C}{R_C + R_L} i_L + \frac{v_R - v_{F1}}{R_C + R_L} \tag{B.4}$$

The second state equation, for $\frac{d}{dt} v_{F2}$, is obtained from a set of three equations. The time-varying capacitor C_M and R_M yield

$$i_M = C_M \frac{d}{dt} v_M + \frac{d}{dt} C_M v_M + \frac{v_M}{R_M} \tag{B.5}$$

Next, v_M can be expressed in terms of the other capacitor voltages as

$$v_M = v_{F1} + v_{F2} - v_R \tag{B.6}$$

and i_M can be expressed as the current through D_2, C_{F2}, R_{F2} and R_{S2} as

$$i_M = -C_{F2} \frac{d}{dt} v_{F2} - \frac{v_{F2}}{R_{F2}} + I_2 \left(e^{-\frac{v_{F2}}{v_T}} - 1 \right) - \frac{1}{R_{S2}} (v_{F1} + v_{F2}) \tag{B.7}$$

Combining Equations B.5, B.6 and B.7 yields

$$C_M \frac{d}{dt}(v_{F1} + v_{F2} - v_R) + \frac{d}{dt} C_M (v_{F1} + v_{F2} - v_R) + \frac{v_{F1} + v_{F2} - v_R}{R_M} + C_{F2} \frac{d}{dt} v_{F2} + \frac{v_{F2}}{R_{F2}} - I_2 \Big(e^{-\frac{v_{F2}}{v_T}} - 1 \Big) + \frac{1}{R_{S2}} (v_{F1} + v_{F2}) = 0 \tag{B.8}$$

which still involves derivatives of v_R and v_{F1}. These expressions will be derived in the next two equations and the final expression for v_{F2} will then be computed through back-substitution. The third state equation, for $\frac{d}{dt} v_R$, can be obtained from KCL at node e_1. Substituting the currents through D_2, C_{F2}, R_{F2} and R_{S2} for i_M and the expression for i_{LT} yields

$$\frac{d}{dt} v_R = - \frac{R_C}{R_C + R_L} \frac{1}{C_R} i_L - \frac{v_R - v_{F1}}{(R_C + R_L) C_R} - \frac{1}{R_{S1} C_R} v_R - \frac{1}{R_{F2} C_R} v_{F2} - \frac{v_{F1} + v_{F2}}{R_{S2} C_R} + \frac{1}{C_R} I_2 \Big(e^{-\frac{v_{F2}}{v_T}} - 1 \Big) + \frac{1}{C_R} I_R \Big(e^{\frac{V - v_R}{v_T}} - 1 \Big) - \frac{C_{F2}}{C_R} \frac{d}{dt} v_{F2} \tag{B.9}$$

The fourth and final state equation, for $\frac{d}{dt} v_{F1}$, can be obtained from KCL at e_3. Substitution for i_{LT} yields

$$\frac{d}{dt} v_{F1} = \frac{R_C}{R_C + R_L} \frac{1}{C_{F1}} i_L + \frac{v_R - v_{F1}}{(R_C + R_L) C_{F1}} + \frac{1}{R_{F2} C_{F1}} v_{F2} - \frac{1}{R_{F1} C_{F1}} v_{F1} + \frac{1}{C_{F1}} I_1 \Big(e^{-\frac{v_{F1}}{v_T}} - 1 \Big) - \frac{1}{C_{F1}} I_2 \Big(e^{-\frac{v_{F2}}{v_T}} - 1 \Big) + \frac{C_{F2}}{C_{F1}} \frac{d}{dt} v_{F2} \tag{B.10}$$

The Equations for $\frac{d}{dt} v_R$, Equation B.9, and $\frac{d}{dt} v_{F1}$, Equation B.10, only depend on state variables and $\frac{d}{dt} v_{F2}$. Substituting these two Equations, B.9 and B.10, into Equation B.8

yields

$$
\begin{aligned}
Q\frac{d}{dt}v_{F2} = &-\frac{1}{R_{F2}}v_{F2} - \frac{v_{F1}+v_{F2}}{R_{S2}} - \frac{1}{R_M}(v_{F1}+v_{F2}-v_R) + I_2\Big(e^{-\frac{v_{F2}}{v_T}}-1\Big) \\
&- \frac{d}{dt}C_M(v_{F1}+v_{F2}-v_R) \\
&+ \Bigg[-\frac{R_C}{R_C+R_L}\Big(\frac{1}{C_R}+\frac{1}{C_{F1}}\Big)i_L - \Big(\frac{1}{C_R}+\frac{1}{C_{F1}}\Big)\frac{1}{R_{F2}}v_{F2} - \frac{v_{F1}+v_{F2}}{R_{S2}C_R} \\
&+ \frac{1}{R_{F1}C_{F1}}v_{F1} - \Big(\frac{1}{C_R}+\frac{1}{C_{F1}}\Big)\frac{v_R-v_{F1}}{R_C+R_L} - \frac{1}{R_{S1}C_R}v_R \\
&- \frac{1}{C_{F1}}I_1\Big(e^{-\frac{v_{F1}}{v_T}}-1\Big) + \Big(\frac{1}{C_R}+\frac{1}{C_{F1}}\Big)I_2\Big(e^{-\frac{v_{F2}}{v_T}}-1\Big) + \frac{1}{C_R}I_R\Big(e^{\frac{V-v_R}{v_T}}-1\Big)\Bigg]C_M
\end{aligned}
\tag{B.11}
$$

which depends only on state variables and where

$$
Q = C_{F2} + \Bigg[1 + C_{F2}\Big(\frac{1}{C_R}+\frac{1}{C_{F1}}\Big)\Bigg]C_M \tag{B.12}
$$

Back-substitution of the Equation for $\frac{d}{dt}v_{F2}$, Equation B.11, into the Equations for $\frac{d}{dt}v_R$, Equation B.9, and $\frac{d}{dt}v_{F1}$, Equation B.10, can yield explicit state equations, but, in the interest of minimizing computation time, it is better to compute $\frac{d}{dt}v_{F2}$ once and use this result in the computation of $\frac{d}{dt}v_R$ and $\frac{d}{dt}v_{F1}$. The variable capacitance $C_M(t)$ will be modeled as:

$$
C_M(t) = \frac{\Delta C}{2}\cos(\omega t - \alpha) + \frac{\Delta C}{2} + C_{min} \tag{B.13}
$$

where C_M oscillates between $C_{min}+\Delta C$ and C_{min} and ω and α represent the frequency and phase of the shaking. From this expression,

$$
\frac{d}{dt}C_M(t) = -\frac{\Delta C}{2}\omega\sin(\omega t - \alpha) \tag{B.14}
$$

Segment	F1	F2	C_{MEMS}	Description
1	Open	Open	$C_{min} \rightarrow C_{min} + \Delta C$	Rest
2	Closed	Open	$C_{min} + \Delta C$	Charging
3	Open	Open	$C_{min} + \Delta C \rightarrow C_{min}$	Transduction
4	Open	Closed	C_{min}	Discharging
5	Open	Open	$C_{min} \rightarrow C_{min} + \Delta C$	Rest

Table B.1: A full simulated non-synchronous conversion cycle consisting of separate sequential cycle segments in accordance with the MOSFET states.

The complete set of state equations is

$$\frac{d}{dt}di_L = -\frac{R_C R_L}{R_C + R_L}\frac{1}{L}i_L + \frac{R_C}{R_C + R_L}\frac{1}{L}(v_R - v_{F1}) \tag{B.15}$$

$$\begin{aligned}\frac{d}{dt}v_{F2} =& \Bigg\{ -\frac{1}{R_{F2}}v_{F2} - \frac{v_{F1} + v_{F2}}{R_{S2}} - \frac{1}{R_M}(v_{F1} + v_{F2} - v_R) + I_2\Big(e^{-\frac{v_{F2}}{v_T}} - 1\Big) \\ & - \frac{d}{dt}C_M(v_{F1} + v_{F2} - v_R) \\ & + \Bigg[-\frac{R_C}{R_C + R_L}\Big(\frac{1}{C_R} + \frac{1}{C_{F1}}\Big)i_L - \Big(\frac{1}{C_R} + \frac{1}{C_{F1}}\Big)\frac{1}{R_{F2}}v_{F2} - \frac{v_{F1} + v_{F2}}{R_{S2}C_R} \\ & + \frac{1}{R_{F1}C_{F1}}v_{F1} - \Big(\frac{1}{C_R} + \frac{1}{C_{F1}}\Big)\frac{v_R - v_{F1}}{R_C + R_L} - \frac{1}{R_{S1}C_R}v_R \\ & - \frac{1}{C_{F1}}I_1\Big(e^{-\frac{v_{F1}}{v_T}} - 1\Big) + \Big(\frac{1}{C_R} + \frac{1}{C_{F1}}\Big)I_2\Big(e^{-\frac{v_{F2}}{v_T}} - 1\Big) + \frac{1}{C_R}I_R\Big(e^{\frac{V - v_R}{v_T}} - 1\Big)\Bigg] C_M \Bigg\}\frac{1}{Q}\end{aligned} \tag{B.16}$$

$$\begin{aligned}\frac{d}{dt}v_R =& -\frac{R_C}{R_C + R_L}\frac{1}{C_R}i_L - \frac{v_R - v_{F1}}{(R_C + R_L)C_R} - \frac{1}{R_{S1}C_R}v_R - \frac{1}{R_{F2}C_R}v_{F2} - \frac{v_{F1} + v_{F2}}{R_{S2}C_R} \\ & + \frac{1}{C_R}I_2\Big(e^{-\frac{v_{F2}}{v_T}} - 1\Big) + \frac{1}{C_R}I_R\Big(e^{\frac{V - v_R}{v_T}} - 1\Big) - \frac{C_{F2}}{C_R}\frac{d}{dt}v_{F2}\end{aligned} \tag{B.17}$$

$$\begin{aligned}\frac{d}{dt}v_{F1} =& \frac{R_C}{R_C + R_L}\frac{1}{C_{F1}}i_L + \frac{v_R - v_{F1}}{(R_C + R_L)C_{F1}} + \frac{1}{R_{F2}C_{F1}}v_{F2} - \frac{1}{R_{F1}C_{F1}}v_{F1} \\ & + \frac{1}{C_{F1}}I_1\Big(e^{-\frac{v_{F1}}{v_T}} - 1\Big) - \frac{1}{C_{F1}}I_2\Big(e^{-\frac{v_{F2}}{v_T}} - 1\Big) + \frac{C_{F2}}{C_{F1}}\frac{d}{dt}v_{F2}\end{aligned} \tag{B.18}$$

For the cycle segments in which the MOSFET switch F1 or F2 is open, $R_{F1} \rightarrow \infty$ or $R_{F2} \rightarrow \infty$, accordingly. Thus, the appropriate terms that are divided by R_{F1} or R_{F2} will vanish. A full simulated conversion cycle will consist of separate sequential cycle segments in accordance with the MOSFET states. These segments are shown in Table B.1. To simulate

Segment	F1	F2	C_{MEMS}	Description
1	Open	Open	$C_{min} \rightarrow C_{min} + \Delta C$	Rest
2	Closed	Open	$C_{min} + \Delta C$	Charging Inductor
3	Open	Closed	$C_{min} + \Delta C$	Charging C_M
4	Open	Open	$C_{min} + \Delta C \rightarrow C_{min}$	Transduction
5	Open	Closed	C_{min}	Discharging C_M
6	Closed	Open	C_{min}	Discharging Inductor
7	Open	Open	$C_{min} \rightarrow C_{min} + \Delta C$	Rest

Table B.2: A full simulated synchronous conversion cycle consisting of separate sequential cycle segments in accordance with the MOSFET states.

synchronous switching with lateral MOSFETs (i.e., MOSFETs without parasitic diodes), the MOSFET diodes are turned off by setting I_1 and I_2 to zero and changing the order of the time stages in accordance with the MOSFET states as shown in Table B.2.

Appendix C

MATLAB Programs

The five program listed below simulate the equations obtained in Appendix B. The first program, *powerelectronicsdiodes.m* is the main program called inside MATLAB® by the user which implements a non-synchronous rectification where the MOSFETs are turned on only when the current flows from drain to source. The MOSFET diodes carry the current in the opposite direction. The second program, *powerelectronicsdiodesfun.m* calculates the derivatives of the state variables in *powerelectronicsdiodes.m* and is used to compute these derivatives directly, as well as by the High-Order Runge-Kutta stiff integrator ODE15s. The third program, *powerelectronicssynch.m* is the main program called inside MATLAB® by the user which implements synchronous rectification where the MOSFET are turned on every time the current flows through them. The MOSFETs in this simulation do not have diodes. The fourth program, *powerelectronicssynchfun.m* calculates the derivatives of the state variables in *powerelectronicssynch.m* and is used to compute these derivatives directly, as well as by the High-Order Runge-Kutta stiff integrator ODE15s. The fifth program, *integrate.m*, performs a trapezoidal integration of a numerical series x as a function of t. In all the programs except *integrate.m*, the state vector x is the state vector $[i_L\ v_{F2}\ v_R\ v_{F1}]$, such that x(:,1) is i_L, and xdot(:,1) is $\frac{d}{dt}i_L$.

C.1 *powerelectronicsdiodes.m*

This program is called directly within MATLAB®, and returns graphically the results of a simulation. The graphics include the state variables of the simulation, the simulated oscilloscope traces, and the energy absorbed and returned by each element. It also loads the measured oscilloscope traces from the test circuit and superimposes them with the simulated traces for comparison. Finally, it lists the energies of all the elements after one energy conversion cycle.

The first section lists the global variables shared with the state derivative function *powerelectronicsdiodesfun.m*. The next section defines the values for all the elements in the model. The third section defines the time intervals where the MOSFETs are on or off. This is a manual process, and a better implementation could find these breakpoints automatically, specially since correct timing values are critical to the operation of the simulated power electronics. The next few sections define the global variables to be shared with *powerelectronicsdiodesfun.m* in order to minimize the computational burden every time *powerelectronicsdiodesfun.m* is called within ODE15s.

The next sections call sequentially ODE15s using the previous call as the initial condition for next one. Each section stores both the state variables and its derivatives. As a matter of convenience, each section also displays the amount of time it takes to run in the main window. The next section used the state variable and its derivatives to compute the instantaneous power of each element. These powers are then integrated to find the energies absorbed, return and/or dissipated by each element. The next three sections create the resulting plots and save each plot to a graphical file. The last section finds manually the energies after one cycle and returns these values to the main window.

The equations solved by this simulation are very stiff; the time constant for the discharging of the MOSFET output capacitance when it closes is in the order of 10^{-10} seconds. The stiffness of the equations makes it essential to use a stiff differential equation solver. Furthermore, ODE15s, the high-order method, returns values that are noticeably different from using a low-order stiff solver.

```
clear

global qa qb cma Ac omega alpha As
global I1 d1 I2 d2 Ir dr Ivr
global xd1lx1 xd1lx3mx4
global xd2lx2a xd2lx2x4a xd2lx2mx3x4 xd2lx1 xd2lx2b xd2lx2x4b
global xd2lx3 xd2lx3mx4 xd2lx4 xd2li1 xd2li2 xd2lir
global xd3lx1 xd3lx2 xd3lx2x4 xd3lx3 xd3lx3mx4 xd3li2 xd3lir xd3lxd2
global xd4lx1 xd4lx2 xd4lx3mx4 xd4lx4 xd4li1 xd4li2 xd4lxd2

cr=3e-9;
l=2.5e-3;
rl=8;
rc=2e5;%360e3@300khz
cf1=95e-12;
rf1=1.5;
cf2=cf1;
rf2=rf1;
cmin=450e-12;
%530pF@000mVpp
%480pF@200mVpp
%450pF@400mVpp
deltac=160e-12;
%100pF@200mVpp
%160pF@400mVpp
rm=10e6;%10e6
I1=1e-30;%1e-8 best
vt1=26e-3;
I2=I1;
vt2=vt1;
Ir=1e-14;
vtr=vt1;
V=1.24;
rs1=10e6;
rs2=10e6;
f=3.8e3;
duty=.62;
tc=19.4e-6;
td=6.2e-6;
alpha=-pi/2;

%xinit=[iL vF2 vR vF1];
%vF1 should be vR after a long time,
%vMEMS=vF2+vF1-vR;
%if vF1=vR => vF2=vMEMS
```

```
load laststate.mat -ascii
xinit=laststate;
tp(1)=(1-duty)/2*1/f;
tp(2)=tc;%tc;
%transduction
tp(3)=duty*1/f-tc;%1/(2*f)-tc;
tp(4)=td;%td;
tp(5)=(1-duty)*1/f-td;%1/(2*f)-td;
tp(6)=tc;%tc;
%transduction
tp(7)=duty*1/f-tc;%1/(2*f)-tc;
tp(8)=td;%td;
tp(9)=(1-duty)*1/f-td;%1/(2*f)-td;
tp(10)=tc;%tc;
%transduction
tp(11)=duty*1/f-tc;%1/(2*f)-tc;
tp(12)=td;%td;
tp(13)=(1-duty)/2*1/f-td;%1/(2*f)-td;

%global variables
qa=cf2;
qb=1+cf2*(1/cr+1/cf1);

cma=cmin+deltac/2;
Ac=deltac/2;
omega=2*pi*f;
As=-deltac/2*omega;

d1=exp(-1/vt1);
d2=exp(-1/vt2);
Ivr=Ir*exp(V/vtr);
dr=exp(-1/vtr);

xd1lx1=-rc*rl/((rc+rl)*l);
xd1lx3mx4=rc/((rc+rl)*l);

xd2lx2aclosed=-1/rf2;%0 when F2 open
xd2lx2x4a=-1/rs2;
xd2lx2mx3x4=-1/rm;
xd2lx1=-rc/(rc+rl)*(1/cr+1/cf1);
xd2lx2bclosed=-(1/cr+1/cf1)/rf2;%0 when F2 open
xd2lx2x4b=-1/(rs2*cr);
xd2lx3=-1/(rs1*cr);
xd2lx3mx4=-1/(rc+rl)*(1/cr+1/cf1);
xd2lx4closed=1/(rf1*cf1);%0 when F1 open
```

```
xd2li1=-1/cf1;
xd2li2=(1/cr+1/cf1);
xd2lir=1/cr;

xd3lx1=-rc/(rc+rl)/cr;
xd3lx2closed=-1/(rf2*cr);%0 when F2 open
xd3lx2x4=-1/(rs2*cr);
xd3lx3=-1/(rs1*cr);
xd3lx3mx4=-1/((rc+rl)*cr);
xd3li2=1/cr;
xd3lir=1/cr;
xd3lxd2=-cf2/cr;

xd4lx1=rc/(rc+rl)/cf1;
xd4lx2closed=1/(rf2*cf1);%0 when F2 open
xd4lx3mx4=1/((rc+rl)*cf1);
xd4lx4closed=-1/(rf1*cf1);%0 when F1 open
xd4li1=1/cf1;
xd4li2=-1/cf1;
xd4lxd2=cf2/cf1;

%stage1
disp('stage1')
%F1 open
xd2lx4=0;
xd4lx4=0;
%F2 open
xd2lx2a=0;
xd2lx2b=0;
xd3lx2=0;
xd4lx2=0;
tic
[t1,x1]=ode15s('powerelectronicsdiodesfun',...
   [0 tp(1)],xinit);
disp(num2str(toc))
x1dot=powerelectronicsdiodesfun(t1,x1')';

%charging
%stage2
disp('stage2')
%F1 closed
xd2lx4=xd2lx4closed;
xd4lx4=xd4lx4closed;
%F2 open
xd2lx2a=0;
```

```
xd2lx2b=0;
xd3lx2=0;
xd4lx2=0;
tic
[t2,x2]=ode15s('powerelectronicsdiodesfun',...
   [sum(tp(1:1)) sum(tp(1:2))],x1(end,:));
disp(num2str(toc))
x2dot=powerelectronicsdiodesfun(t2,x2')';

%transduction
%stage3
disp('stage3')
%F1 open
xd2lx4=0;
xd4lx4=0;
%F2 open
xd2lx2a=0;
xd2lx2b=0;
xd3lx2=0;
xd4lx2=0;
tic
[t3,x3]=ode15s('powerelectronicsdiodesfun',...
   [sum(tp(1:2)) sum(tp(1:3))],x2(end,:));
disp(num2str(toc))
x3dot=powerelectronicsdiodesfun(t3,x3')';

%discharging
%stage4
disp('stage4')
%F1 open
xd2lx4=0;
xd4lx4=0;
%F2 closed
xd2lx2a=xd2lx2aclosed;
xd2lx2b=xd2lx2bclosed;
xd3lx2=xd3lx2closed;
xd4lx2=xd4lx2closed;
tic
[t4,x4]=ode15s('powerelectronicsdiodesfun',...
   [sum(tp(1:3)) sum(tp(1:4))],x3(end,:));
disp(num2str(toc))
x4dot=powerelectronicsdiodesfun(t4,x4')';

%stage5
disp('stage5')
```

```
%F1 open
xd2lx4=0;
xd4lx4=0;
%F2 open
xd2lx2a=0;
xd2lx2b=0;
xd3lx2=0;
xd4lx2=0;
tic
[t5,x5]=ode15s('powerelectronicsdiodesfun',...
   [sum(tp(1:4)) sum(tp(1:5))],x4(end,:));
disp(num2str(toc))
x5dot=powerelectronicsdiodesfun(t5,x5')';

%charging
%stage6
disp('stage6')
%F1 closed
xd2lx4=xd2lx4closed;
xd4lx4=xd4lx4closed;
%F2 open
xd2lx2a=0;
xd2lx2b=0;
xd3lx2=0;
xd4lx2=0;
tic
[t6,x6]=ode15s('powerelectronicsdiodesfun',...
   [sum(tp(1:5)) sum(tp(1:6))],x5(end,:));
disp(num2str(toc))
x6dot=powerelectronicsdiodesfun(t6,x6')';

%transduction
%stage7
disp('stage7')
%F1 open
xd2lx4=0;
xd4lx4=0;
%F2 open
xd2lx2a=0;
xd2lx2b=0;
xd3lx2=0;
xd4lx2=0;
tic
[t7,x7]=ode15s('powerelectronicsdiodesfun',...
   [sum(tp(1:6)) sum(tp(1:7))],x6(end,:));
```

```
disp(num2str(toc))
x7dot=powerelectronicsdiodesfun(t7,x7')';

%discharging
%stage8
disp('stage8')
%F1 open
xd2lx4=0;
xd4lx4=0;
%F2 closed
xd2lx2a=xd2lx2aclosed;
xd2lx2b=xd2lx2bclosed;
xd3lx2=xd3lx2closed;
xd4lx2=xd4lx2closed;
tic
[t8,x8]=ode15s('powerelectronicsdiodesfun',...
   [sum(tp(1:7)) sum(tp(1:8))],x7(end,:));
disp(num2str(toc))
x8dot=powerelectronicsdiodesfun(t8,x8')';

%stage9
disp('stage9')
%F1 open
xd2lx4=0;
xd4lx4=0;
%F2 open
xd2lx2a=0;
xd2lx2b=0;
xd3lx2=0;
xd4lx2=0;
tic
[t9,x9]=ode15s('powerelectronicsdiodesfun',...
   [sum(tp(1:8)) sum(tp(1:9))],x8(end,:));
disp(num2str(toc))
x9dot=powerelectronicsdiodesfun(t9,x9')';

%charging
%stage10
disp('stage10')
%F1 closed
xd2lx4=xd2lx4closed;
xd4lx4=xd4lx4closed;
%F2 open
xd2lx2a=0;
xd2lx2b=0;
```

```
xd3lx2=0;
xd4lx2=0;
tic
[t10,x10]=ode15s('powerelectronicsdiodesfun',...
    [sum(tp(1:9)) sum(tp(1:10))],x9(end,:));
disp(num2str(toc))
x10dot=powerelectronicsdiodesfun(t10,x10')';

%transduction
%stage11
disp('stage11')
%F1 open
xd2lx4=0;
xd4lx4=0;
%F2 open
xd2lx2a=0;
xd2lx2b=0;
xd3lx2=0;
xd4lx2=0;
tic
[t11,x11]=ode15s('powerelectronicsdiodesfun',...
    [sum(tp(1:10)) sum(tp(1:11))],x10(end,:));
disp(num2str(toc))
x11dot=powerelectronicsdiodesfun(t11,x11')';

%discharging
%stage12
disp('stage12')
%F1 open
xd2lx4=0;
xd4lx4=0;
%F2 closed
xd2lx2a=xd2lx2aclosed;
xd2lx2b=xd2lx2bclosed;
xd3lx2=xd3lx2closed;
xd4lx2=xd4lx2closed;
tic
[t12,x12]=ode15s('powerelectronicsdiodesfun',...
    [sum(tp(1:11)) sum(tp(1:12))],x11(end,:));
disp(num2str(toc))
x12dot=powerelectronicsdiodesfun(t12,x12')';

%stage13
disp('stage13')
%F1 open
```

```
xd2lx4=0;
xd4lx4=0;
%F2 open
xd2lx2a=0;
xd2lx2b=0;
xd3lx2=0;
xd4lx2=0;
tic
[t13,x13]=ode15s('powerelectronicsdiodesfun',...
    [sum(tp(1:12)) sum(tp(1:13))],x12(end,:));
disp(num2str(toc))
x13dot=powerelectronicsdiodesfun(t13,x13')';

t=[t1;t2;t3;t4;t5;t6;t7;t8;t9;t10;t11;t12;t13];
x=[x1;x2;x3;x4;x5;x6;x7;x8;x9;x10;x11;x12;x13];
xdot=[x1dot;x2dot;x3dot;x4dot;x5dot;x6dot;x7dot;...
      x8dot;x9dot;x10dot;x11dot;x12dot;x13dot];
laststate=x(end,:);
save laststate.mat laststate -ascii
beep
disp('Successful integration')
close all

%energy computation
disp('Calculating energies')
il=x(:,1);vf2=x(:,2);vr=x(:,3);vf1=x(:,4);
ildot=xdot(:,1);vf2dot=xdot(:,2);vrdot=xdot(:,3);vf1dot=xdot(:,4);
%source
idr=Ivr*(dr).^vr-Ir;
pdr=-idr.*vr;
edr=integrate(t,pdr,0);
%inductor
ilt=rc/(rc+rl)*il+(vr-vf1)/(rc+rl);
pl=ilt.*(vr-vf1);
el=integrate(t,pl,0);
%reservoir
ir=vr/rs1+cr*vrdot;
pr=vr.*ir;
er=integrate(t,pr,0);
%mems
im=ilt+ir-idr;
vm=vf1+vf2-vr;
pm=im.*vm;
em=integrate(t,pm,0);
%MOSFET1 (bottom)
```

```
if1=ilt-im;
pf1=vf1.*if1;
ef1=integrate(t,pf1,0);
%MOSFET2 (top)
id2=-I2*d2.^vf2+I2;
icf2=cf2*vf2dot;
irf2=-id2-icf2-im;
pf2=-im.*vf2;
ef2=integrate(t,pf2,0);

%plot waveforms
disp('Displaying waveforms')
figure
set(gcf,'Position',[400 35 620 660])
subplot 311
plot(t*1e6,il*1e3)
ylabel('i_L (mA)')
title(strvcat('Power Electronics (State Variables)','(time in \mus)'))
grid on
axis tight
subplot 613
plot(t*1e6,vm)
ylabel('v_{M} (V)')
grid on
axis tight
subplot 614
plot(t*1e6,vr)
ylabel('v_{res} (V)')
grid on
axis tight
subplot 615
plot(t*1e6,vf2)
ylabel('v_{FET2} (V)')
grid on
axis tight
subplot 616
plot(t*1e6,vf1)
ylabel('v_{FET1} (V)')
grid on
axis tight
xlabel(strvcat(['C_{res}=' num2str(cr*1e9) 'nF'...
      '  L=' num2str(l*1e3) 'mH'...
      '  R_L=' num2str(round(rl)) '\Omega'...
      '  R_C=' num2str(rc*1e-3) 'k\Omega'...
      '  C_{FET}=' num2str(cf1*1e12) 'pF'...
```

```
      '  R_{FET}=' num2str(rf1) '\Omega'...
      '  C_{min}=' num2str(cmin*1e12) 'pF'...
      '  \DeltaC=' num2str(round(deltac*1e12)) 'pF'],...
      [ 't_{rest}\approx' num2str(round(tp(5)*1e6)) '\mus'...
      '  t_{charge}=' num2str(tp(6)*1e6) '\mus'...
      '  t_{active}\approx' num2str(round(tp(7)*1e6)) '\mus'...
      '  t_{discharge}=' num2str(tp(8)*1e6) '\mus'...
      '  f=' num2str(f*1e-3) 'kHz'...
      '  duty=' num2str(duty*100) '%']))
print('-dpng',['matlabstate'...
      'Cr' num2str(cr*1e9) 'n'...
      'L'  num2str(l*1e3) 'm'...
      'Rl' num2str(round(rl))...
      'Rc' num2str(round(rc*1e-3)) 'k'...
      'Cf' num2str(cf1*1e12) 'p'...
      'Rf' num2str(rf1)...
      'Cm' num2str(cmin*1e12) 'p'...
      'dC' num2str(round(deltac*1e12)) 'p.png'])

%plot trace
disp('Displaying scope traces')
figure
set(gcf,'Position',[400 35 620 660])
subplot 211
plot(t*1e6,vr+vm)
ylabel('v_{res}+ v_{M} (V)')
title(strvcat('Power Electronics (Scope Traces)','(time in \mus)'))
grid on
axis([0 800 -5 15])
tek=csvread('tek_3.8khz_400mVpp_top.DAT');
hold on
plot(tek(:,1)*1e6+360,tek(:,2),'m')
subplot 212
plot(t*1e6,vr)
ylabel('v_{res} (V)')
grid on
axis([0 800 0 4])
tek=csvread('tek_3.8khz_400mVpp.DAT');
hold on
plot(tek(:,1)*1e6+360,tek(:,2),'m')
xlabel(strvcat(['C_{res}=' num2str(cr*1e9) 'nF'...
      '  L=' num2str(l*1e3) 'mH'...
      '  R_L=' num2str(round(rl)) '\Omega'...
      '  R_C=' num2str(rc*1e-3) 'k\Omega'...
      '  C_{FET}=' num2str(cf1*1e12) 'pF'...
```

```
      '  R_{FET}=' num2str(rf1) '\Omega'...
      '  C_{min}=' num2str(cmin*1e12) 'pF'...
      '  \DeltaC=' num2str(round(deltac*1e12)) 'pF'],...
      [ 't_{rest}\approx' num2str(round(tp(5)*1e6)) '\mus'...
      '  t_{charge}=' num2str(tp(6)*1e6) '\mus'...
      '  t_{active}\approx' num2str(round(tp(7)*1e6)) '\mus'...
      '  t_{discharge}=' num2str(tp(8)*1e6) '\mus'...
      '  f=' num2str(f*1e-3) 'kHz'...
      '  duty=' num2str(duty*100) '%']))
print('-dpng',['matlabscope'...
      'Cr' num2str(cr*1e9) 'n'...
      'L' num2str(l*1e3) 'm'...
      'Rl' num2str(round(rl))...
      'Rc' num2str(round(rc*1e-3)) 'k'...
      'Cf' num2str(cf1*1e12) 'p'...
      'Rf' num2str(rf1)...
      'Cm' num2str(cmin*1e12) 'p'...
      'dC' num2str(round(deltac*1e12)) 'p.png'])

%plot energies
disp('Displaying energies')
figure
set(gcf,'Position',[400 35 620 660])
subplot 611
plot(t(1:end)*1e6,el(1:end)*1e9)
grid on
axis tight
title(strvcat('Power Electronics (Energies)','(time in \mus)'))
ylabel('E_{L} (nJ)')
subplot 612
plot(t(1:end)*1e6,em(1:end)*1e9)
grid on
axis tight
ylabel('E_{M} (nJ)')
subplot 613
plot(t(1:end)*1e6,er(1:end)*1e9)
grid on
axis tight
ylabel('E_{res} (nJ)')
subplot 614
plot(t(1:end)*1e6,edr(1:end)*1e9)
grid on
axis tight
ylabel('E_{source} (nJ)')
subplot 615
```

```
plot(t(1:end)*1e6,ef2(1:end)*1e9)
grid on
axis tight
ylabel('E_{F2} (nJ)')
subplot 616
plot(t(1:end)*1e6,ef1(1:end)*1e9)
grid on
axis tight
ylabel('E_{F1} (nJ)')
xlabel(strvcat(['C_{res}=' num2str(cr*1e9) 'nF'...
      '  L=' num2str(l*1e3) 'mH'...
      '  R_L=' num2str(round(rl)) '\Omega'...
      '  R_C=' num2str(rc*1e-3) 'k\Omega'...
      '  C_{FET}=' num2str(cf1*1e12) 'pF'...
      '  R_{FET}=' num2str(rf1) '\Omega'...
      '  C_{min}=' num2str(cmin*1e12) 'pF'...
      '  \DeltaC=' num2str(round(deltac*1e12)) 'pF'],...
      [ 't_{rest}\approx' num2str(round(tp(5)*1e6)) '\mus'...
      '  t_{charge}=' num2str(tp(6)*1e6) '\mus'...
      '  t_{active}\approx' num2str(round(tp(7)*1e6)) '\mus'...
      '  t_{discharge}=' num2str(tp(8)*1e6) '\mus'...
      '  f=' num2str(f*1e-3) 'kHz'...
      '  duty=' num2str(duty*100) '%']))
print('-dpng',['matlabenergies'...
      'Cr' num2str(cr*1e9) 'n'...
      'L'  num2str(l*1e3) 'm'...
      'Rl' num2str(round(rl))...
      'Rc' num2str(round(rc*1e-3)) 'k'...
      'Cf' num2str(cf1*1e12) 'p'...
      'Rf' num2str(rf1)...
      'Cm' num2str(cmin*1e12) 'p'...
      'dC' num2str(round(deltac*1e12)) 'p.png'])

index=find(t>180e-6&t<220e-6);
index=index(1);
disp(['v_r='num2str(vr(index))])
disp(['Em=' num2str(em(index)*1e9)])
disp(['Er=' num2str(er(index)*1e9)])
disp(['Es=' num2str(edr(index)*1e9)])
disp(['Ps=' num2str(edr(index)*f*1e6)])
disp(['El=' num2str(el(index)*1e9)])
disp(['Ef1=' num2str(ef1(index)*1e9)])
disp(['Ef2=' num2str(ef2(index)*1e9)])
disp(['Ef=' num2str((ef1(index)+ef2(index))*1e9)])
disp(['Elt=' num2str((ef1(index)+ef2(index)+el(index))*1e9)])
```

```
disp('End of File')
```

C.2 *powerelectronicsdiodesfun.m*

This function returns the state derivatives as required by MATLAB®'s ODE solvers. Furthermore, it is also capable of returning a whole vector of state derivatives if the inputs are vectors of time and state variables. It shares most variables with *powerelectronicsdiodes.m* to minimize the amount of computation it must do every time it is called. This drastically minimizes the amount of time the MATLAB® ODE solvers take to solve the equations. The equations in this function implement diodes associated with the MOSFETs.

```
function xdot=f(t,x)
global qa qb cma Ac omega alpha As
global I1 d1 I2 d2 Ir dr Ivr
global xd1lx1 xd1lx3mx4
global xd2lx2a xd2lx2x4a xd2lx2mx3x4 xd2lx1 xd2lx2b xd2lx2x4b
global xd2lx3 xd2lx3mx4 xd2lx4 xd2li1 xd2li2 xd2lir
global xd3lx1 xd3lx2 xd3lx2x4 xd3lx3 xd3lx3mx4 xd3li2 xd3lir xd3lxd2
global xd4lx1 xd4lx2 xd4lx3mx4 xd4lx4 xd4li1 xd4li2 xd4lxd2

cm=cma+Ac*cos(omega*t+alpha)';
q=qa+qb*cm;
id1=I1*d1.^x(4,:)-I1;
id2=I2*d2.^x(2,:)-I2;
idr=Ivr*dr.^x(3,:)-Ir;

xdot(1,:)=xd1lx1*x(1,:)+xd1lx3mx4*(x(3,:)-x(4,:));
xdot(2,:)=(xd2lx2a*x(2,:)+xd2lx2x4a*(x(4,:)+x(2,:))+...
   xd2lx2mx3x4*(x(2,:)-x(3,:)+x(4,:))+id2+...
   (xd2lx1*x(1,:)+xd2lx2b*x(2,:)+xd2lx2x4b*(x(2,:)+x(4,:))+...
   xd2lx3*x(3,:)+xd2lx4*x(4,:)+xd2lx3mx4*(x(3,:)-x(4,:))+...
   xd2li1*id1+xd2li2*id2+xd2lir*idr).*cm+...
   As*sin(omega*t-alpha)'.*(x(2,:)-x(3,:)+x(4,:)))./q;
xdot(3,:)=xd3lx1*x(1,:)+xd3lx2*x(2,:)+xd3lx2x4*(x(2,:)+x(4,:))+...
   xd3lx3*x(3,:)+xd3lx3mx4*(x(3,:)-x(4,:))+...
   xd3li2*id2+xd3lir*idr+xd3lxd2*xdot(2,:);
xdot(4,:)=xd4lx1*x(1,:)+xd4lx2*x(2,:)+xd4lx3mx4*(x(3,:)-x(4,:))+...
   xd4lx4*x(4,:)+xd4li1*id1+xd4li2*id2+xd4lxd2*xdot(2,:);
```

C.3 *powerelectronicssynch.m*

This program is called directly within MATLAB®, and returns graphically the results of a simulation. The graphics include the state variables of the simulation, the simulated oscilloscope traces, and the energy absorbed and returned by each element. Finally, it lists the energies of all the elements after one energy conversion cycle. The program differs from *powerelectronicsdiodes.m* in the order of the stages in order to implement synchronous rectification, the MOSFETs do not have diodes associated with them.

The first section lists the global variables shared with the state derivative function *powerelectronicssynchfun.m*. The next section defines the values for all the elements in the model. The third section defines the time intervals where the MOSFETs are on or off. This is a manual process, and a better implementation could find these breakpoints automatically, specially since correct timing values are critical to the operation of the simulated power electronics. The next few sections define the global variables to be shared with *powerelectronicssynchfun.m* in order to minimize the computational burden every time *powerelectronicssynchfun.m* is called within ODE15s.

The next sections call sequentially ODE15s using the previous call as the initial condition for next one. Each section stores both the state variables and its derivatives. As a matter of convenience, each section also displays the amount of time it takes to run in the main window. The next section used the state variable and its derivatives to compute the instantaneous power of each element. These powers are then integrated to find the energies absorbed, return and/or dissipated by each element. The next three sections create the resulting plots and save each plot to a graphical file. The next section finds manually the energies after one cycle and returns these values to the main window. The last three sections create blowout figures to simplify finding the zero crossings when the MOSFETs turn off or on.

The equations solved by this simulation are very stiff; the time constant for the discharging of the MOSFET output capacitance when it closes is in the order of 10^{-10} seconds. The stiffness of the equations makes it essential to use a stiff differential equation solver. Furthermore, ODE15s, the high-order method, returns values that are noticeably different from using a low-order stiff solver.

```
clear

global qa qb cma Ac omega alpha As
global Ir dr Ivr
global xd1lx1 xd1lx3mx4
global xd2lx2a xd2lx2x4a xd2lx2mx3x4 xd2lx1 xd2lx2b xd2lx2x4b
global xd2lx3 xd2lx3mx4 xd2lx4 xd2lir
global xd3lx1 xd3lx2 xd3lx2x4 xd3lx3 xd3lx3mx4 xd3lir xd3lxd2
global xd4lx1 xd4lx2 xd4lx3mx4 xd4lx4 xd4lxd2

cr=1e-6;
l=1e-3;
rl=10;
rc=100e3;%360e3@300khz
cf1=10e-12;
rf1=1;
cf2=cf1;
rf2=rf1;
cmin=89e-12;
deltac=79e-12;
rm=10e9;
Ir=1e-14;
vtr=26e-3;
V=1;
rs1=10e9;
rs2=10e9;
f=2.5e3;
duty=.5;
tcl=9.1e-6;
tcm=.669e-6;
tdm=.4875e-6;
tdl=8.91e-6;
alpha=-pi/2;

%xinit=[iL vF2 vR vF1];
%vF1 should be vR after a long time,
%vMEMS=vF2+vF1-vR;
%if vF1=vR => vF2=vMEMS
xinit=[0 0 1 1];
tp(1)=(1-duty)/2*1/f;
tp(2)=tcl;
tp(3)=tcm;
%transduction
tp(4)=duty*1/f-tcl-tcm;
tp(5)=tdm;
```

```
tp(6)=tdl;
tp(7)=(1-duty)*1/f-tdm-tdl;
tp(8)=tcl;
tp(9)=tcm;
%transduction
tp(10)=duty*1/f-tcl-tcm;
tp(11)=tdm;
tp(12)=tdl;
tp(13)=(1-duty)/2*1/f-tdm-tdl;

%global variables
qa=cf2;
qb=1+cf2*(1/cr+1/cf1);

cma=cmin+deltac/2;
Ac=deltac/2;
omega=2*pi*f;
As=-deltac/2*omega;

Ivr=Ir*exp(V/vtr);
dr=exp(-1/vtr);

xd1lx1=-rc*rl/((rc+rl)*l);
xd1lx3mx4=rc/((rc+rl)*l);

xd2lx2aclosed=-1/rf2;%0 when F2 open
xd2lx2x4a=-1/rs2;
xd2lx2mx3x4=-1/rm;
xd2lx1=-rc/(rc+rl)*(1/cr+1/cf1);
xd2lx2bclosed=-(1/cr+1/cf1)/rf2;%0 when F2 open
xd2lx2x4b=-1/(rs2*cr);
xd2lx3=-1/(rs1*cr);
xd2lx3mx4=-1/(rc+rl)*(1/cr+1/cf1);
xd2lx4closed=1/(rf1*cf1);%0 when F1 open
xd2li1=-1/cf1;
xd2li2=(1/cr+1/cf1);
xd2lir=1/cr;

xd3lx1=-rc/(rc+rl)/cr;
xd3lx2closed=-1/(rf2*cr);%0 when F2 open
xd3lx2x4=-1/(rs2*cr);
xd3lx3=-1/(rs1*cr);
xd3lx3mx4=-1/((rc+rl)*cr);
xd3li2=1/cr;
xd3lir=1/cr;
```

```
xd3lxd2=-cf2/cr;

xd4lx1=rc/(rc+rl)/cf1;
xd4lx2closed=1/(rf2*cf1);%0 when F2 open
xd4lx3mx4=1/((rc+rl)*cf1);
xd4lx4closed=-1/(rf1*cf1);%0 when F1 open
xd4li1=1/cf1;
xd4li2=-1/cf1;
xd4lxd2=cf2/cf1;

%rest
%stage1
disp('stage1')
%F1 open
xd2lx4=0;
xd4lx4=0;
%F2 open
xd2lx2a=0;
xd2lx2b=0;
xd3lx2=0;
xd4lx2=0;
tic
[t1,x1]=ode15s('powerelectronicssynchfun',...
   [0 tp(1)],xinit);
disp(num2str(toc))
x1dot=powerelectronicssynchfun(t1,x1')';

%charging inductor
%stage2
disp('stage2')
%F1 closed
xd2lx4=xd2lx4closed;
xd4lx4=xd4lx4closed;
%F2 open
xd2lx2a=0;
xd2lx2b=0;
xd3lx2=0;
xd4lx2=0;
tic
[t2,x2]=ode15s('powerelectronicssynchfun',...
   [sum(tp(1:1)) sum(tp(1:2))],x1(end,:));
disp(num2str(toc))
x2dot=powerelectronicssynchfun(t2,x2')';

%charging mems
```

```
%stage3
disp('stage3')
%F1 open
xd2lx4=0;
xd4lx4=0;
%F2 open
xd2lx2a=xd2lx2aclosed;
xd2lx2b=xd2lx2bclosed;
xd3lx2=xd3lx2closed;
xd4lx2=xd4lx2closed;
tic
[t3,x3]=ode15s('powerelectronicssynchfun',...
   [sum(tp(1:2)) sum(tp(1:3))],x2(end,:));
disp(num2str(toc))
x3dot=powerelectronicssynchfun(t3,x3')';

%transduction
%stage4
disp('stage4')
%F1 open
xd2lx4=0;
xd4lx4=0;
%F2 closed
xd2lx2a=0;
xd2lx2b=0;
xd3lx2=0;
xd4lx2=0;
tic
[t4,x4]=ode15s('powerelectronicssynchfun',...
   [sum(tp(1:3)) sum(tp(1:4))],x3(end,:));
disp(num2str(toc))
x4dot=powerelectronicssynchfun(t4,x4')';

%discharging mems
%stage5
disp('stage5')
%F1 open
xd2lx4=0;
xd4lx4=0;
%F2 open
xd2lx2a=xd2lx2aclosed;
xd2lx2b=xd2lx2bclosed;
xd3lx2=xd3lx2closed;
xd4lx2=xd4lx2closed;
tic
```

```
[t5,x5]=ode15s('powerelectronicssynchfun',...
   [sum(tp(1:4)) sum(tp(1:5))],x4(end,:));
disp(num2str(toc))
x5dot=powerelectronicssynchfun(t5,x5')';

%discharging inductor
%stage6
disp('stage6')
%F1 closed
xd2lx4=xd2lx4closed;
xd4lx4=xd4lx4closed;
%F2 open
xd2lx2a=0;
xd2lx2b=0;
xd3lx2=0;
xd4lx2=0;
tic
[t6,x6]=ode15s('powerelectronicssynchfun',...
   [sum(tp(1:5)) sum(tp(1:6))],x5(end,:));
disp(num2str(toc))
x6dot=powerelectronicssynchfun(t6,x6')';

%rest
%stage7
disp('stage7')
%F1 open
xd2lx4=0;
xd4lx4=0;
%F2 open
xd2lx2a=0;
xd2lx2b=0;
xd3lx2=0;
xd4lx2=0;
tic
[t7,x7]=ode15s('powerelectronicssynchfun',...
   [sum(tp(1:6)) sum(tp(1:7))],x6(end,:));
disp(num2str(toc))
x7dot=powerelectronicssynchfun(t7,x7')';

%charging inductor
%stage8
disp('stage8')
%F1 open
xd2lx4=xd2lx4closed;
xd4lx4=xd4lx4closed;
```

```
%F2 closed
xd2lx2a=0;
xd2lx2b=0;
xd3lx2=0;
xd4lx2=0;
tic
[t8,x8]=ode15s('powerelectronicssynchfun',...
   [sum(tp(1:7)) sum(tp(1:8))],x7(end,:));
disp(num2str(toc))
x8dot=powerelectronicssynchfun(t8,x8')';

%charging mems
%stage9
disp('stage9')
%F1 open
xd2lx4=0;
xd4lx4=0;
%F2 open
xd2lx2a=xd2lx2aclosed;
xd2lx2b=xd2lx2bclosed;
xd3lx2=xd3lx2closed;
xd4lx2=xd4lx2closed;
tic
[t9,x9]=ode15s('powerelectronicssynchfun',...
   [sum(tp(1:8)) sum(tp(1:9))],x8(end,:));
disp(num2str(toc))
x9dot=powerelectronicssynchfun(t9,x9')';

%transduction
%stage10
disp('stage10')
%F1 closed
xd2lx4=0;
xd4lx4=0;
%F2 open
xd2lx2a=0;
xd2lx2b=0;
xd3lx2=0;
xd4lx2=0;
tic
[t10,x10]=ode15s('powerelectronicssynchfun',...
   [sum(tp(1:9)) sum(tp(1:10))],x9(end,:));
disp(num2str(toc))
x10dot=powerelectronicssynchfun(t10,x10')';
```

```
%discharging mems
%stage11
disp('stage11')
%F1 open
xd2lx4=0;
xd4lx4=0;
%F2 open
xd2lx2a=xd2lx2aclosed;
xd2lx2b=xd2lx2bclosed;
xd3lx2=xd3lx2closed;
xd4lx2=xd4lx2closed;
tic
[t11,x11]=ode15s('powerelectronicssynchfun',...
   [sum(tp(1:10)) sum(tp(1:11))],x10(end,:));
disp(num2str(toc))
x11dot=powerelectronicssynchfun(t11,x11')';

%discharging inductor
%stage12
disp('stage12')
%F1 open
xd2lx4=xd2lx4closed;
xd4lx4=xd4lx4closed;
%F2 closed
xd2lx2a=0;
xd2lx2b=0;
xd3lx2=0;
xd4lx2=0;
tic
[t12,x12]=ode15s('powerelectronicssynchfun',...
   [sum(tp(1:11)) sum(tp(1:12))],x11(end,:));
disp(num2str(toc))
x12dot=powerelectronicssynchfun(t12,x12')';

%rest
%stage13
disp('stage13')
%F1 open
xd2lx4=0;
xd4lx4=0;
%F2 open
xd2lx2a=0;
xd2lx2b=0;
xd3lx2=0;
xd4lx2=0;
```

```
tic
[t13,x13]=ode15s('powerelectronicssynchfun',...
   [sum(tp(1:12)) sum(tp(1:13))],x12(end,:));
disp(num2str(toc))
x13dot=powerelectronicssynchfun(t13,x13')';

t=[t1;t2;t3;t4;t5;t6;t7;t8;t9;t10;t11;t12;t13];
x=[x1;x2;x3;x4;x5;x6;x7;x8;x9;x10;x11;x12;x13];
xdot=[x1dot;x2dot;x3dot;x4dot;x5dot;x6dot;x7dot;...
      x8dot;x9dot;x10dot;x11dot;x12dot;x13dot];
laststate=x(end,:);
beep
disp('Successful integration')
close all

%energy computation
disp('Calculating energies')
il=x(:,1);vf2=x(:,2);vr=x(:,3);vf1=x(:,4);
ildot=xdot(:,1);vf2dot=xdot(:,2);vrdot=xdot(:,3);vf1dot=xdot(:,4);
%source
idr=Ivr*(dr).^vr-Ir;
pdr=-idr.*vr;
edr=integrate(t,pdr,0);
%inductor
ilt=rc/(rc+rl)*il+(vr-vf1)/(rc+rl);
pl=ilt.*(vr-vf1);
el=integrate(t,pl,0);
%reservoir
ir=vr/rs1+cr*vrdot;
pr=vr.*ir;
er=integrate(t,pr,0);
%mems
im=ilt+ir-idr;
vm=vf1+vf2-vr;
pm=im.*vm;
em=integrate(t,pm,0);
%MOSFET1 (bottom)
if1=ilt-im;
pf1=vf1.*if1;
ef1=integrate(t,pf1,0);
%MOSFET2 (top)
pf2=-im.*vf2;
ef2=integrate(t,pf2,0);
icf2=cf2*vf2dot;
pcf2=icf2.*vf2;
```

```
ecf2=integrate(t,pcf2,0);

%plot waveforms
disp('Displaying waveforms')
figure
set(gcf,'Position',[400 35 620 660])
subplot 311
plot(t*1e6,il*1e3)
ylabel('i_L (mA)')
title(strvcat('Power Electronics (State Variables)','(time in \mus)'))
grid on
axis tight
subplot 613
plot(t*1e6,vm)
ylabel('v_{M} (V)')
grid on
axis tight
subplot 614
plot(t*1e6,vr)
ylabel('v_{res} (V)')
grid on
axis tight
subplot 615
plot(t*1e6,vf2)
ylabel('v_{FET2} (V)')
grid on
axis tight
subplot 616
plot(t*1e6,vf1)
ylabel('v_{FET1} (V)')
grid on
axis tight
xlabel(strvcat(['C_{res}=' num2str(cr*1e6) '\muF'...
      '  L=' num2str(l*1e3) 'mH'...
      '  R_L=' num2str(round(rl)) '\Omega'...
      '  R_C=' num2str(rc*1e-3) 'k\Omega'...
      '  C_{FET}=' num2str(cf1*1e12) 'pF'...
      '  R_{FET}=' num2str(rf1) '\Omega'...
      '  C_{min}=' num2str(cmin*1e12) 'pF'...
      '  \DeltaC=' num2str(round(deltac*1e12)) 'pF'...
      '  f=' num2str(f*1e-3) 'kHz'...
      '  duty=' num2str(duty*100) '%'],...
      [ 't_{charge L}=' num2str(tp(2)*1e6) '\mus'...
      '  t_{charge C}=' num2str(tp(3)*1e6) '\mus'...
      '  t_{active}\approx' num2str(round(tp(4)*1e6)) '\mus'...
```

```
      '  t_{discharge C}=' num2str(tp(5)*1e6) '\mus'...
      '  t_{discharge L}=' num2str(tp(6)*1e6) '\mus'...
      '  t_{rest}\approx' num2str(round(tp(7)*1e6)) '\mus']))
print('-dpng',['matlabstate'...
      'Cr' num2str(cr*1e9) 'n'...
      'L'  num2str(l*1e3) 'm'...
      'Rl' num2str(round(rl))...
      'Rc' num2str(round(rc*1e-3)) 'k'...
      'Cf' num2str(cf1*1e12) 'p'...
      'Rf' num2str(rf1)...
      'Cm' num2str(cmin*1e12) 'p'...
      'dC' num2str(round(deltac*1e12)) 'p.png'])

%plot trace
disp('Displaying scope traces')
figure
set(gcf,'Position',[400 35 620 660])
subplot 211
plot(t*1e6,vr+vm)
ylabel('v_{res}+ v_{M} (V)')
title(strvcat('Power Electronics (Scope Traces)','(time in \mus)'))
grid on
subplot 212
plot(t*1e6,vr)
ylabel('v_{res} (V)')
grid on
xlabel(strvcat(['C_{res}=' num2str(cr*1e6) '\muF'...
      '  L=' num2str(l*1e3) 'mH'...
      '  R_L=' num2str(round(rl)) '\Omega'...
      '  R_C=' num2str(rc*1e-3) 'k\Omega'...
      '  C_{FET}=' num2str(cf1*1e12) 'pF'...
      '  R_{FET}=' num2str(rf1) '\Omega'...
      '  C_{min}=' num2str(cmin*1e12) 'pF'...
      '  \DeltaC=' num2str(round(deltac*1e12)) 'pF'...
      '  f=' num2str(f*1e-3) 'kHz'...
      '  duty=' num2str(duty*100) '%'],...
      [ 't_{charge L}=' num2str(tp(2)*1e6) '\mus'...
      '  t_{charge C}=' num2str(tp(3)*1e6) '\mus'...
      '  t_{active}\approx' num2str(round(tp(4)*1e6)) '\mus'...
      '  t_{discharge C}=' num2str(tp(5)*1e6) '\mus'...
      '  t_{discharge L}=' num2str(tp(6)*1e6) '\mus'...
      '  t_{rest}\approx' num2str(round(tp(7)*1e6)) '\mus']))
print('-dpng',['matlabscope'...
      'Cr' num2str(cr*1e9) 'n'...
      'L'  num2str(l*1e3) 'm'...
```

```
      'Rl' num2str(round(rl))...
      'Rc' num2str(round(rc*1e-3)) 'k'...
      'Cf' num2str(cf1*1e12) 'p'...
      'Rf' num2str(rf1)...
      'Cm' num2str(cmin*1e12) 'p'...
      'dC' num2str(round(deltac*1e12)) 'p.png'])

%plot energies
disp('Displaying energies')
figure
set(gcf,'Position',[400 35 620 660])
subplot 511
plot(t(1:end)*1e6,el(1:end)*1e9)
grid on
axis tight
title(strvcat('Power Electronics (Energies)','(time in \mus)'))
ylabel('E_{L} (nJ)')
subplot 512
plot(t(1:end)*1e6,em(1:end)*1e9)
grid on
axis tight
ylabel('E_{M} (nJ)')
subplot 513
plot(t(1:end)*1e6,er(1:end)*1e9)
grid on
axis tight
ylabel('E_{res} (nJ)')
subplot 514
plot(t(1:end)*1e6,ef2(1:end)*1e9)
grid on
axis tight
ylabel('E_{F2} (nJ)')
subplot 515
plot(t(1:end)*1e6,ef1(1:end)*1e9)
grid on
axis tight
ylabel('E_{F1} (nJ)')
xlabel(strvcat(['C_{res}=' num2str(cr*1e6) '\muF'...
      '  L=' num2str(l*1e3) 'mH'...
      '  R_L=' num2str(round(rl)) '\Omega'...
      '  R_C=' num2str(rc*1e-3) 'k\Omega'...
      '  C_{FET}=' num2str(cf1*1e12) 'pF'...
      '  R_{FET}=' num2str(rf1) '\Omega'...
      '  C_{min}=' num2str(cmin*1e12) 'pF'...
      '  \DeltaC=' num2str(round(deltac*1e12)) 'pF'...
```

```
      '  f=' num2str(f*1e-3) 'kHz'...
      '  duty=' num2str(duty*100) '%'],...
      [ 't_{charge L}=' num2str(tp(2)*1e6) '\mus'...
      '  t_{charge C}=' num2str(tp(3)*1e6) '\mus'...
      '  t_{active}\approx' num2str(round(tp(4)*1e6)) '\mus'...
      '  t_{discharge C}=' num2str(tp(5)*1e6) '\mus'...
      '  t_{discharge L}=' num2str(tp(6)*1e6) '\mus'...
      '  t_{rest}\approx' num2str(round(tp(7)*1e6)) '\mus']))
print('-dpng',['matlabenergies'...
      'Cr' num2str(cr*1e9) 'n'...
      'L'  num2str(l*1e3) 'm'...
      'Rl' num2str(round(rl))...
      'Rc' num2str(round(rc*1e-3)) 'k'...
      'Cf' num2str(cf1*1e12) 'p'...
      'Rf' num2str(rf1)...
      'Cm' num2str(cmin*1e12) 'p'...
      'dC' num2str(round(deltac*1e12)) 'p.png'])

index=find(t>380e-6&t<420e-6);
index=index(1);
disp(['v_r='num2str(vr(index))])
disp(['DeltaE=' num2str(.5*cr*vr(index)^2*1e9-500)])
disp(['P='  num2str((.5*cr*vr(index)^2-500e-9)*f*1e6)])
disp(['Em=' num2str(em(index)*1e9)])
disp(['Er=' num2str(er(index)*1e9)])
disp(['P='  num2str(er(index)*f*1e6)])
disp(['El=' num2str(el(index)*1e9)])
disp(['Ef1=' num2str(ef1(index)*1e9)])
disp(['Ef2=' num2str(ef2(index)*1e9)])
disp(['Ef=' num2str((ef1(index)+ef2(index))*1e9)])
disp(['Elt=' num2str((ef1(index)+ef2(index)+el(index))*1e9)])

e=1e-6;
indt=find(t>(sum(tp(1:3))-e)&t<(sum(tp(1:3))+e));
indi=find(il(indt)<0);
if isempty(indi),
   disp('No zero crossing found for tcm')
else
tcross=t(indt(1)+indi(1)-2)-il(indt(1)+indi(1)-2)/(il(indt(1)+indi(1)-1)-...
   il(indt(1)+indi(1)-2))*(t(indt(1)+indi(1)-1)-t(indt(1)+indi(1)-2));
tcm=tcross-sum(tp(1:2));
figure
plot((t(indt)-sum(tp(1:2)))*1e6,il(indt)*1e3,'+')
grid on
hold on
```

```
plot((t(indt(1)+indi(1)-1)-sum(tp(1:2)))*1e6,il(indt(1)+indi(1)-1)*1e3,'ro')
plot((t(indt(1)+indi(1)-2)-sum(tp(1:2)))*1e6,il(indt(1)+indi(1)-2)*1e3,'ro')
plot((tcross-sum(tp(1:2)))*1e6,0,'m*')
title(['t_{before}='num2str((t(indt(1)+indi(1)-2)-sum(tp(1:2)))*1e6)...
      '  tcm='num2str(tcm*1e6)...
      '  t_{after}='num2str((t(indt(1)+indi(1)-1)-sum(tp(1:2)))*1e6)])
end

e=1e-6;
indt=find(t>(sum(tp(1:5))-e)&t<(sum(tp(1:5))+e));
indi=find(vm(indt)<0);
if isempty(indi),
   disp('No zero crossing found for tdm')
else
tcross=t(indt(1)+indi(1)-2)-vm(indt(1)+indi(1)-2)/(vm(indt(1)+indi(1)-1)-...
   vm(indt(1)+indi(1)-2))*(t(indt(1)+indi(1)-1)-t(indt(1)+indi(1)-2));
tdm=tcross-sum(tp(1:4));
figure
plot((t(indt)-sum(tp(1:4)))*1e6,vm(indt),'+')
grid on
hold on
plot((t(indt(1)+indi(1)-1)-sum(tp(1:4)))*1e6,vm(indt(1)+indi(1)-1),'ro')
plot((t(indt(1)+indi(1)-2)-sum(tp(1:4)))*1e6,vm(indt(1)+indi(1)-2),'ro')
plot((tcross-sum(tp(1:4)))*1e6,0,'m*')
title(['t_{before}='num2str((t(indt(1)+indi(1)-2)-sum(tp(1:4)))*1e6)...
      '  tdm='num2str(tdm*1e6)...
      '  t_{after}='num2str((t(indt(1)+indi(1)-1)-sum(tp(1:4)))*1e6)])
end

e=3e-6;
indt=find(t>(sum(tp(1:6))-e)&t<(sum(tp(1:6))+e));
indi=find(il(indt)>0);
if isempty(indi),
   disp('No zero crossing found for tdl')
else
tcross=t(indt(1)+indi(1)-2)-il(indt(1)+indi(1)-2)/(il(indt(1)+indi(1)-1)-...
   il(indt(1)+indi(1)-2))*(t(indt(1)+indi(1)-1)-t(indt(1)+indi(1)-2));
tdl=tcross-sum(tp(1:5));
figure
plot((t(indt)-sum(tp(1:5)))*1e6,il(indt)*1e3,'+')
grid on
hold on
plot((t(indt(1)+indi(1)-1)-sum(tp(1:5)))*1e6,il(indt(1)+indi(1)-1)*1e3,'ro')
plot((t(indt(1)+indi(1)-2)-sum(tp(1:5)))*1e6,il(indt(1)+indi(1)-2)*1e3,'ro')
plot((tcross-sum(tp(1:5)))*1e6,0,'m*')
```

```
title(['t_{before}='num2str((t(indt(1)+indi(1)-2)-sum(tp(1:5)))*1e6)...
      '  tdl='num2str(tdl*1e6)...
      '  t_{after}='num2str((t(indt(1)+indi(1)-1)-sum(tp(1:5)))*1e6)])
end

disp('End of File')
```

C.4 *powerelectronicssynchfun.m*

This function returns the state derivatives as required by MATLAB®'s ODE solvers. Furthermore, it is also capable of returning a whole vector of state derivatives if the inputs are vectors of time and state variables. It shares most variables with *powerelectronicssynch.m* to minimize the amount of computation it must do every time it is called. This drastically minimizes the amount of time the MATLAB® ODE solvers take to solve the equations. The equations in this function do not implement diodes associated with the MOSFETs.

```
function xdot=f(t,x)
global qa qb cma Ac omega alpha As
global Ir dr Ivr
global xd1lx1 xd1lx3mx4
global xd2lx2a xd2lx2x4a xd2lx2mx3x4 xd2lx1 xd2lx2b xd2lx2x4b
global xd2lx3 xd2lx3mx4 xd2lx4 xd2lir
global xd3lx1 xd3lx2 xd3lx2x4 xd3lx3 xd3lx3mx4 xd3lir xd3lxd2
global xd4lx1 xd4lx2 xd4lx3mx4 xd4lx4 xd4lxd2

cm=cma+Ac*cos(omega*t+alpha)';
q=qa+qb*cm;
idr=Ivr*dr.^x(3,:)-Ir;

xdot(1,:)=xd1lx1*x(1,:)+xd1lx3mx4*(x(3,:)-x(4,:));
xdot(2,:)=(xd2lx2a*x(2,:)+xd2lx2x4a*(x(4,:)+x(2,:))+...
   xd2lx2mx3x4*(x(2,:)-x(3,:)+x(4,:))+...
   (xd2lx1*x(1,:)+xd2lx2b*x(2,:)+xd2lx2x4b*(x(2,:)+x(4,:))+...
   xd2lx3*x(3,:)+xd2lx4*x(4,:)+xd2lx3mx4*(x(3,:)-x(4,:))+...
   xd2lir*idr).*cm+...
   As*sin(omega*t-alpha)'.*(x(2,:)-x(3,:)+x(4,:))./q;
xdot(3,:)=xd3lx1*x(1,:)+xd3lx2*x(2,:)+xd3lx2x4*(x(2,:)+x(4,:))+...
   xd3lx3*x(3,:)+xd3lx3mx4*(x(3,:)-x(4,:))+...
   xd3lir*idr+xd3lxd2*xdot(2,:);
```

```
xdot(4,:)=xd4lx1*x(1,:)+xd4lx2*x(2,:)+xd4lx3mx4*(x(3,:)-x(4,:))+...
   xd4lx4*x(4,:)+xd4lxd2*xdot(2,:);
```

C.5 *integrate.m*

This function takes two vectors, p, and t, and constant C. It performs a trapezoidal integration of the series p as a function of time t and initial value C. It returns the integrated vector e, of the same length as p and t. It is called from *powerelectronicsdiodes.m* and *powerelectronicssynch.m* to compute energies out of power series.

```
function e=integrate(t,p,C);
e=[C;cumsum((t(2:end)-t(1:end-1)).*(p(2:end)+p(1:end-1))/2)+C];
```

Appendix D

TN-2510 MOSFET Data Sheet

The TN-2510 MOSFET is used in the test circuit built in Chapter 3. They are surface-mounted vertical MOSFETs with a low output capacitance. They have a parasitic diode specified by a V_{SD} of 1.8 V when I_{SD} is 1.5 mA. This correspond to a saturation current of 10^{-30} A in an exponential diode model. This is a comparatively lossy diode, and even though it was used as part of the rectification circuitry, future designs should either bypass the diode with a less lossy diode. Schoktty diodes have saturation currents as low as 10^{-8} A. An alternative is to use synchronous rectification, where the MOSFET is turned on every time current must flow through it so that the diodes are bypassed. Other values used in the model of the MOSFET where the ON channel resistance ($R_F = 1.5\ \Omega$), and the output capacitance used in the model was $C_F = 95$ pF. This capacitance was the value which best matched the experimental traces while still being in reasonable accordance with the data sheet information, given that the drain-to-source voltages of the MOSFETs during operation ranged from low voltages to zero.

N-Channel Enhancement-Mode Vertical DMOS FETs

Ordering Information

BV_{DSS} / BV_{DGS}	$R_{DS(ON)}$ (max)	$V_{GS(th)}$ (max)	$I_{D(ON)}$ (min)	Order Number / Package	
				TO-243AA*	Die†
100V	1.5Ω	2.0V	3.0A	TN2510N8	TN2510ND

* Same as SOT-89. Product supplied on 2000 piece carrier tape reels.
† MIL visual screening available.

Product marking for TO-243AA:

TN5A*

Where * = 2-week alpha date code

Features

- Low threshold —2.0V max.
- High input impedance
- Low input capacitance — 125pF max.
- Fast switching speeds
- Low on resistance
- Free from secondary breakdown
- Low input and output leakage
- Complementary N- and P-channel devices

Applications

- Logic level interfaces – ideal for TTL and CMOS
- Solid state relays
- Battery operated systems
- Photo voltaic drives
- Analog switches
- General purpose line drivers
- Telecom switches

Absolute Maximum Ratings

Drain-to-Source Voltage	BV_{DSS}
Drain-to-Gate Voltage	BV_{DGS}
Gate-to-Source Voltage	± 20V
Operating and Storage Temperature	-55°C to +150°C
Soldering Temperature*	300°C

* Distance of 1.6 mm from case for 10 seconds.

Low Threshold DMOS Technology

These low threshold enhancement-mode (normally-off) transistors utilize a vertical DMOS structure and Supertex's well-proven silicon-gate manufacturing process. This combination produces devices with the power handling capabilities of bipolar transistors and with the high input impedance and positive temperature coefficient inherent in MOS devices. Characteristic of all MOS structures, these devices are free from thermal runaway and thermally-induced secondary breakdown.

Supertex's vertical DMOS FETs are ideally suited to a wide range of switching and amplifying applications where very low threshold voltage, high breakdown voltage, high input impedance, low input capacitance, and fast switching speeds are desired.

Package Option

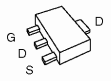

TO-243AA
(SOT-89)

Note: See Package Outline section for dimensions.

11/12/01

Thermal Characteristics

Package	I_D (continuous)*	I_D (pulsed)	Power Dissipation @ T_A = 25°C	θ_{jc} °C/W	θ_{ja} °C/W	I_{DR}*	I_{DRM}
TO-243AA	0.73A	5.0A	1.6W†	15	78†	0.73A	5.0A

* I_D (continuous) is limited by max rated T_j.
† Mounted on FR5 board, 25mm x 25mm x 1.57mm. Significant P_D increase possible on ceramic substrate.

Electrical Characteristics (@ 25°C unless otherwise specified)

Symbol	Parameter	Min	Typ	Max	Unit	Conditions
BV_{DSS}	Drain-to-Source Breakdown Voltage	100			V	V_{GS} = 0V, I_D = 2mA
$V_{GS(th)}$	Gate Threshold Voltage	0.6		2.0	V	V_{GS} = V_{DS}, I_D= 1mA
$\Delta V_{GS(th)}$	Change in $V_{GS(th)}$ with Temperature			-4.5	mV/°C	V_{GS} = V_{DS}, I_D= 1.0mA
I_{GSS}	Gate Body Leakage			100	nA	V_{GS} = ± 20V, V_{DS} = 0V
I_{DSS}	Zero Gate Voltage Drain Current			10	µA	V_{GS} = 0V, V_{DS} = Max Rating
				1.0	mA	V_{GS} = 0V, V_{DS} = 0.8 Max Rating T_A = 125°C
$I_{D(ON)}$	ON-State Drain Current	1.2	2.0		A	V_{GS} = 5.0V, V_{DS} = 25V
		3.0	6.0			V_{GS} = 10V, V_{DS} = 25V
$R_{DS(ON)}$	Static Drain-to-Source ON-State Resistance			15	Ω	V_{GS} = 3.0V, I_D = 250mA
			1.5	2.0		V_{GS} = 4.5V, I_D = 750mA
			1.0	1.5		V_{GS} = 10V, I_D = 750mA
$\Delta R_{DS(ON)}$	Change in $R_{DS(ON)}$ with Temperature			0.75	%/°C	V_{GS} = 10V, I_D = 750mA
G_{FS}	Forward Transconductance	0.4	0.8		℧	V_{DS} = 25V, I_D = 1.0A
C_{ISS}	Input Capacitance		70	125	pF	V_{GS} = 0V, V_{DS} = 25V f = 1 MHz
C_{OSS}	Common Source Output Capacitance		30	70		
C_{RSS}	Reverse Transfer Capacitance		15	25		
$t_{d(ON)}$	Turn-ON Delay Time			10	ns	V_{DD} = 25V, I_D = 1.5A, R_{GEN} = 25Ω
t_r	Rise Time			10		
$t_{d(OFF)}$	Turn-OFF Delay Time			20		
t_f	Fall Time			10		
V_{SD}	Diode Forward Voltage Drop			1.8	V	V_{GS} = 0V, I_{SD} = 1.5A
t_{rr}	Reverse Recovery Time		300		ns	V_{GS} = 0V, I_{SD} = 1.5A

Notes:
1. All D.C. parameters 100% tested at 25°C unless otherwise stated. (Pulse test: 300µs pulse, 2% duty cycle.)
2. All A.C. parameters sample tested.

Switching Waveforms and Test Circuit

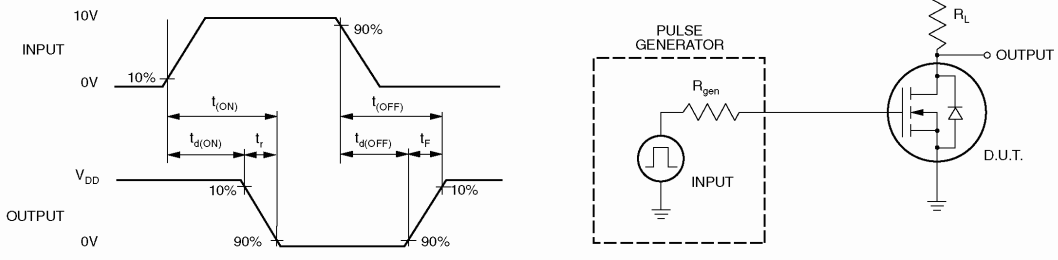

Typical Performance Curves

Output Characteristics

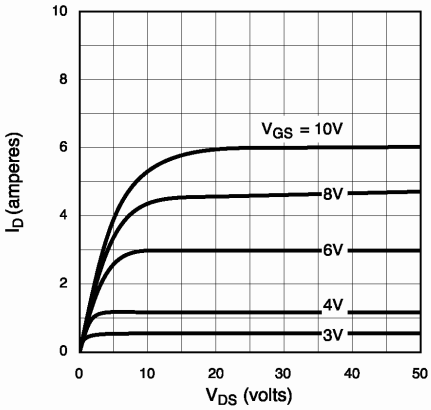

Saturation Characteristics

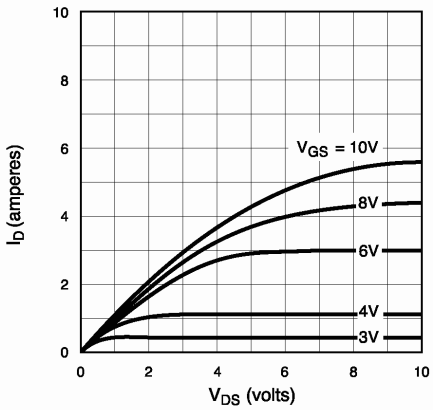

Transconductance vs. Drain Current

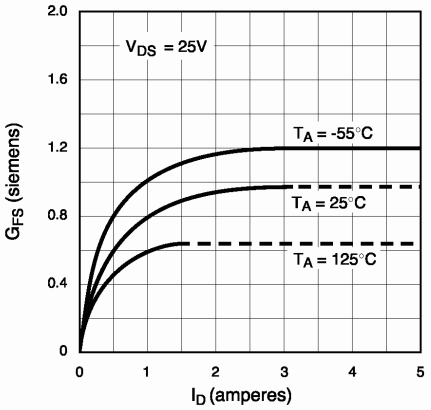

Power Dissipation vs. Ambient Temperature

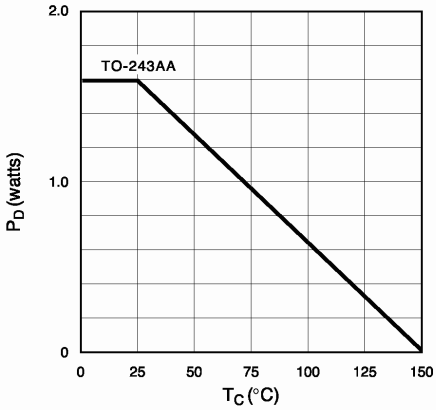

Maximum Rated Safe Operating Area

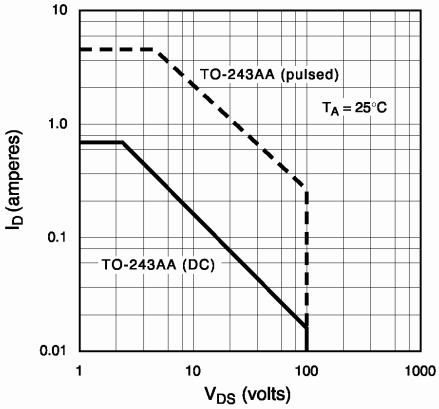

Thermal Response Characteristics

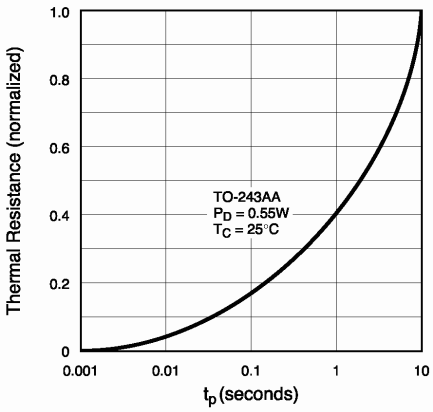

Typical Performance Curves

BV$_{DSS}$ Variation with Temperature

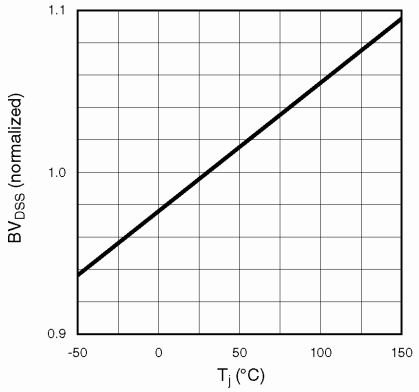

On-Resistance vs. Drain Current

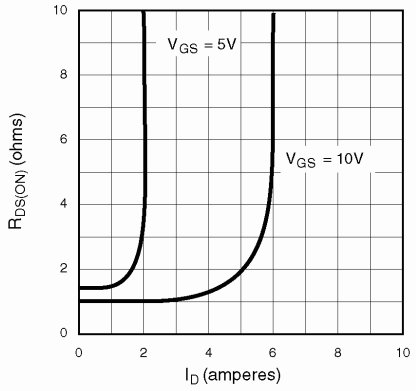

Transfer Characteristics

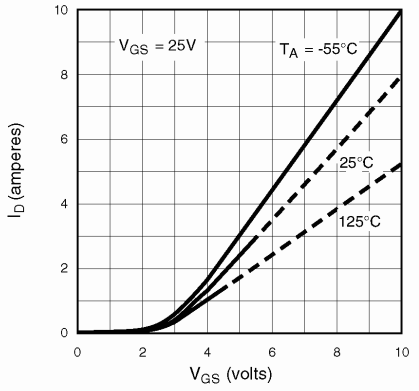

V$_{(th)}$ and R$_{DS}$ Variation with Temperature

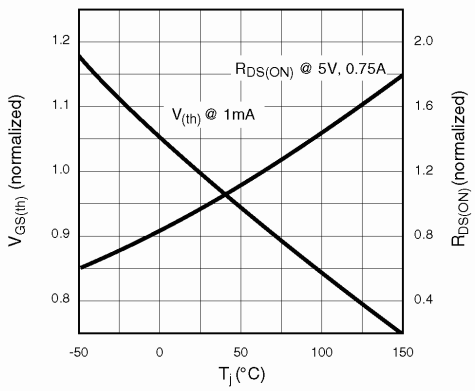

Capacitance vs. Drain-to-Source Voltage

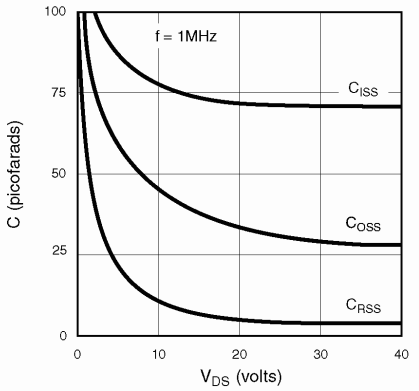

Gate Drive Dynamic Characteristics

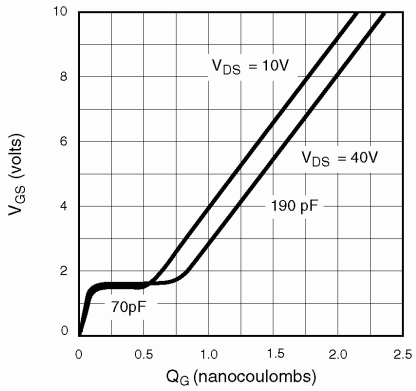

Supertex inc.

1235 Bordeaux Drive, Sunnyvale, CA 94089
TEL: (408) 744-0100 • FAX: (408) 222-4895
www.supertex.com

Appendix E

Spring Beam

The beam flexures used in the design of the suspension shown in Figures 6-3 and 6-4 act as linear springs provided that their deflection is small. This Appendix derives the spring constant and energy content of single-beam springs with the same boundary conditions. These results allow the derivation of an effective spring constant for the suspensions composed of several beam springs. Figure E-1 shows one such spring beam and defines the dimensions and coordinates used in this derivation. The dashed centerline of the beam is described by $y(x)$. The length of the beam is L, its thickness is h and its width is b. Following the constraints imposed by the suspension, the beam is fixed at the origin, and free at the other end, but the slope at the free end is constrained to be zero. Thus, the boundary conditions for this beam are $y(0) = 0$, $y'(0) = 0$ and $y'(L) = 0$, Where $y'(x)$ refers to the first derivative of $y(x)$ with respect to x. The expression for y' will be of the form [31]

$$y'(x) = x(L - x)C_1 = (Lx - x^2)C_1, \tag{E.1}$$

where C_1 is an arbitrary constant. This expression fulfills the conditions $y'(0) = 0$ and $y'(L) = 0$. Integrating Equation E.1,

$$y(x) = \left(\frac{Lx^2}{2} - \frac{x^3}{3}\right)C_1 = (3Lx^2 - 2x^3)C_0, \tag{E.2}$$

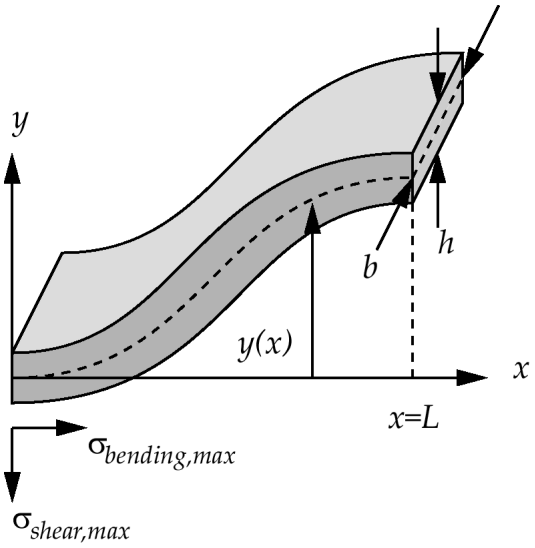

Figure E-1: Rectangular beam undergoing deflection. The deflection is greatly exaggerated for clarity. The dashed centerline of the beam is described by $y(x)$. The length of the beam is L, its height is h and its depth is b. The beam is fixed at the origin, and free at the other end, but the slope at the free end is constrained to be zero.

where the condition $y(0) = 0$ has been met and C_0 is defined so that the expression for y does not contain fractions. The second derivative of y is the curvature of the beam and is related to the moment M [31],

$$y''(x) = \frac{M}{EI} \tag{E.3}$$

where E is Young's modulus and I is the second moment of inertia about the neutral axis. For a rectangular beam, $I = bh^3/12$. The complete set of derivatives for the beam and their relation to applied forces are

$$y(x) = C_0(3Lx^2 - 2x^3) \qquad \text{displacement} \tag{E.4}$$

$$y'(x) = 6C_0(Lx - x^2) \qquad \text{angle} \tag{E.5}$$

$$y''(x) = 6C_0(L - 2x) = \frac{M}{EI} \qquad \text{curvature} \tag{E.6}$$

$$y'''(x) = -12C_0 = \frac{V}{EI} \qquad \text{shear} \tag{E.7}$$

$$y''''(x) = 0 = \frac{W}{EI} \qquad \text{distributed load} \tag{E.8}$$

The beam in the suspension is under a point loading at $x = L$ with a load force F. This point load results in a constant shear $V = F$ [31]. Using this shear,

$$\frac{F}{EI} = -12C_0 \Rightarrow C_0 = -\frac{F}{12EI} \tag{E.9}$$

and

$$y(x) = \frac{F}{12EI}(3Lx^2 - 2x^3) \tag{E.10}$$

The maximal displacement occurs at $x = L$,

$$y_{max} = y(L) = -\frac{F_{max}}{12EI}(3L^3 - 2L^3) = -\frac{F_{max}L^3}{12EI} \tag{E.11}$$

Solving for the load F_{max},

$$F_{max} = -\frac{12EI}{L^3}y_{max} \tag{E.12}$$

Substituting the expression $I = bh^3/12$ for a rectangular beam yields

$$F_{max} = -\frac{Ebh^3}{L^3}y_{max} \tag{E.13}$$

The effective spring constant of the beam, $F = -Ky_{max}$, can be extracted from this expression as

$$K = \frac{Ebh^3}{L^3} \tag{E.14}$$

The computation of the effective spring constant of the suspensions in Chapter 6 will be done using energy arguments. In sinusoidal steady state, the energy U stored in the beam is $\frac{1}{2}Ky_{max}^2$, so that

$$U = \frac{1}{2}\frac{Ebh^3}{L^3}y_{max}^2 \tag{E.15}$$

The maximum shear $\sigma_{shear,max}$ is constant throughout the beam, and is equal to

$$\sigma_{shear,max} = \frac{V}{bh} = \frac{F_{max}}{bh} = \frac{Ky_{max}}{bh} = \frac{Eh^2}{L^3}y_{max} \tag{E.16}$$

The normal, or bending stress $\sigma_{bending,max}$ is proportional to the moment in the beam and the distance from the centerline of the beam. The maximum bending stress in this beam occurs in the surface of the beam at the ends and is equal to

$$\sigma_{bending,max} = \frac{M_{max}h/2}{I} = \frac{F_{max}L}{2}\frac{h}{2I} \tag{E.17}$$

Substitution of Equation E.12 into Equation E.17 yields

$$\sigma_{bending,max} = \frac{3Eh}{L^2}y_{max} \tag{E.18}$$

Appendix F

Flexure Spring Suspension

Figure F-1 shows a fabricated flexure spring, and defines the flexure spring radius R and the flexure spring width t. The torsional spring constant K_r such that $\tau = K_r\theta$, where τ is the applied torque and θ is the displacement angle, is [33]

$$K_r = \frac{2R^2EW}{3s} \tag{F.1}$$

where E is Young's Modulus, and W is the depth of the spring into the wafer plane. The variable s is a function defined as

$$s = \frac{1}{\gamma(\gamma^2-1)^2}\left[2\gamma^2 + 1 + \frac{3\gamma^2}{\sqrt{\gamma^2-1}}\left(\frac{\pi}{2} + \tan^{-1}\frac{1}{\sqrt{\gamma^2-1}}\right)\right] \tag{F.2}$$

where $\gamma = 1 + \frac{t}{2R}$. Figure F-2 shows a suspension where 16 flexure springs are used. The flexure springs are connected by rigid beams of length L (defined from the center of a flexure spring to the other center). If the shuttle mass is displaced a distance x, each beam will be deflected a distance $x/2$. Furthermore, the distance $x/2$ is much smaller than the beam length L, such that the displacement angle $\theta \approx \frac{x/2}{L}$. The effective spring constant K can be found by equating the energy stored in the effective spring $\frac{1}{2}Kx^2$ with the total energy stored in all the flexure springs $\frac{1}{2}K_r\theta^2$

$$\frac{1}{2}Kx^2 = 16\frac{1}{2}K_r\frac{1}{4L^2}x^2 \tag{F.3}$$

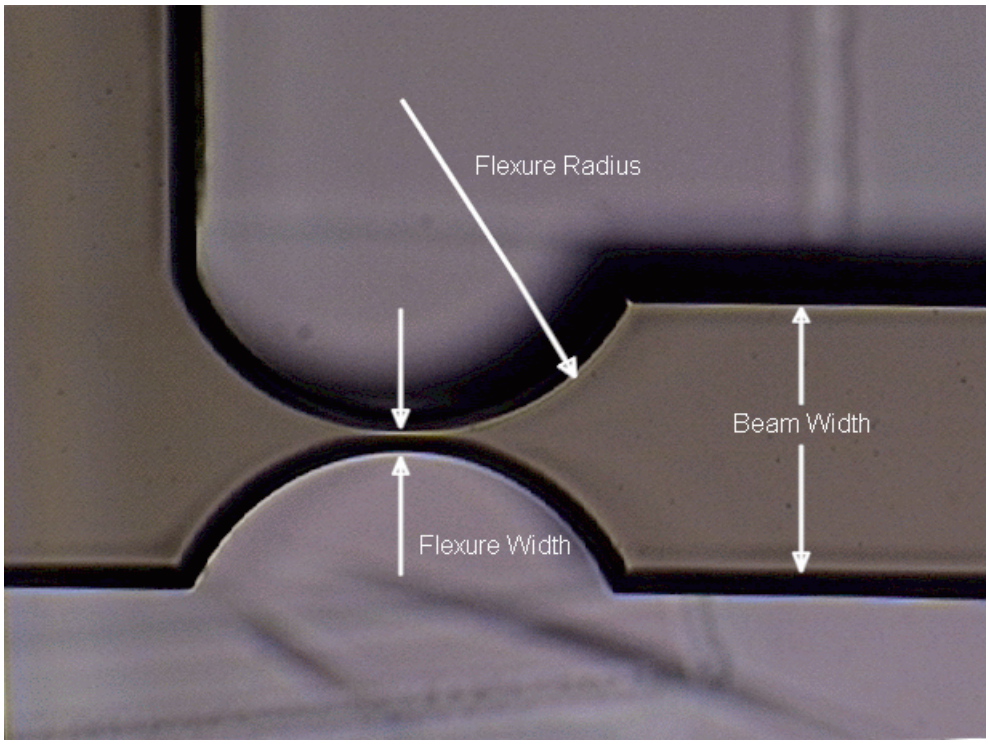

Figure F-1: Flexure Spring.

$$\Rightarrow K = \frac{16K_r}{4L^2} = \frac{16}{4L^2}\frac{2EWR^2}{3s} \tag{F.4}$$

The maximum stress, at the center of the flexure spring, is [33]

$$\sigma_{max} = \frac{6\tau}{t^2W} \approx \frac{6K_r x}{2Lt^2W} = \frac{2R^2E}{Lt^2s}x \tag{F.5}$$

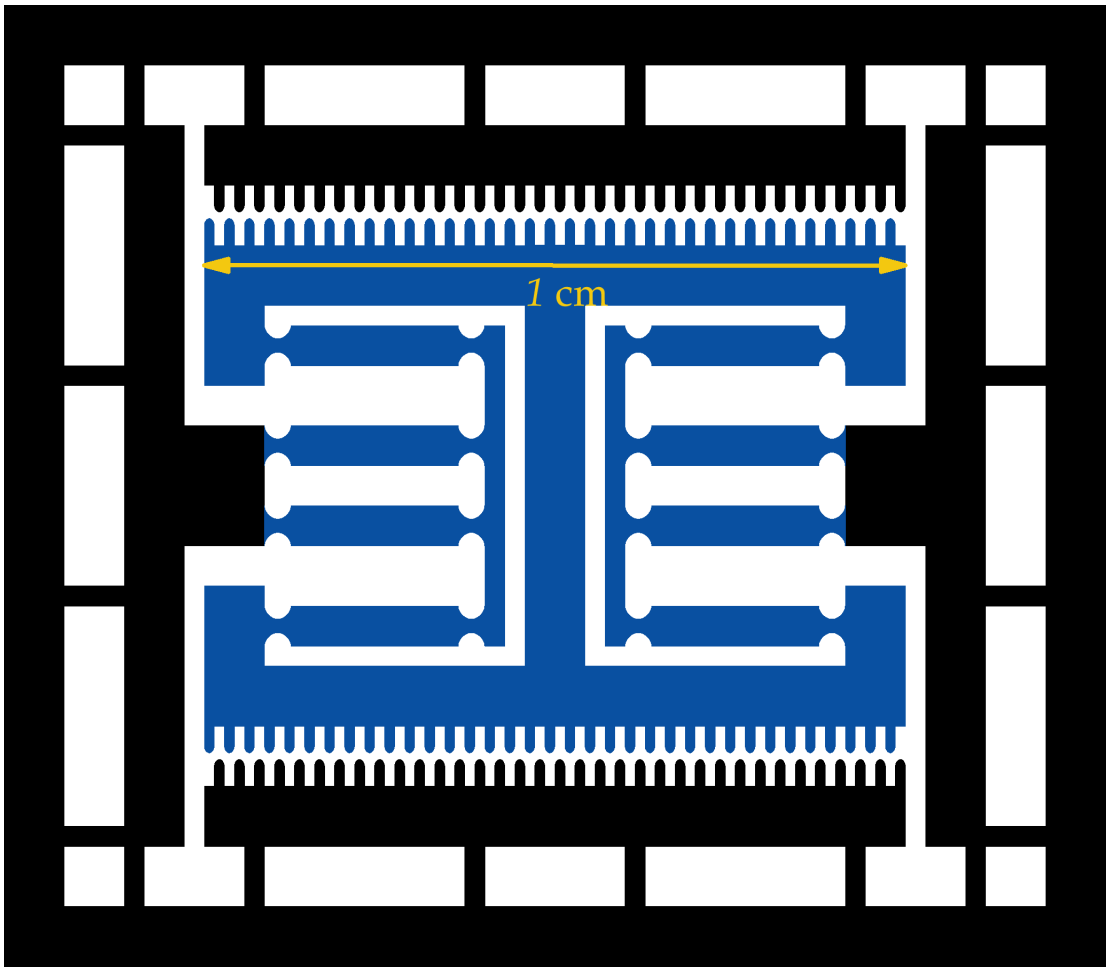

Figure F-2: Plan view of a constant-gap energy harvester with non-overlapping fingers and four-bar linkage suspension.

Appendix G

Fabrication Processes

The constant-gap process in this appendix was used together with the masks shown in Appendix H to create the examples shown in Chapter 7. Problems and solution incorporated in this process are discussed in Chapter 8. The variable-gap process was not attempted, but was designed to follow easy fabrication steps.

G.1 Constant-Gap Converter

This process attempts to create a constant-gap capacitor. The I-shaped Si mass moves up and down in the top view using a 4-bar, multiple-beam suspension of Si as a spring. Probes connect to the fixed Si anchors, shown in black.

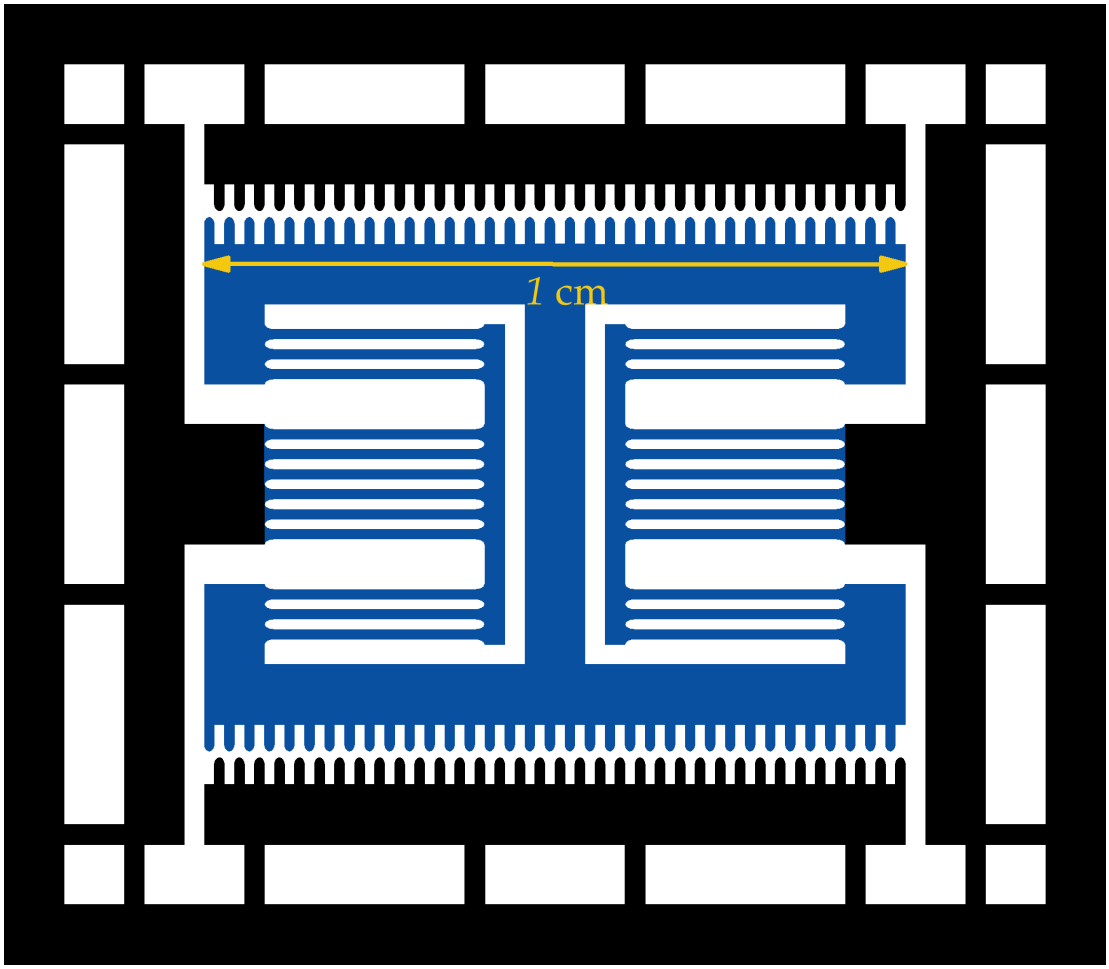

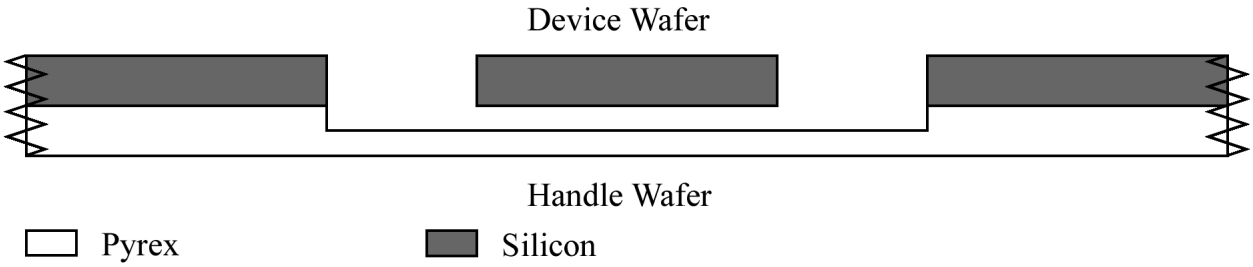

G.1.1 Device Wafer

1. Device wafers are nSi prime wafers, double polished, 500 μm thick, doped using $POCl_3$ with 1 μm grown thermal oxide.

2. Coat frontside with 10 μm thick resist.

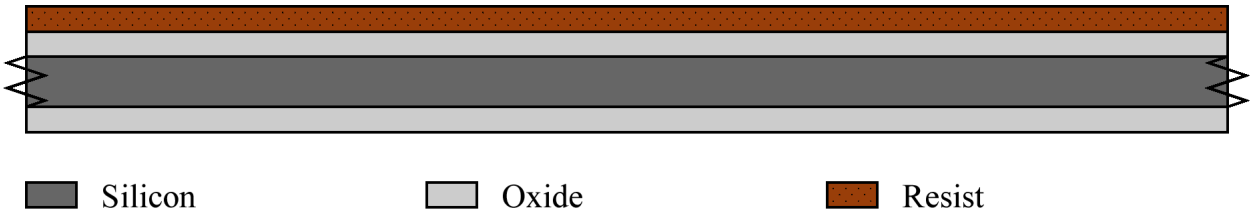

3. Develop frontside side using "DEVICE" mask.

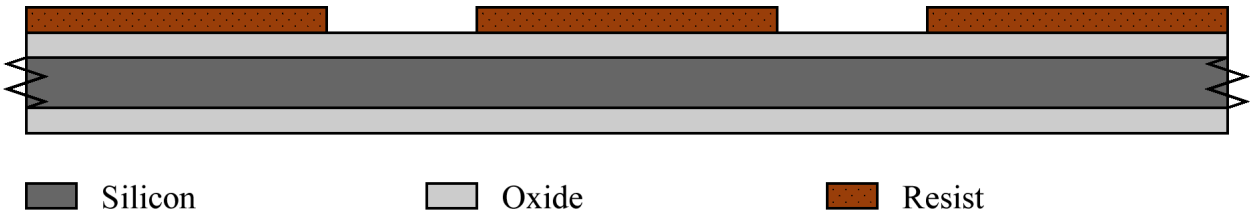

4. BOE etch of 1 μm TOx.

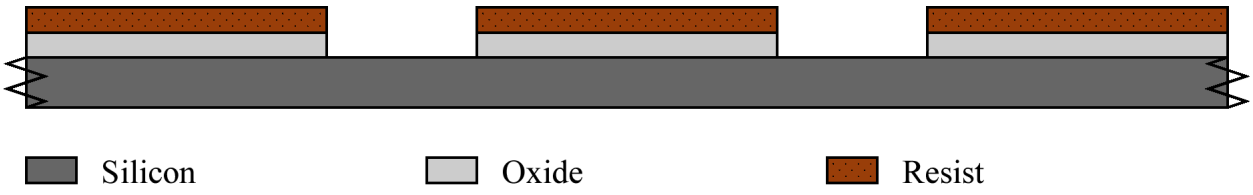

5. STS through-etch of Si.

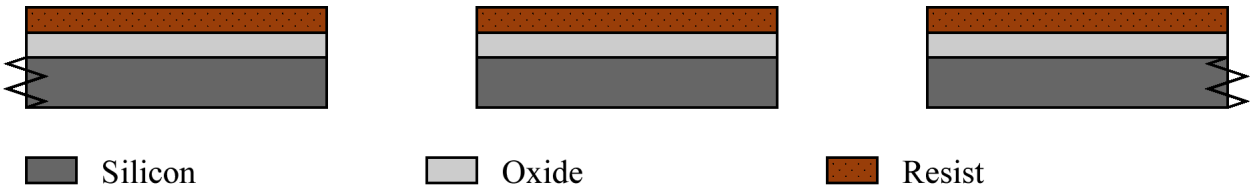

6. Acetone removal of resist.

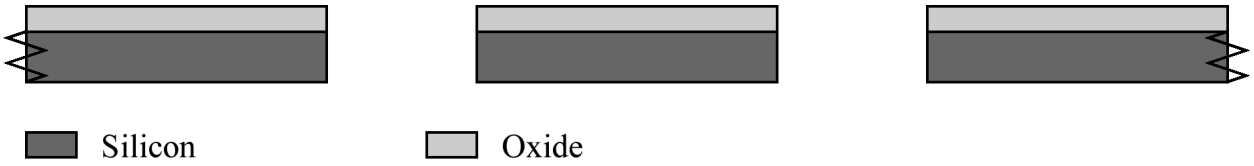

7. BOE etch of frontside TOx.

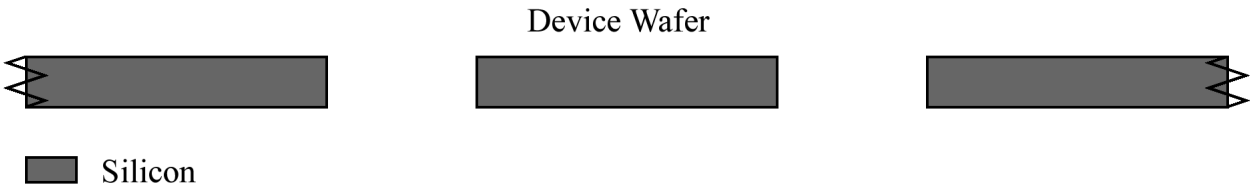

G.1.2 Handle Wafer

8. Handle wafers are 7740 Pyrex wafers, 500 μm thick.

9. Coat both sides with resist.

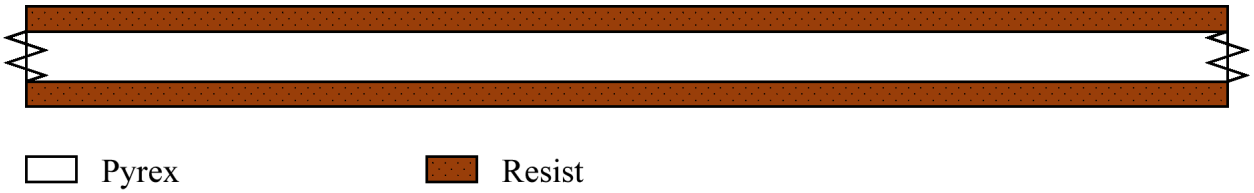

10. Develop resist using "PIT" mask.

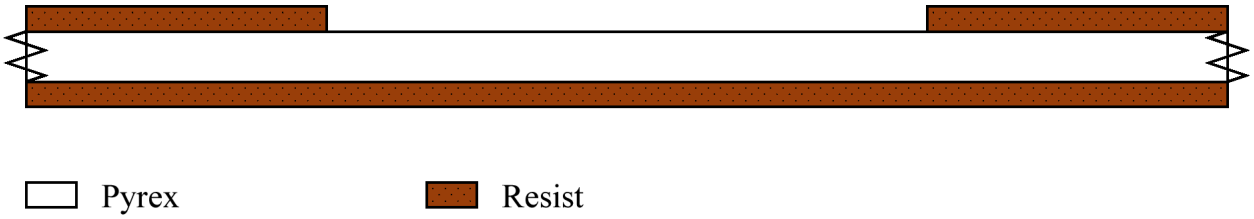

11. HF etch of Pyrex.

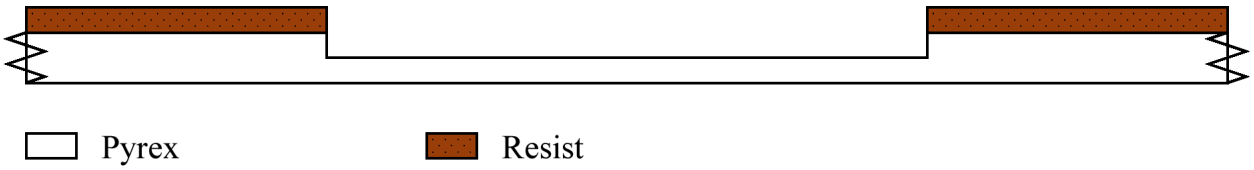

12. Gold piranha clean of resist.

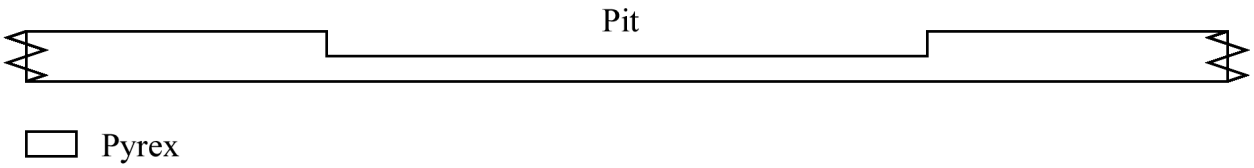

13. Anodic bond.

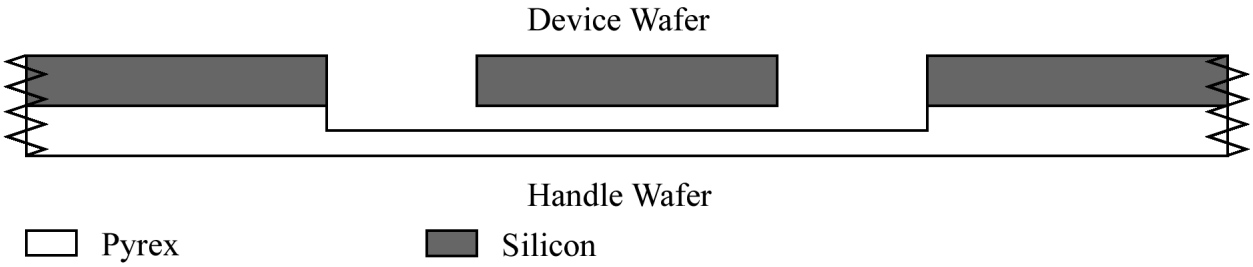

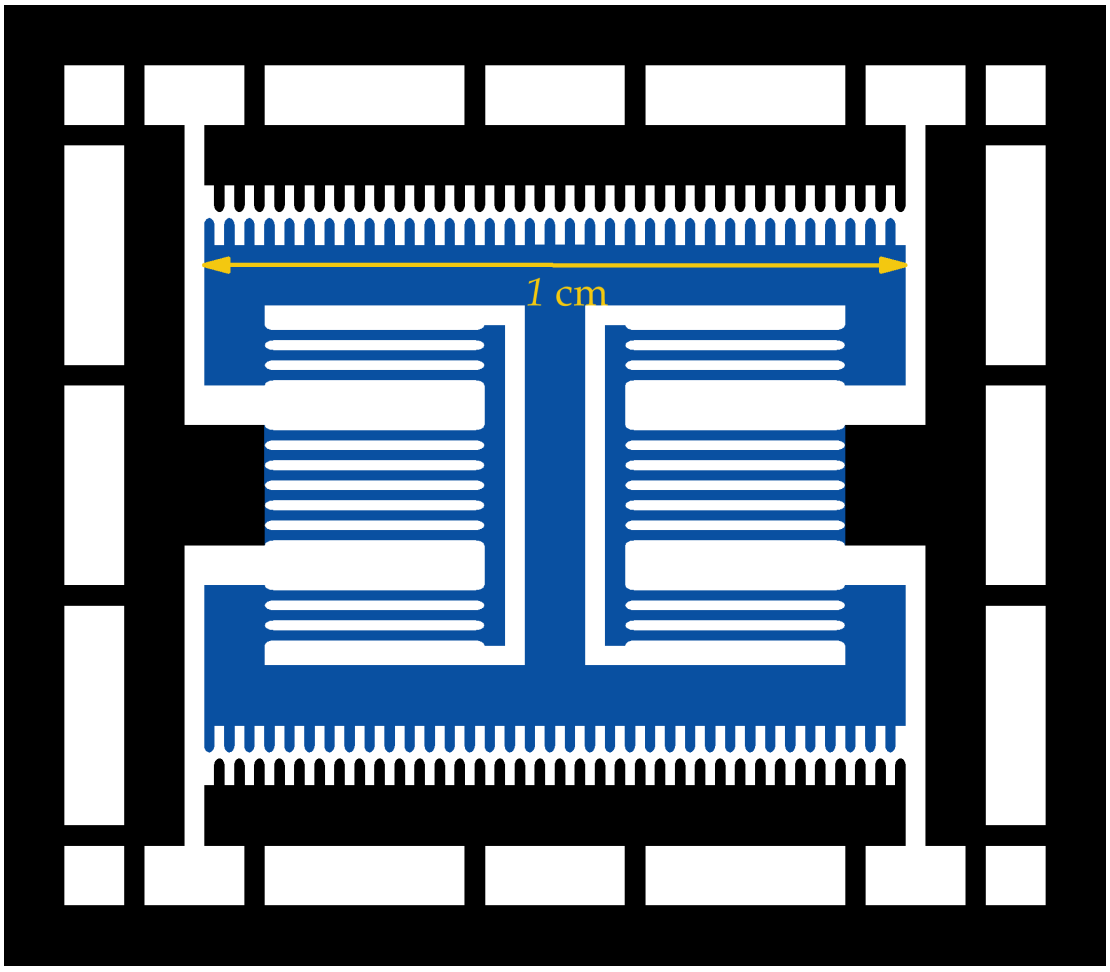

G.2 Variable-Gap Converter

This process attempts to create a variable-gap capacitor. The square Si/gold mass moves in and out of the page in the top view using a thin layer of Si/gold as a spring. Probes connect to the fixed Silicon field and to the gold on the Pyrex through the probe hole.

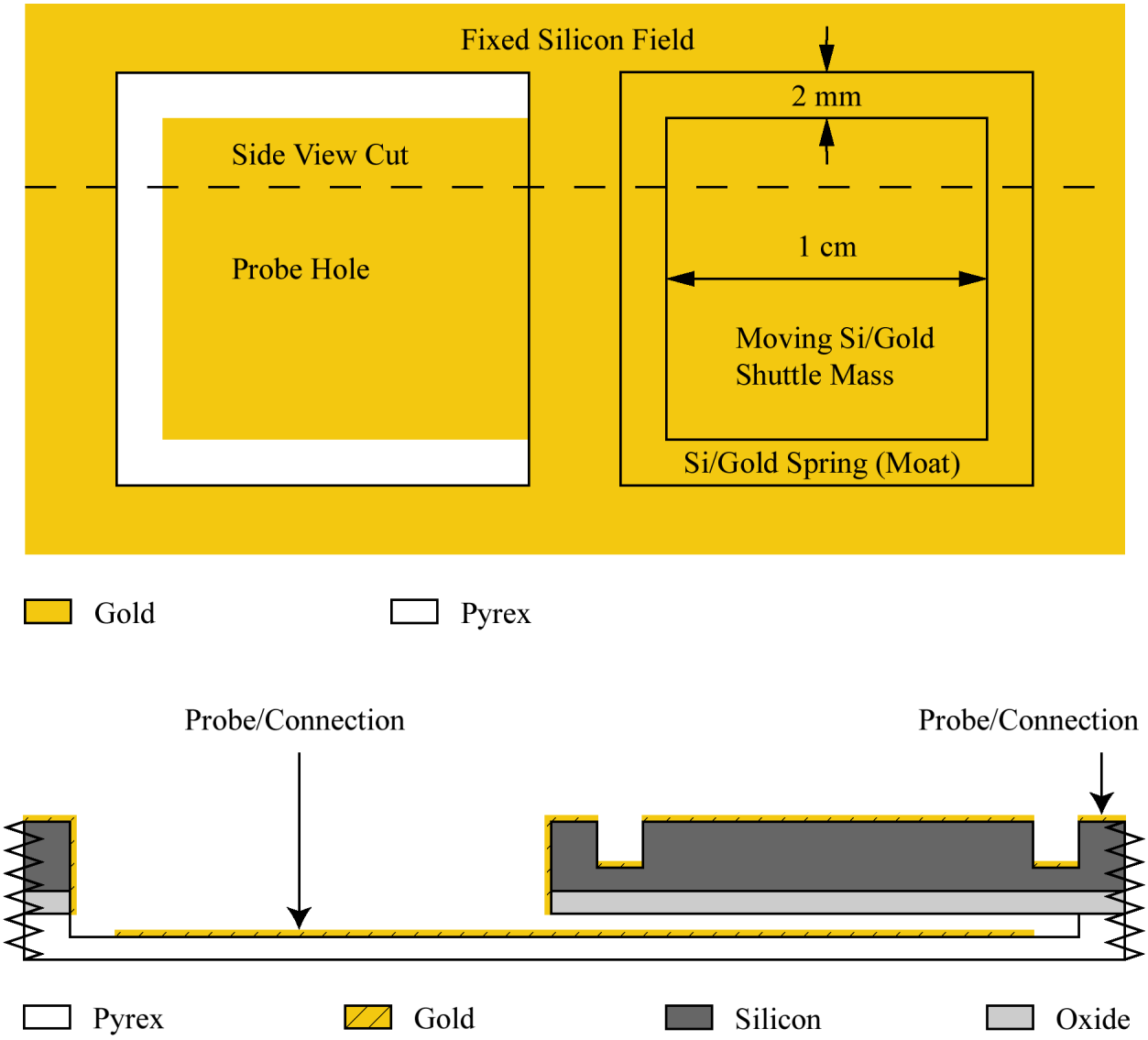

G.2.1 Device Wafer

1. Device wafers are nSi prime wafers, double polished, 500 μm thick, doped using $POCl_3$ with 1 μm grown thermal oxide.

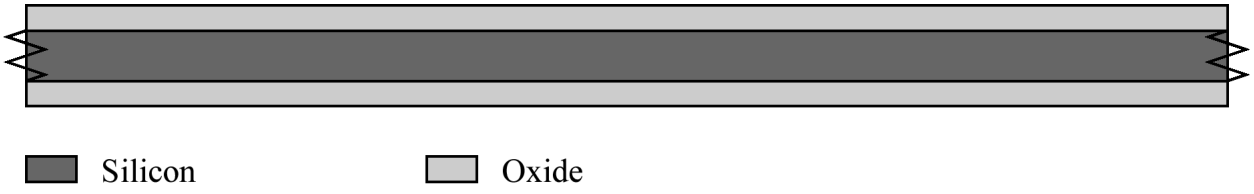

2. Coat backside with resist.

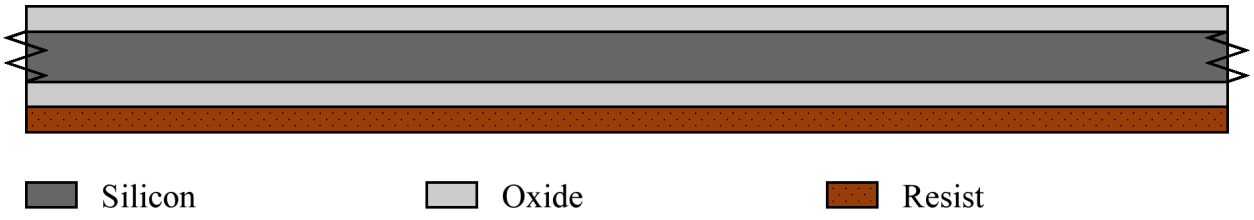

3. BOE etch of frontside TOx.

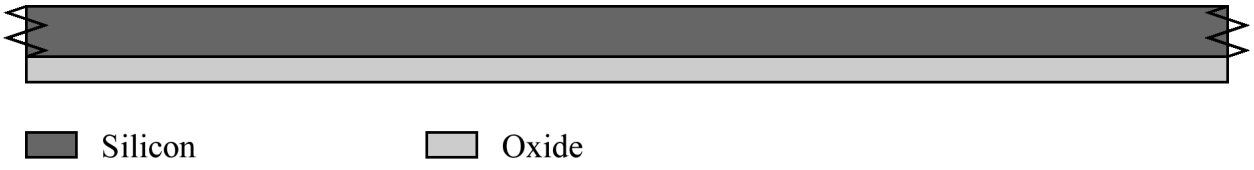

4. Coat both sides with 10 μm thick resist.

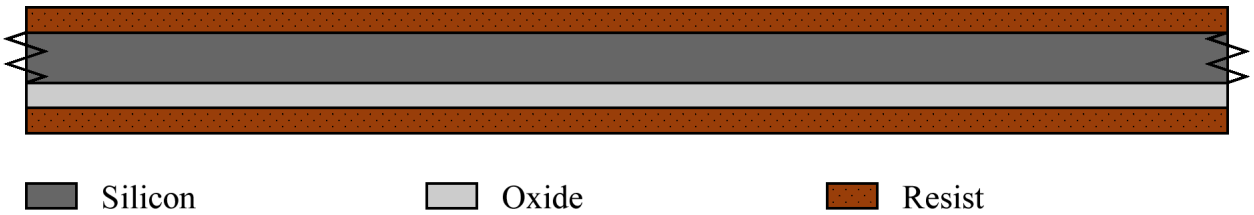

5. Develop frontside side using “DEVICE” mask.

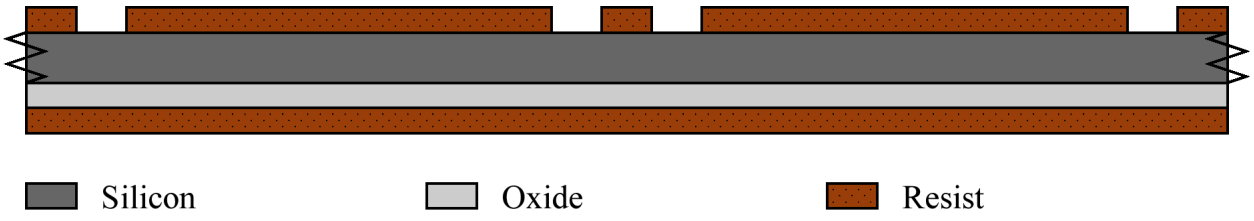

6. STS etch of Si. Etch mask or manual deposition of resist is used to cover the membrane spring after the desired etch depth has been achieved.

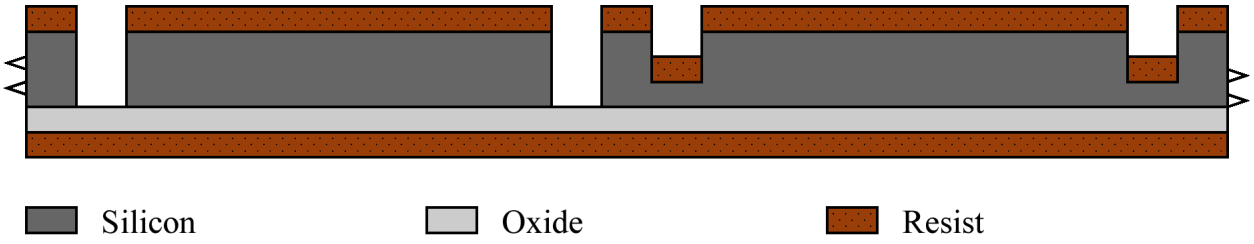

7. Acetone removal of resist.

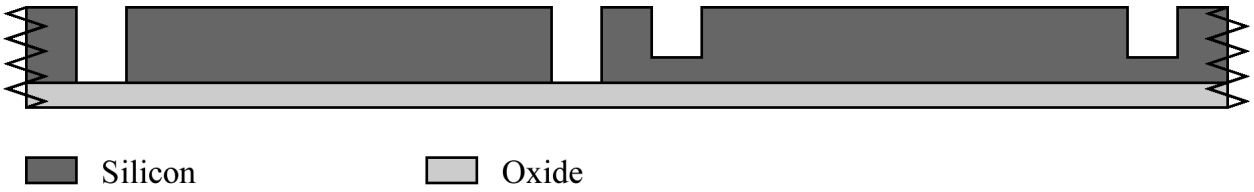

8. Coat backside with resist.

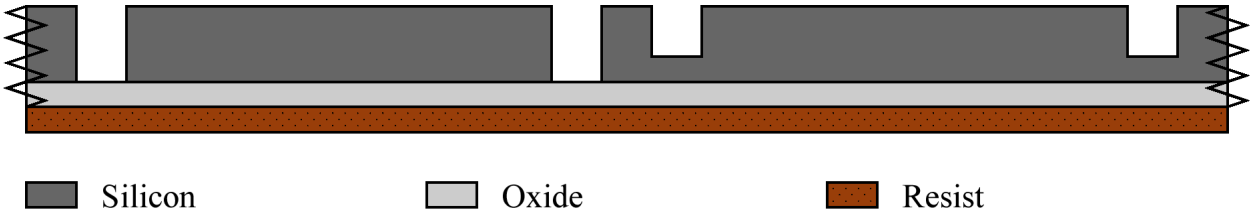

9. Develop backside resist using “CONTACT” mask.

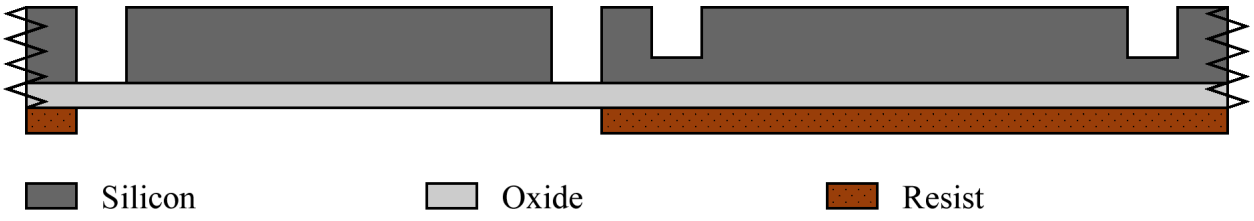

10. BOE etch of backside TOx.

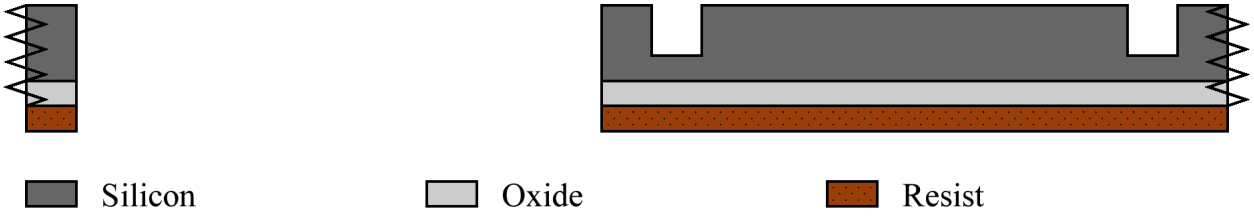

11. Piranha removal of resist.

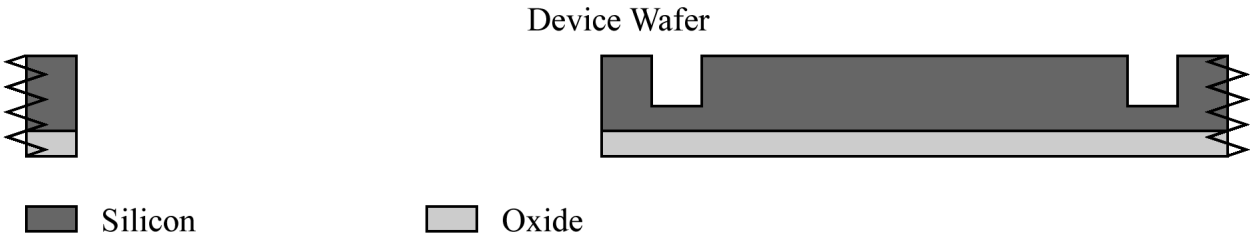

12. Deposition of 100 Å of Cr and 40 μm of Au to augment mass of Si shuttle.

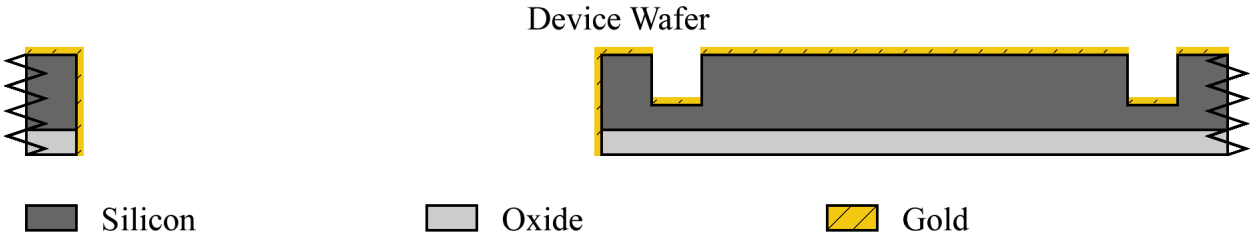

G.2.2 Handle Wafer

Note that a resist-only mask will not survive an etch of more than a few micrometers. To etch deeper, a chrome-gold mask should be used [23].

13. Handle wafers are 7740 Pyrex wafers, 500 μm thick.

14. Coat both sides with resist.

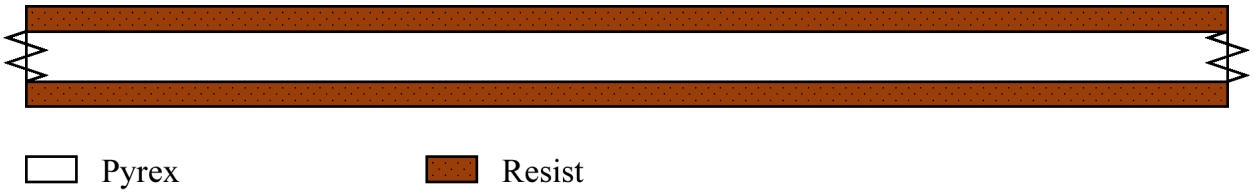

15. Develop resist using "PIT" mask.

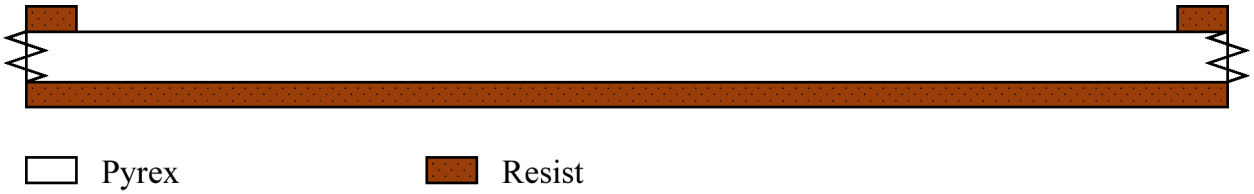

16. HF etch of Pyrex.

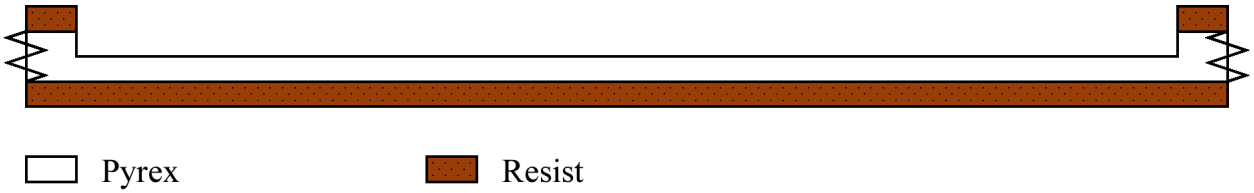

17. Gold piranha clean of resist.

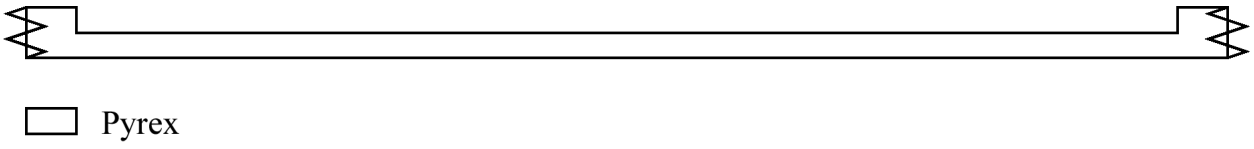

18. Selective deposition of metal using shadow mask.

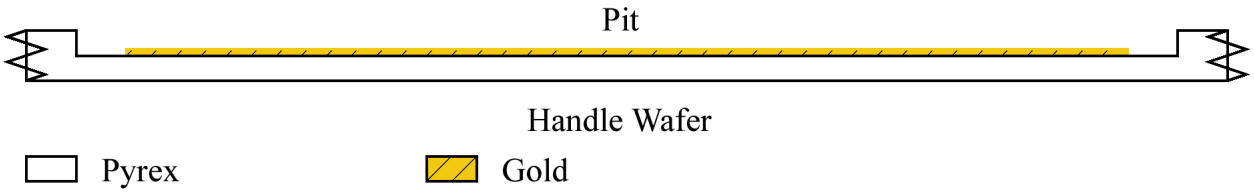

19. Anodic bond.

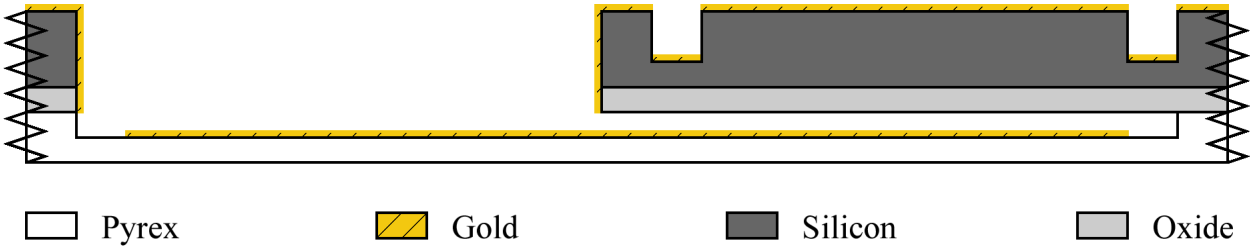

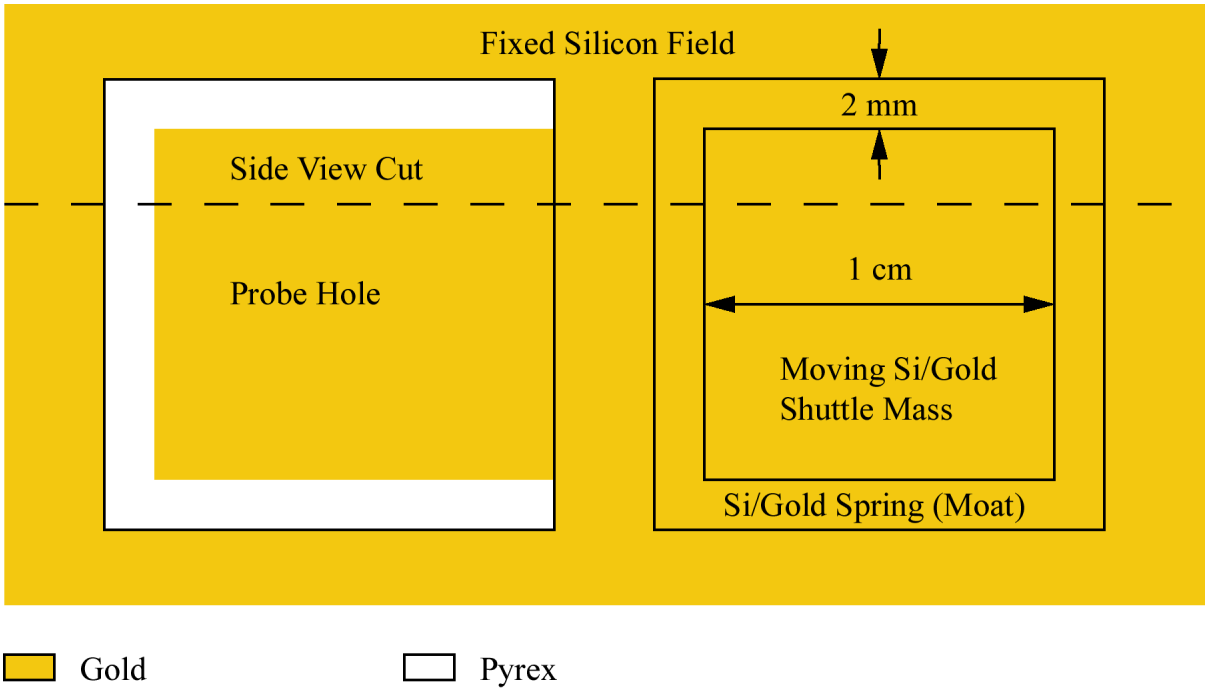

Appendix H

Fabrication Masks

The masks shown in this appendix were used in conjunction with the constant-gap fabrication process described in Appendix G to create the examples shown in Chapter 7. For each mask, a mask overview figure, a die-level figure and a detail of the fingers and suspension is shown.

H.1 Constant-Gap Converter Mask 3

Mask 3 does not include inside-out folded springs, taking much more area than 1 cm^2. This required bonding prior to etching the actual device. Halo pieces are used. The fingers were 12, 16, and 20 μm thick, with a gap, as drawn, of 1 μm. The shuttle masses have dimensions of 2 mm $\times$ 10 mm, 4 mm $\times$ 10 mm and 8 mm $\times$ 10 mm. The suspension uses flexure springs. Isolation was achieved during etching.

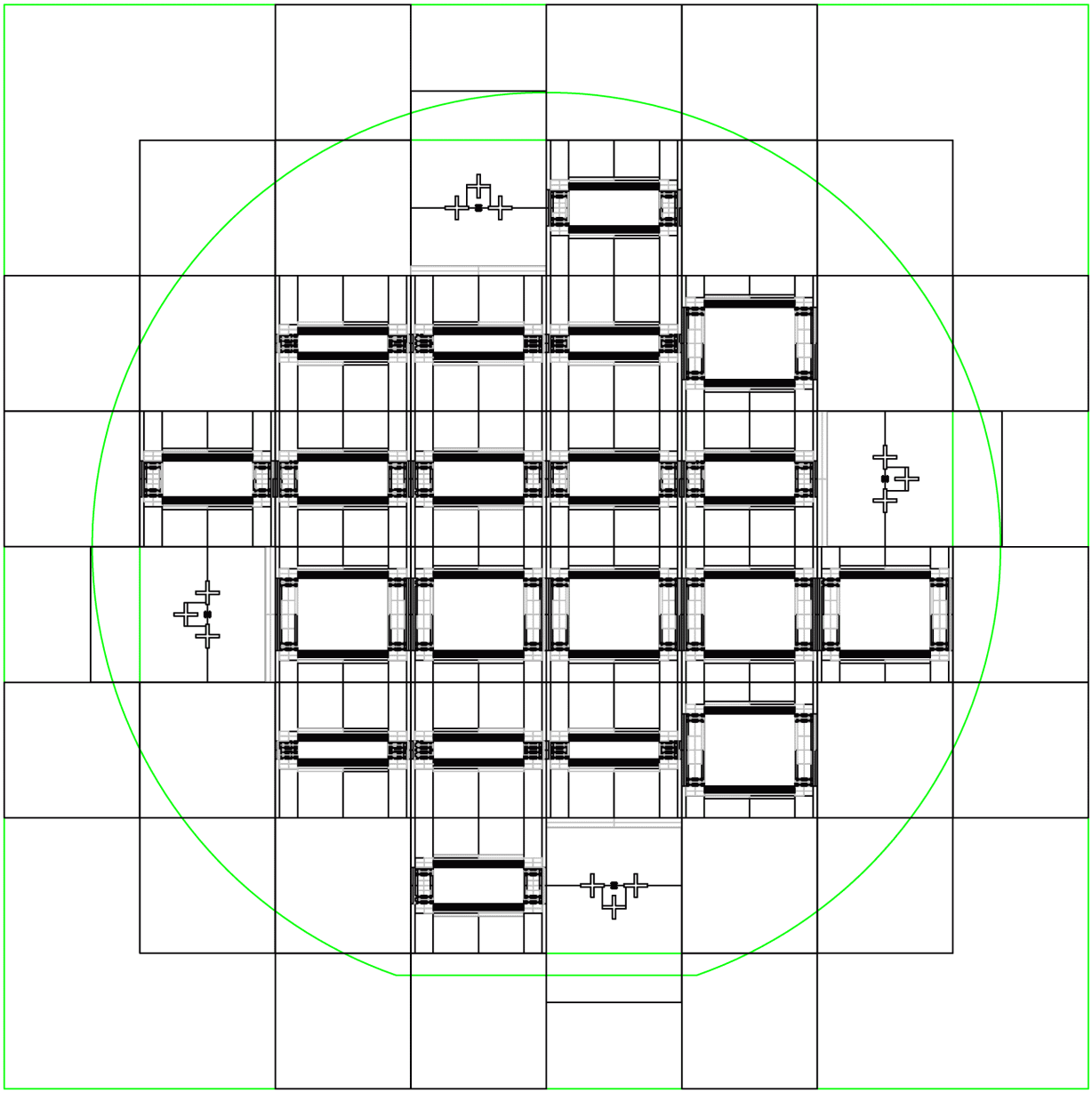

Figure H-1: Constant-gap converter mask 3.

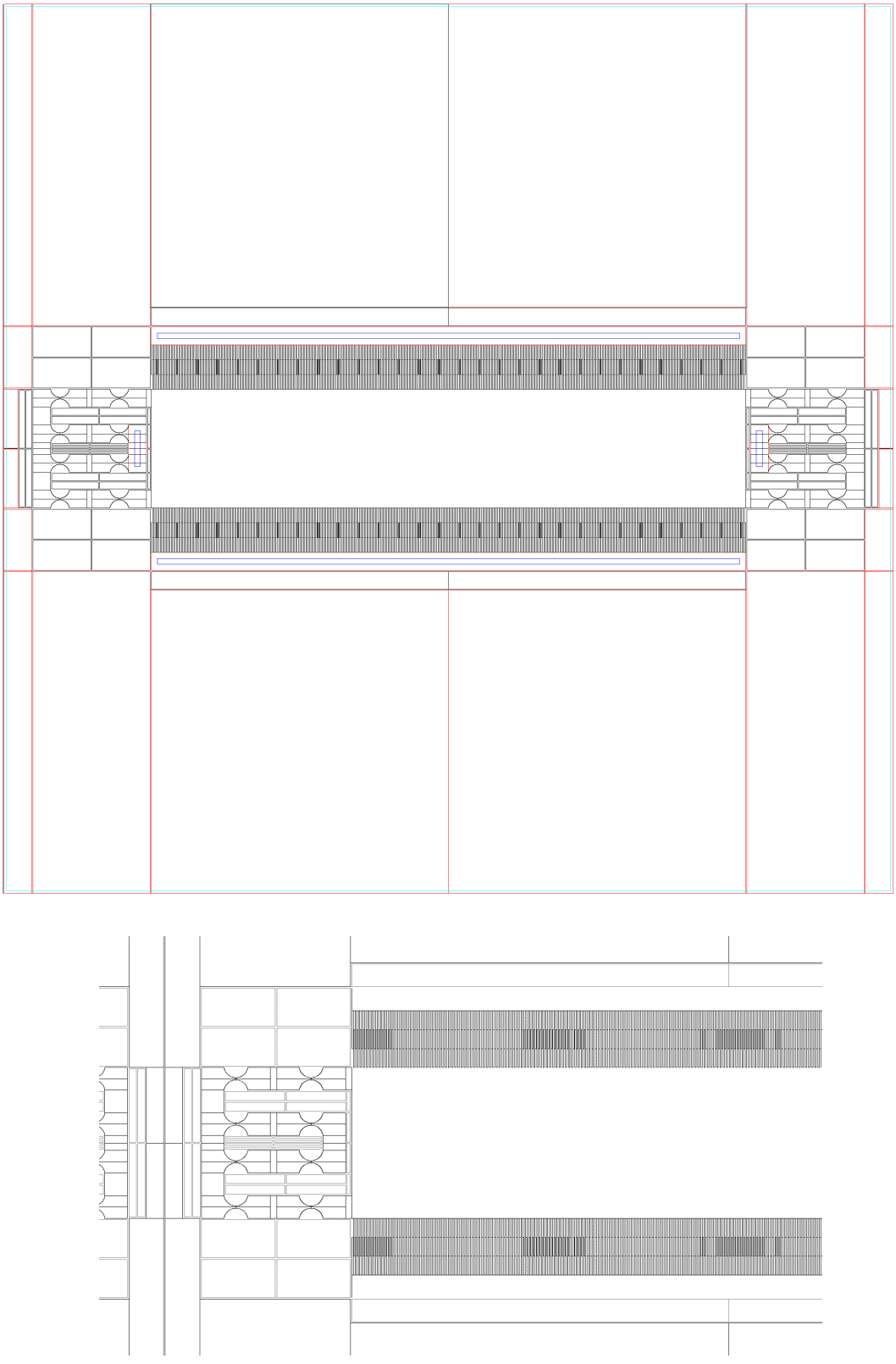

Figure H-2: Die level and detail of constant-gap converter mask 3.

H.2 Constant-Gap Converter Mask 7

Mask 7 includes inside-out folded springs, and the shuttle mass and suspension take a 1 cm^2 area. Halo pieces are used. The fingers are 20 μm thick, with a gaps, as drawn, of 10, 15, and 20 μm. The suspension uses multiple-beam springs. Isolation was achieved using die-saw after bonding.

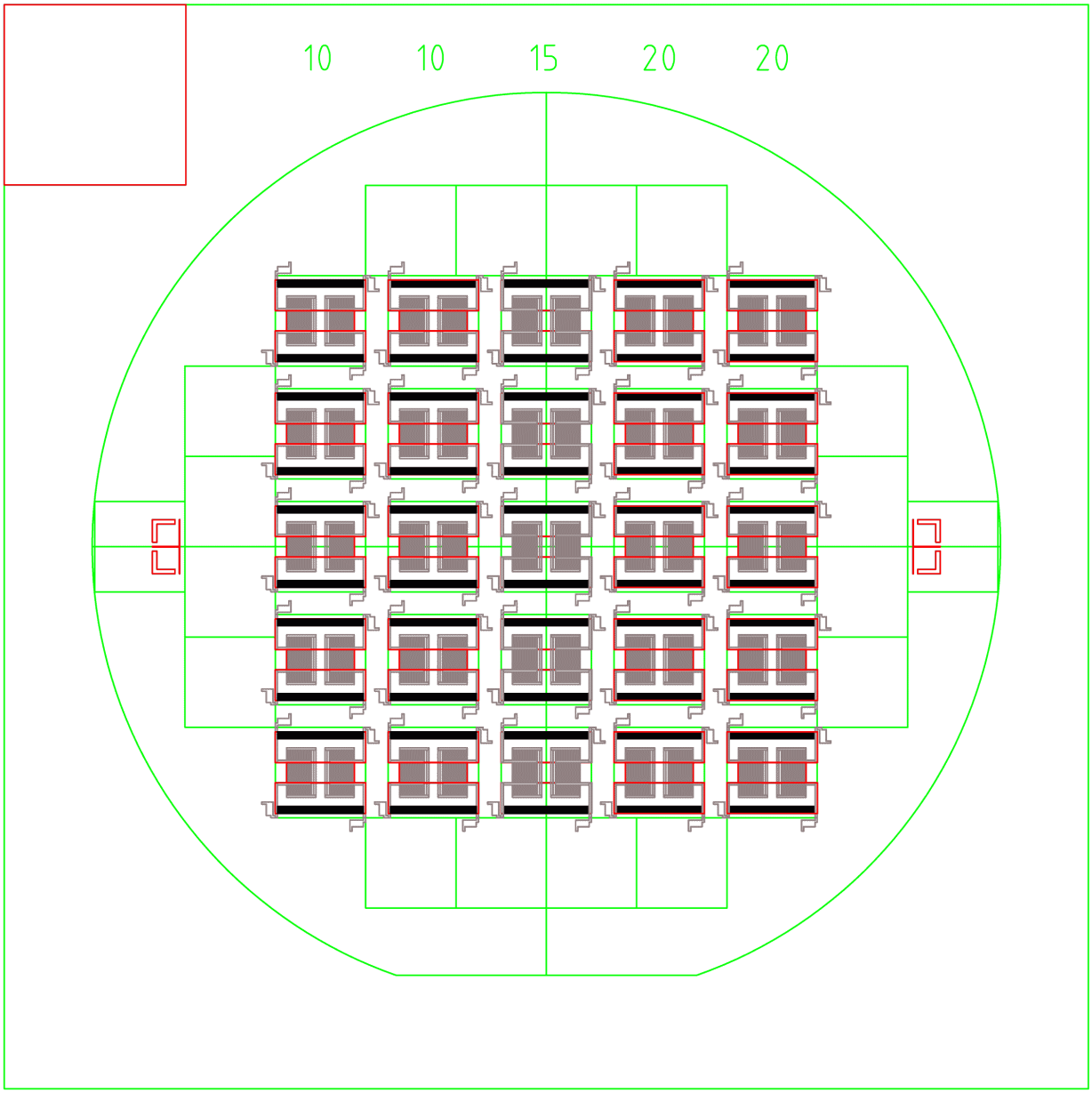

Figure H-3: Constant-gap converter mask 7.

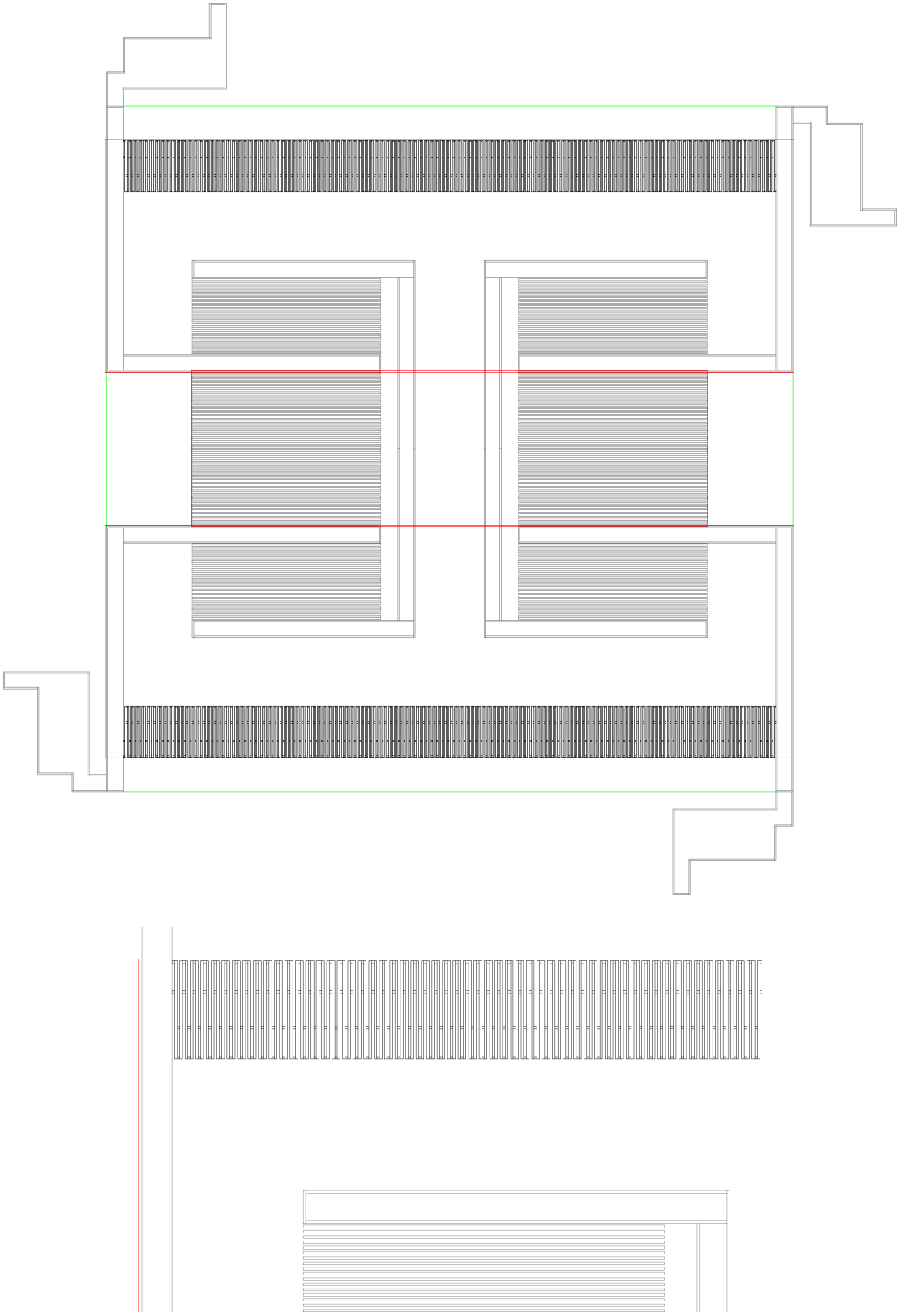

Figure H-4: Die level and detail of constant-gap converter mask 7.

H.3 Constant-Gap Converter Mask 10

Mask includes inside-out folded springs, and the shuttle mass and suspension take a 1 cm^2 area. The fingers were non-overlapping, 50 μm thick. The suspension uses flexure springs. Isolation was achieved using break-off tabs after bonding.

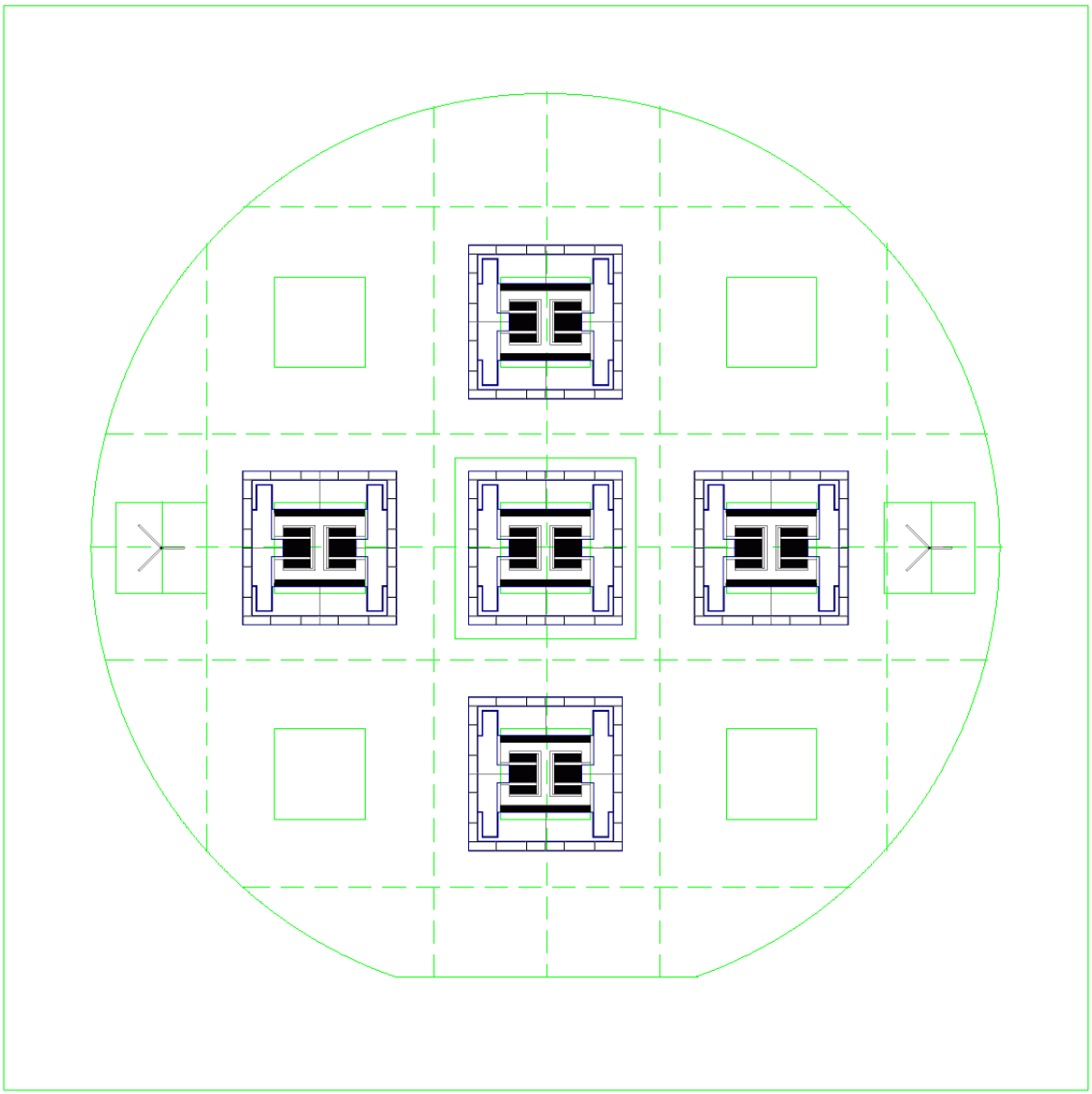

Figure H-5: Constant-gap converter mask 10.

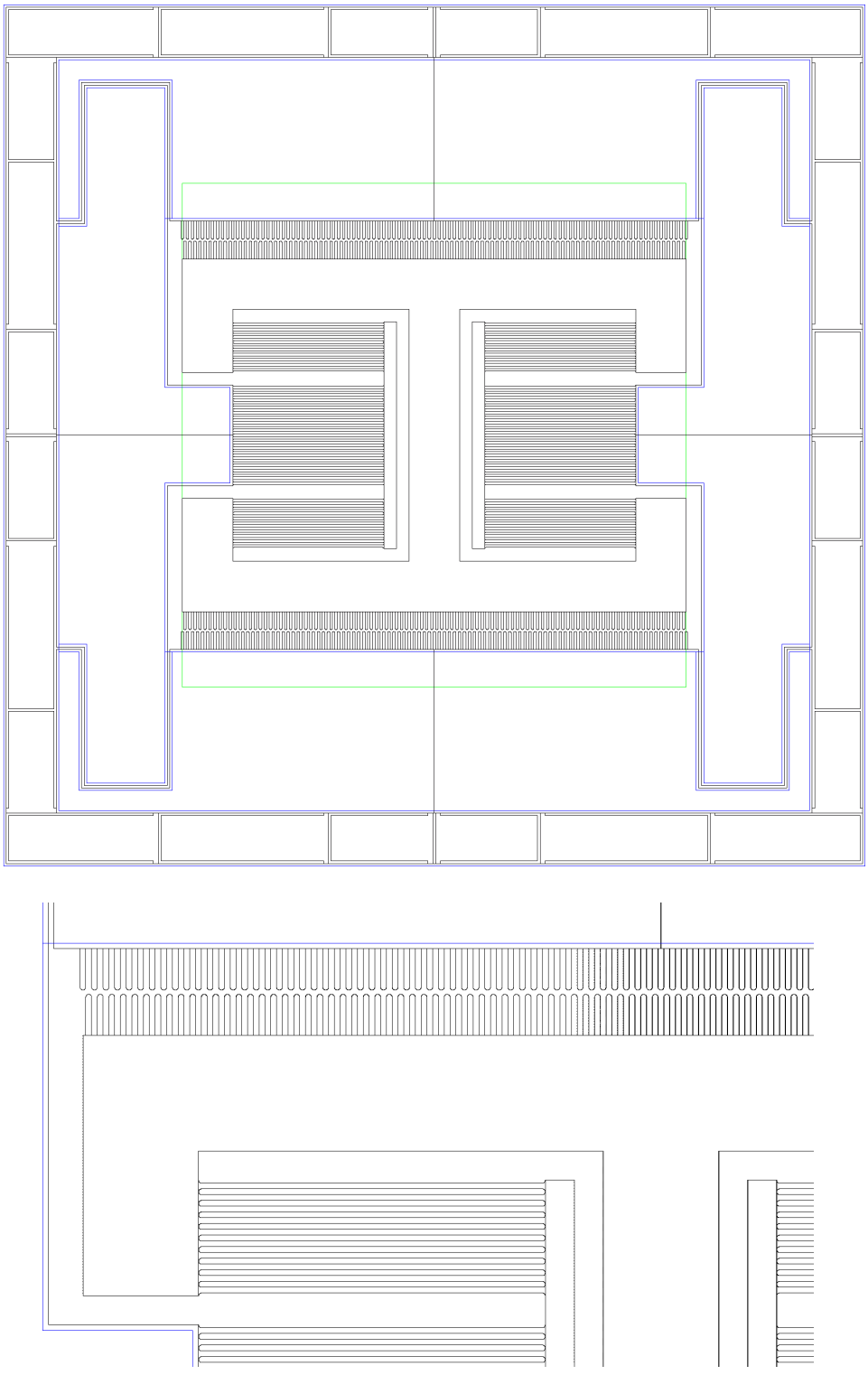

Figure H-6: Die level and detail of constant-gap converter mask 10.

Bibliography

[1] Jaber Abu-Qahouq and Issa Batarseh. Generalized analysis of soft-switching DC-DC converters. In *IEEE International Symposium on Circuits and Systems*, Geneva, Switzerland, May 28-31, 2000.

[2] Rajeevah Amirtharajah and Anantha P. Chandrakasan. Self-powered signal processing using vibration-based power generation. *IEEE Journal of Solid-State Circuits*, 33(5):687–695, May 1998.

[3] Rajeevan Amirtharajah. *Design of Low Power VLSI Systems Powered by Ambient Mechanical Vibration*. Ph.D. dissertation, Massachusetts Institute of Technology, Department of Electrical Engineering and Computer Science, June 1999.

[4] Rajeevan Amirtharajah, Scott Meninger, Jose Oscar Mur-Miranda, Anantha P. Chandrakasan, and Jeffrey H. Lang. A micropower programmable DSP powered using a MEMS-based vibration-to-electric energy converter. *Digest of Technical Papers - IEEE International Solid-State Circuits Conference*, pages 362–363, 469, February 2000.

[5] Arturo A. Ayón, Rebecca A. Braff, Chuang-Chia Lin, Herb H. Sawin, and Martin A. Schmidt. Characterization of a time multiplexed inductively coupled plasma etcher. *Journal of the Electrochemical Society*, 146(1):339–349, 1999.

[6] Arturo A. Ayón, Chuang-Chia Lin, Rebecca A. Braff, Martin A. Schmidt, and Herb H. Sawin. Etching characteristics and profile control of a time multiplexed inductively coupled plasma etching system. *Solid State Sensor and Actuator Workshop*, 1998.

[7] Arturo A. Ayón, Xin Zhang, and Ravi Khanna. Anisotropic silicon trenches 300-500 μm deep employing time multiplexed deep etching (TMDE). *Sensors and actuators A*, 91:381–385, 2001.

[8] Stephen F. Bart, Theresa A. Lober, Roger T. Howe, Jeffrey H. Lang, and Martin F. Schlecht. Design considerations for micromachined electric actuators. *Sensors and Actuators*, 14(3):269–292, July 1988.

[9] Anantha P. Chandrakasan, Rajeevah Amirtharajah, SeongHwan Cho, James Goodman, Gangadhar Konduri, Wendi Rabiner, and Alice Wang. Design considerations for distributed microsensor systems. *IEEE 1999 Custom Integrated Circuits Conference*, pages 279–286, 1999.

[10] Anantha P. Chandrakasan, Rajeevah Amirtharajah, James Goodman, and Wendi Rabiner. Trends in low power digital signal processing. *Proceedings of the 1998 IEEE International Symposium on Circuits and Systems*, 4:604–607, 1998.

[11] ONSITE SYCOM Energy Corporation. *Review of Combined Heat and Power Technologies*. Office of Industrial Technologies, Office of Energy Efficiency and Renewable Energy, U.S. Department of Energy, October 1999.

[12] Alan H. Epstein. Millimeter-scale, MEMS gas turbine engines. In *Proceedings of ASME Turbo Expo 2003, Power for Land, Sea, and Air*, Atlanta, Georgia, June 16-19, 2003.

[13] H. Guckel, J.J. Sniegowski, and T.R. Christenson. Advances in processing techniques for silicon micromechanical devices with smooth surfaces. In *Proceedings of Micro Electro Mechanical Systems, 'An Investigation of Micro Structures, Sensors, Actuators, Machines and Robots'*, pages 71–75, Salt Lake City, Utah, February 20-22, 1989.

[14] T. Hirano, T. Furuhata, K.J. Gabriel, and H. Fujita. Design, fabrication and operation of submicron gap comb-drive microactuators. *Journal of Microelectromechanical Systems*, 1(1), March 1992.

[15] V.P. Jaecklin, C. Linder, N.F. de Rooij, J.M. Moret, R. Bischof, and F. Rudolf. Novel polysilicon comb actuators for XY stages. In *Microelectromechanical Systems '92*, Travemunde, Germany, February 4-7, 1992.

[16] W.-H. Juan and S.W. Pang. High-aspect-ratio Si vertical micromirror arrays for optical switching. *Journal of Microelectromechanical Systems*, 7(2), June 1998.

[17] Swarn S. Kalsi. Development status of superconducting rotating machines. *IEEE Power Engineering Society Winter Meeting*, 1:401–403, January 2002.

[18] John G. Kassakian, Martin F. Schlecht, and George C. Verghese. *Principles of Power Electronics*. Addison-Wesley, 1991.

[19] John Kymissis, Clyde Kendall, Joseph A. Paradiso, and Neil Gershenfeld. Parasitic power harvesting in shoes. *Proceedings of the Second IEEE International Conference on Wearable Computing (ISWC)*, pages 132–139, October 1998.

[20] B. Lee, S. Seok, and K. Chun. A study on wafer level vacuum packaging for mems devices. *Journal of Micromechanics and Microengineering*, 13:663–669, 2003.

[21] C.S.-B. Lee, S. Han, and N.C. MacDonald. Multiple depth, single crystal silicon microactuators for large displacement fabricated by deep reactive ion etching. In *Solid-State Sensor and Actuator Workshop*, Hilton Head Island, South Carolina, June 8-11, 1998.

[22] Johnny M.H. Lee, Steve C.L. Yuen, Wen J. Li, and Philip H.W. Leong. Development of an AA size energy transducer with micro resonators. In *IEEE International Symposium on Circuit and Systems*, Thailand, May 2003.

[23] Jian Li, Michael P. Brenner, Jeffrey H. Lang, Alexander H. Slocum, and Ralf Struempler. Drie-fabricated curved-electrode zipping actuators with low pull-in voltage. In *The 12th International Conference on Solid State Sensors, Actuators and Microsystems*, Boston, Massachusetts, June 8-12, 2003.

[24] Liwei Lin, Roger T. Howe, and Albert P. Pisano. Microelectromechanical filters for signal processing. *Journal of Microelectromechanical Systems*, 7(3):286–294, September 1998.

[25] Scott Meninger. *A Low Power Controller for a MEMS Based Energy Converter*. M.S. dissertation, Massachusetts Institute of Technology, Department of Electrical Engineering and Computer Science, June 1999.

[26] Scott Meninger, Jose Oscar Mur-Miranda, Rajeevan Amirtharajah, Anantha P. Chandrakasan, and Jeffrey H. Lang. Vibration-to-electric energy conversion. *IEEE Transactions On Very Large Scale Integration (VLSI) Systems*, 9(1):64–76, February 2001.

[27] Masayuki Miyazaki, Hidetoshi Tanaka, Goichi Ono, Tomohiro Nagano, Norio Ohkubo, Takayuki Kawahara, and Kazuo Yano. Electric-energy generation using variable-capacitive resonator for power-free LSI: Efficiency analysis and fundamental experiment. In *Proceedings of the 2003 International Symposium on Low Power Electronics and Design*, pages 193–198, Seoul, Korea, August 25-27, 2003.

[28] Jin Qiu, Jeffrey H. Lang, and Alexander H. Slocum. A centrally-clamped parallel-beam bistable MEMS mechanism. In *Proceedings of IEEE International Workshop on Micro Electro Mechanical Systems*, pages 353–356, Switzerland, January 2125, 2001.

[29] Jin Qiu, Jeffrey H. Lang, Alexander H. Slocum, and Ralf Struempler. A high-current electrothermal bistable MEMS relay. In *Proceedings of IEEE International Workshop on Micro Electro Mechanical Systems*, pages 64–67, Japan, January 1923, 2003.

[30] Shad Roundy, Paul K. Wright, and Kristofer S. J. Pister. Micro-electrostatic vibration-to-electricity converters. *ASME International Mechanical Engineering Congress & Exposition*, November 17-22, 2002.

[31] Stephen D. Senturia. *Microystem Design*. Kluwer Academic Publishers, 2001.

[32] C. Shearwood and Rob B. Yates. Development of an electromagnetic microgenerator. *Electronics Letters*, 33(22):1883–1884, October 23, 1997.

[33] Alexander H. Slocum. *Precision Machine Design*. Society of Manufacturing Engineers, 1992.

[34] Tom Sterken, Kris Baert, Robert Puers, and Staf Borghs. Power extraction from ambient vibration. In *Proceedings of Semiconductor Sensors*, pages 680–683, Veldhoven, The Netherlands, November 29, 2002.

[35] J. Lodewyk Steyn, Carol Livermore, and Gwendolyn Donahue. Wall profile measurements of DRIE-etched wafers. Research in support of the MIT microengine project.

[36] W.C. Tang, T.-C. H. Nguyen, and R.T. Howe. Laterally driven polysilicon resonant microstructures. *Proceedings of Micro Electro Mechanical Systems, 'An Investigation of Micro Structures, Sensors, Actuators, Machines and Robots'*, pages 53–59, 1989.

[37] Kun Wang and Clark T.-C. Nguyen. High-order medium frequency micromechanical electronic filters. *Journal of Microelectromechanical Systems*, 8(4):534–557, December 1999.

[38] Kun Wang, Ark-Chew Wong, and Clark T.-C. Nguyen. VHF free-free beam high-Q micromechanical resonators. *Journal of Microelectromechanical Systems*, 9(3):347–360, September 2000.

[39] C.B. Williams and Rob B. Yates. Analysis of a microelectric generator for microsystems. In *Proceedings of Transducers '95/Eurosensors IX*, pages 369–372, Stockholm, Sweden, 1995.

[40] C.B. Williams and Rob B. Yates. Analysis of a micro-electric generator for microsystems. *Sensors and Actuators*, 52:8–11, 1996.

[41] Herbert H. Woodson and James R. Melcher. *Electromechanical Dynamics: Part I (Discrete Systems) and Part II (Fields, Forces, and Motion)*. Wiley, 1968.

[42] Victor Wowk. *Machinery Vibration: Measurement and Analysis*. McGraw-Hill, 1991.

[43] Xueen Yang. *A MEMS Valve for the MIT Microengine*. M.S. dissertation, Massachusetts Institute of Technology, Department of Mechanical Engineering, May 2001.